Understanding the BCC refractory multi-principal elements alloys using thermodynamics and nanoindentation

Zur Erlangung des akademischen Grades eines

Doktors der Ingenieurwissenschaften
(Dr.-Ing.)

von der KIT-Fakultät für Maschinenbau des
Karlsruher Instituts für Technologie (KIT)

angenommene
Dissertation
von

M.tech **Silva Basu**
aus Kalkutta, Indien

Tag der mündlichen Prüfung:	25.04.2025
Hauptreferent:	Prof. Martin Heilmaier
Korreferentin:	Prof. Dr. Ruth Schwaiger

Abstract

Understanding the stability of multi-principal elements alloys (MPEA) is intriguing as the chemistry and elemental interactions make the thermodynamic and mechanical properties complex. In order to understand these novel material systems, the study of the stability of such alloys is critical. This represents the central topic of this work, which focusses primarily on the body-centred cubic (BCC) system. The topic is approached from two different directions, namely thermodynamic stability and mechanical stability, using simulations and experimental methods.

The thermodynamic stability of alloys is described by the probability of an alloy existing as a single-phase or multiphase (if designed so) for a range of temperatures without any phase or crystallographic changes. As the name suggests, in MPEAs more elements in the system increase the configurational entropy of the system, which in turn lowers the free energy of the alloy and reduces the chance to form a stable single-phase solid solution.

In this work, the focus is on understanding the order-disorder transition in alloys with multiple elements, initiated by configurational entropy. The Potts model for ferromagnetism is extended to multiple elements containing alloys by setting the spin variable as equivalent to the number of elements in the system. The nearest-neighbour interaction of atoms at a lattice site is considered to calculate the ordering of the elements using Monte Carlo

simulations. Therefore, the total energy of the system that excludes the enthalpy of mixing is given by the interaction of the neighbouring atoms; in other words, the configurational entropy. The enthalpy of mixing is the interaction energy of the atoms, which is considered unity and uniform for the simplification of the theory. The order-disorder transition is calculated for systems with increments of two to eight elements. The order-disorder transition temperature is calculated using the regular solution model that is primarily used for binary systems. The energy change in the system was used to calculate the order-disorder transition temperature of the systems with an increasing element from two to eight. The phase diagram construction bolstered the results. Binary, ternary, and quinary systems were observed in detail to understand the changes as the number of elements in the system increased. The order-disorder transition is observed to be a function of configurational entropy and decreases with an increase in elements in the system. It is also seen that, for different crystallographic systems, entropy by itself affects the order-disorder transition and thermodynamic stability of alloys.

Mechanical stability, on the other hand, is here understood as the stability of properties and deformation mechanisms over a range of temperatures and loading conditions. NbMoCrTiAl and its family of alloys, such as MoCrTiAl and NbMoTiAl, were investigated to understand the mechanical stability of BCC-refractory MPEAs. These are brittle at ambient temperature under compression in comparison to an established BCC refractory MPEA TiNbHfZrTa which shows 40% plastic deformability under compression at room temperature. Considering the brittleness of the system, nanoindentation is the method of choice to study the deformation behaviour. The otherwise brittle MPEAs deform plastically under indentation loading. The mechanical properties of the alloys are correlated with the stability of the solid solution strengthening, which is a complex for MPEAs due to the higher number of elements in the solid solution. The lattice mismatch due to different elements of various atomic radii aids the crystallographic ordering and disordering in the system and, in turn, the mechanical properties. However, the effect of the shear modulus mismatch cannot be directly correlated for these alloys in question.

Mechanical stability can be further stretched to the response to deformation of the alloys and, in turn, the dislocation interactions that lead to deformation. The dislocation interaction involves understanding the nucleation and motion of the dislocation. The dislocation nucleation was comprehended by statistical analysis of the so-called pop-in phenomenon, which marks the onset of plastic deformation. The activation volume obtained from this experiment points to active dislocation mechanisms. The BCC structure of the alloys suggested heterogeneous nucleation by atom vacancy exchange. NbMoCrTiAl and its family of alloys were compared to the otherwise ductile TiNbHfZrTa alloy. The subsequent phenomena are found to be different for the two systems, which might be the cause of different ductility at room temperature. While the system NbMoCrTiAl and its family of alloys show pencil glide at room temperature, as does most BCC alloys, TiNbHfZrTa behaves similarly to FCC systems allowing deformation guided by accommodation bands, allowing it to be more ductile at room temperature.

The activation volume of the dislocation motion was further studied by subjecting the systems to a range of strain rates under indentation loading. This not only helps us understand the characteristics of the dislocation mechanisms, but also yields the strain rate sensitivity of the alloys. The results helped to conclude that all the systems despite different initiation of the deformation mechanism follow kink-pair nucleation. The dislocation motion under stress at room temperature is like that of most reported BCC alloys and is sensitive to changes in the strain rate at room temperature, which is below the critical temperature of deformation in BCC. Above the critical temperature or the

Knee temperature, a system exhibits an elastic interaction between the kink pairs and does not show any strain rate sensitivity. NbMoCrTiAl and its family of alloys are also tested for mechanical stability under nanoindentation over a range of temperatures to determine the knee temperature and the dislocation interaction procedure adapted by these alloys.

Kurzfassung

Das Verständnis der Stabilität von Legierungen, die aus mehreren Hauptelementen bestehen (MPEA), ist ein faszinierendes Thema, da die chemischen und elementaren Wechselwirkungen die thermodynamischen und mechanischen Eigenschaften komplex machen. Um diese neuartigen Materialsysteme zu verstehen, ist die Untersuchung der Stabilität solcher Legierungen von entscheidender Bedeutung. Dies stellt das zentrale Thema dieser Arbeit dar, die sich hauptsächlich mit dem körperzentrierten kubischen (BCC) System befasst. Das Thema wird aus zwei verschiedenen Richtungen angegangen, nämlich der thermodynamischen Stabilität und der mechanischen Stabilität unter Verwendung von Simulationen und experimentellen Methoden.

Die thermodynamische Stabilität von Legierungen wird durch die Wahrscheinlichkeit beschrieben, dass eine Legierung einphasig oder mehrphasig (sofern ausgelegt) für einen Temperaturbereich ohne Phasen- oder kristallographische Veränderungen vorliegt. Wie der Name schon sagt, erhöhen in MPEAs mehr Elemente im System die Konfigurationsentropie des Systems, was wiederum die freie Energie der Legierung senkt und die Chance verringert, eine stabile einphasige feste Lösung zu bilden. In dieser Arbeit liegt der Fokus auf dem Verständnis des Ordnungs-Unordnungs-Übergangs in Legierungen mit mehreren Elementen, initiiert durch die Konfigurationsentropie. Das Potts-Modell für Ferromagnetismus wird auf mehrere Elemente, die Le-

gierungen enthalten, erweitert, indem die Spin-Variable als äquivalent zur Anzahl der Elemente im System gesetzt wird. Die Nächste-Nachbar-Wechselwirkung von Atomen an einem Gitterplatz zur Berechnung der Ordnung der Elemente wird unter Verwendung von Monte-Carlo-Simulationen berücksichtigt. Daher ist die Gesamtenergie des Systems ohne Mischungsenthalpie durch die Wechselwirkung der Nachbaratome gegeben, also die Konfigurationsentropie. Die Mischungsenthalpie, also die Wechselwirkungsenergie der Atome, wird zur Vereinfachung der Theorie mit eins angenommen und ist einheitlich. Der Ordnungs-Unordnungs-Übergang wird für Systeme mit Inkrementen von zwei bis acht Elementen berechnet. Die Ordnungs-Unordnungs-Übergangstemperatur wird mit dem regulären Lösungsmodell berechnet, das hauptsächlich für binäre Systeme verwendet wird. Die Energieänderung im System wurde verwendet, um die Ordnungs-Unordnungs-Übergangstemperatur der Systeme mit zunehmendem Element von zwei auf acht zu berechnen. Das konstruierte Phasendiagramm unterstützte die Ergebnisse. Die binären, ternären und quinären Systeme wurden im Detail beobachtet, um die Änderungen der Anzahl der Elemente im Systeminkrement zu verstehen. Es wird beobachtet, dass der Ordnungs-Unordnungs-Übergang eine Funktion der Konfigurationsentropie ist und mit zunehmender Anzahl von Elementen im System abnimmt. Es ist auch ersichtlich, dass für verschiedene kristallographische Systeme die Entropie selbst den Ordnungs-Unordnungs-Übergang und die thermodynamische Stabilität von Legierungen beeinflusst.

Unter mechanischer Stabilität hingegen wird hier die Stabilität von Eigenschaften und Verformungsmechanismen über einen Bereich von Temperaturen und Belastungsbedingungen verstanden. NbMoCrTiAl und seine Legierungsfamilie, wie MoCrTiAl und NbMoTiAl, wurden untersucht, um die mechanische Stabilität von BCC-refraktären MPEAs zu verstehen. Diese sind bei Umgebungstemperatur unter Druck spröde im Vergleich zu einem etablierten feuerfesten BCC-MPEA TiHfZrNbTa, das unter Druck bei Raumtemperatur eine Verformbarkeit von 40% aufweist. Unter Berücksichtigung der Sprödigkeit des Systems ist die Nanoindentation die Methode der Wahl, um das Verformungsverhalten zu untersuchen. Die ansonsten spröden MPEAs verformen sich unter Eindruckbelastung plastisch. Die mechanischen Eigenschaften der Legierungen korrelieren mit der Stabilität der Mischkristallverfestigung, die für MPEAs aufgrund der höheren Anzahl von Elementen im Mischkristall ein Komplex ist. Die Gitterfehlanpassung aufgrund verschiedener Elemente mit unterschiedlichen Atomradien unterstützt die kristallographische Ordnung und Unordnung im System ,welche wiederum die mechanischen Eigenschaften unterstützt. Allerdings kann der Effekt der Fehlanpassung des Schermoduls für diese fraglichen Legierungen nicht direkt in Korrelation gesetzt werden.

Die mechanische Stabilität kann weiter auf das Verformungsverhalten der Legierungen und damit auf die Versetzungswechselwirkungen, die die Verformung hervorrufen, ausgedehnt werden. Die Versetzungswechselwirkung beinhaltet das Verständnis der Versetzungskeimbildung und -bewegung. Die Versetzungskeimbildung wurde durch statistische Analyse des sogenannten Pop-in-Phänomens erfasst, das den Beginn der plastischen Verformung markiert. Das aus diesem Experiment gewonnene Aktivierungsvolumen weist auf die aktiven Versetzungsmechanismen hin. Die BCC-Struktur der Legierungen legte eine heterogene Keimbildung durch Atomleerstellenaustausch nahe. NbMoCrTi-Al und seine Legierungsfamilie wurden mit der ansonsten duktilen TiHfZrNbTa-Legierung verglichen. Die Folgephänomene sind für die beiden Systeme unterschiedlich, was die Ursache für die unterschiedliche Duktilität bei Raumtemperatur sein könnte. Während das NbMoCrTiAl-System und seine Legierungsfamilie, wie die meisten BCC-Legierungen, bei Raumtemperatur Versetzungsgleiten aufweisen, verhält sich TiHfZrNbTa ähnlich wie FCC-Systeme und ermöglicht eine durch Akkommodationsbänder geführte Verformung, wodurch es bei Raumtemperatur duktiler ist.

Das Aktivierungsvolumen der Versetzungsbewegung wurde weiter untersucht, indem die Systeme einer Reihe von Dehnungsraten unter Eindrückbelastung ausgesetzt wurden. Dies hilft uns nicht nur, die Charakteristika der Versetzungsmechanismen zu verstehen, sondern ergibt auch die Dehnratenempfindlichkeit der Legierungen. Die Ergebnisse trugen zu der Schlussfolgerung bei, dass alle Systeme trotz unterschiedlicher Initiierung des Verformungsmechanismus der Versetzungszwilling Keimbildung folgen. Die Versetzungsbewegung unter Spannung bei Raumtemperatur ist ähnlich wie die meisten berichteten BCC-Legierungen, und reagiert empfindlich auf Änderungen der Dehnungsrate, was darauf hindeutet, dass diese unter der kritischen Verformungstemperatur von BCC-Legierungen liegt. Oberhalb der kritischen Temperatur oder der Knee-Temperatur zeigt ein System eine elastische Wechselwirkung zwischen den Knickpaaren und zeigt keine Dehnungsratensensitivität. NbMoCrTiAl und seine Legierungsfamilie werden auch auf mechanische Stabilität unter Nanoindentation über einen Bereich von Temperaturen getestet, um die Knietemperatur und das von diesen Legierungen angepasste Versetzungswechselwirkungsverfahren zu bestimmen.

Contents

Chapter 1

Introduction

“Learn how to see. Realize that everything connects to everything else.”

Leonardo da Vinci

1.1 Multi-principal elements alloys

The last two decades have seen the emergence of new alloys containing five or more elements, which are popularly known as *high entropy alloys (HEAs)* or *compositionally complex alloys (CCAs)*. These alloys can be present in equiatomic compositions such as $Fe_{20}Co_{20}Cr_{20}Mn_{20}Ni_{20}$, or in non-equiatomic compositions such as $Al_{10}Co_{25}Cr_{8}Fe_{15}Ni_{36}Ti_{6}$ [1, 2].

These *multi-principal element alloys (MPEAs)* were initially developed by Brian Cantor [1] and J. W. Yeh [3] independently in 2004. The primary concept proposed for these alloys was to increase the number of elements in the systems, in order to maximise the configurational entropy and obtain a single-phase substitutional solid solution. Since then, these alloys have been investigated in detail to understand not only the mechanical properties but also the thermodynamic stabilities of these alloys [4–9]. The increased number of elements in the systems allows for more complex alloys to form. Thus, these alloys can be engineered to obtain desirable mechanical or physical properties, such as improved ductility with strength, improved electrical resistance, low temperature resistance, and high temperature refractory behavior [10–13]. The MPEAs can be developed to have different crystal structures, such as: face-centred cubic (FCC), body-centred cubic (BCC), and hexagonal close-packed (HCP). Various MPEAs have been developed since then, such as FeCoCrMnNi (FCC), TiNbHfZrTa (BCC), DyGdHoLaTbY (HCP), FeCuCrMnNi (multiphase MPEAs); and have been studied in detail [1, 14–16].

One of the most widely studied MPEAs is FeCoCrMnNi. This is famously called the *Cantor alloy* as this was the first single-phase solid solution of FCC MPEA developed by Cantor [1]. This FCC system is highly ductile with enhanced strength and toughness. Further modifications have been performed on this system by altering or adding the composition, in order to achieve improved properties such as cryogenic stability or deformation-induced strengthening [17–20]. In comparison to FCC MPEAs, BCC MPEAs are more limited in variety and have not been extensively studied. Most BCC MPEAs such as MoNbTaW, MbNbTiVW, or TiNbHfZrTa are high-temperature resistant in nature [5, 14, 21]. Furthermore, the class of NbMoCrTiAl alloys is also a BCC refractory alloy but with a different set of properties than other popular BCC MPEA like TiNbHfZrTa [22, 23].

The versatile properties of these alloys were classically said to be governed by four major factors: high entropy effect, severe lattice distortion, sluggish diffusion, and cocktail effect [24]. However, as will be discussed later in section 1.1.3, sluggish diffusion does not dictate the properties of these alloys [25].

1.1.1 High entropy effect

On the basis of the concepts of physical metallurgy, when more than two elements interact to form a single solid solution, there is always a probability of intermetallic compound formation or phase separation. Such interactions influence the enthalpy of mixing of the alloys. However, keeping in mind the free energy of mixing the increased compositional elements will increase the configurational entropy and, in turn, thus lower the free energy of the system. According to the second law of thermodynamics, an equilibrium state is reached for a system that attains the lowest free energy of the system. The free energy of a system is controlled by the enthalpy of mixing and the entropy of mixing.

Yeh et al. [26] reported that as the number of components increases, the configurational entropy of the system also increases, but for MPEAs the mixing enthalpy is reduced. The enthalpy of mixing is usually lowered as a result of the possibility of forming pairs of unlike atoms whose enthalpy balances the pairs from like atoms. It can also be argued that the increase in the number of elements in the system increases the chances of forming a more ordered phase like an intermetallic compound. The decrease in enthalpy of mixing for like atoms generating intermetallic compounds, and the increase in entropy of mixing by increasing the number of constituents are always in competition. However, Miracle [27] also reported that the increase in configurational entropy destabilises intermetallic compounds at room temperature. At increased temperatures, following the second law of thermodynamics, most systems avoid ordered compounds. Thus, despite the fact that high entropy is a classically basic requirement for these alloys, it has been seen that without the enthalpy of mixing, the former is not the governing factor [27].

The variation of the solid solution and the possibilities of intermetallic compounds along with the change in the number of constituents is observed in alloys such as AlFeCoCrCuNi [28, 29]. AlFeCoCrCuNi shows a multicomponent solid solution of FCC as well as BCC phases at temperatures above 873 K and precipitation of B2 structures during cooling. CoCrFeNiMn has been reported to show a small difference in heat of mixing and results in a single-phase FCC solid solution [30]. Certain alloys have been designed to control the configurational entropy to obtain a multiphase system that exhibits specific properties. One such system is non-equiatomic FeMnCoCrNi, which has an increasing amount of HCP phase along with FCC phase under stress exhibiting stress-induced phase transformation [16]. This transformation improves the strength and ductility of the system.

1.1.2 Severe lattice distortion

A severe lattice distortion can be caused by the presence of a large number of elements with very different atomic sizes. The atomic size criteria are one of the most specific criteria for alloy formation, as mentioned by Hume-Rothery [31]. In order to obtain a binary alloy of solid solutions, the difference in atomic size should not exceed 15%. In addition, Porter et al. [32] have reported that the difference in size among the elements also determines the possibility of intermetallic phases or compounds. The crystallographic scenario changes for MPEAs with elements of varying atomic sizes, and the whole system becomes a solute matrix. In addition to the large difference among the atomic sizes of the elements (figure 1.1.1), the atomic bonding of each element with another element and the variable crystal structure of the elements distort the lattice of MPEAs. In a completely disordered solid solution, any element can be occupying any site of the lattice, resulting in a completely distorted three-dimensional lattice structure.

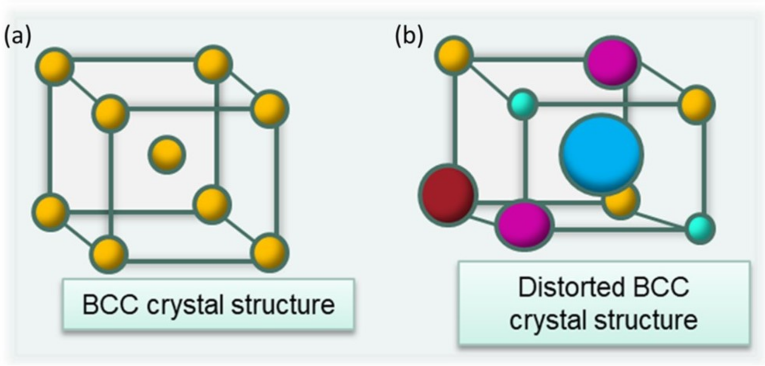

Figure 1.1.1: (a) Regular BCC crystal containing atoms of a single element. (b) Irregular BCC crystal containing atoms of different elements of different atomic sizes.

Because the alloy and its properties are related to the lattice structure and the elemental bonding, lattice distortion in MPEAs also affects various properties. Although understanding and determining the lattice distortion of these alloys has not been studied in detail, there are some works that show the relationship between lattice distortion and mechanical properties. For example, Senkov et al. [21] that MoNbTaVW, a BCC MPEA, shows a hardness value three times higher than what was theoretically estimated. Most properties such as hardness can be theoretically estimated using the rule of mixture, which considers the mole fraction of each element and their contribution to the properties. Ideally, the rule of mixture is used for composites. In a single-phase system, a solid solution can be considered equivalent to an atomic-scale composite, and thus the rule of mixture is applicable. However, for MPEAs, the distortion in the lattice structure due to the different sizes of the site occupants makes it deviate from the rule of mixture. The deviation is reported for the FCC system CoCrFeMnNi [33]. The lattice distortion results in a distortion strain and, in turn, modifies the solid solution hardening of the system. The thermal conductivity is also affected by the lattice distortion as the phonon scattering increases. Thus, in MPEAs, as the lattice becomes more distorted, the strengthening or solid solution hardening in the alloy improves.

1.1.3 Diffusion

In MPEAs, the equiatomic and close-to-equiatomic compositions do not allow for a specific solute and solvent distinction. In contrast, the whole system is equivalent to a solute matrix. This results in vacancies having more restricted motions that involve a higher activation energy. In fact, all defects require a higher activation energy to move in this matrix. This is in contrast to a binary alloy where there is a distinct solute and solvent demarcation.

Tsai et al. [34] reported that sluggish diffusion is a function of the number of elements in the system. However, Divinski et al. [25] showed that such a concept is not universally applicable. The tracer technique proved that MPEAs are majorly affected by atomic correlations and interactions. The effect of sluggish diffusion is reported for the alloy family AlCoCrFeNi [35, 36]. However, it was proven that the sluggish diffusion was similar to the diffusion caused by the ordering tendencies of certain species in this MPEA. That could be aided by fast diffusing species resulting in enrichment of other species, or by slow diffusing species themselves. An extensive study on CoCrFeNi alloys shows that sluggish diffusion is not always observed when tested using different tracers [37–39].

Furthermore, grain boundary diffusion also plays an important role, especially at elevated temperatures. The effect of the number of atoms along with their interactions does not necessarily slow down diffusion in the MPEA system. However, they allow enough opportunities for improving high temperature properties like strength and creep.

1.1.4 Cocktail effect

Ranganathan [40] proposed the idea of the cocktail effect, defined as the contribution of the properties of the individual constituent elements and phases to the overall properties of MPEAs.

As mentioned above, because single-phase and multiphase MPEAs can be compared to an atomic-scale composite, overall properties can be obtained from the rule of mixture. However, as discussed for MPEAs, the presence of different elements within the system results in competition in the enthalpy of mixing, different bonding energies, and lattice distortions as a result of elemental interactions. Together, these impact the properties of these alloys. These have a mixed effect on the MPEAs, making their properties very unique and sometimes unpredictable. Therefore, this effect is cause for scientific curiosity and investigation.

Yeh [41] studied this effect in detail on a varying Al-containing CoCrCuFeAl system, which shows the transition from FCC to BCC phase beyond a critical Al content. The enhanced yield strength at high temperatures and the higher resistance to softening in MoNbTaW and MoNbTaVW can also be explained due to the cocktail effect [21]. An alloy with an optimal combination of mechanical, electrical and magnetic properties was reported to be $\mathrm{CoNiFe(AlSi)}_{0-0.8}$ by Zhang et al. [42]. These alloys, especially those containing 0.2 wt% of Al and Si, have enhanced plasticity and strength together with increased magnetisation and electric resistance due to the cocktail effect.

These factors are considered stepping stones for formulating and understanding MPEAs. These effects impact the thermodynamic and mechanical properties and stability of the MPEAs.

1.2 Thermodynamics of alloys

1.2.1 Regular solution of binary alloys

Thermodynamics defines the free energy of a state (G) as a function of the enthalpy of the system (H), the entropy of the system (S), and the temperature of the system (T). A change in thermodynamic state as given by Δ is:

$$\Delta G = \Delta H - T\Delta S \tag{1.2.1}$$

An ideal solution is considered to be the mixing of two different elements where the enthalpy of mixing ΔH_{mix} or the interaction energy of the mixing atoms is 0. The entropy of mixing is the primary contributing factor for Gibb's free energy (G_{mix}^{ideal}):

$$\Delta G_{mix}^{ideal} = -T\Delta S_{mix}^{ideal} \tag{1.2.2}$$

The entropy of mixing ΔS_{mix}^{ideal} is the measure of randomness in the mixture with $S = k_B \ln|\Omega|$, where Ω measures the random distribution of elements in the system and k_B is the Boltzmann constant. The entropy (S) includes the thermal and configurational entropy of the system. Thermal entropy (S_{ther}) involves the vibrational, electronic, and magnetic entropy of the atoms, and configurational entropy involves the arrangement of the atoms. One of the most important factors is the configurational entropy (S_{conf}), which measures the number of ways the atoms in a mixture can be arranged. S_{ther} can be considered negligible if the change in heat or volume during mixing is negligible. Then, the primary factor contributing to the entropy of mixing is the configurational entropy.

In a binary solution or mixture of atoms type A and type B where the mole fraction of A in the solution X_A and that of B is X_B sums up to be 1, the ΔS_{mix}^{ideal} is given as:

$$\Delta S_{mix}^{ideal} = R(X_A \ln|X_A| + X_B \ln|X_B|) \tag{1.2.3}$$

R is the molar gas constant that is related to k_B and Avogadro's number N_A: $R = k_B/N_A$ However, in reality, no solution or mixture is ideal, suggesting that the energy of mixing, ie, the enthalpy of mixing ΔH_{mix}^{ideal} is nonzero according to the quasichemical model [32]. This model suggests that for a constant volume of A and B in a mixture or solution, the bond energy of the neighbouring atoms contributes to the enthalpy of mixing. In a binary solution, the bond energies are given as ϵ_{AA} between A and A, ϵ_{BB} between B and B atoms, and ϵ_{AB} between A and B atoms. The internal bond energy for a binary mixture is given as:

$$\epsilon = \frac{\epsilon_{AB} - 1}{\epsilon_{AA} + \epsilon_{BB}} \tag{1.2.4}$$

The enthalpy of mixing(ΔH_{mix}), being independent of the interatomic distances between the neighbouring atoms is thus given as:

$$\Delta H_{mix} = \Omega X_A X_B \tag{1.2.5}$$

where $\Omega = ZN\epsilon$; N is the number of bonds between the type A and B of atoms and among themselves and Z is the number of coordinations of the given lattice system. The free energy of a regular solution model can thus be written as:

$$\begin{aligned} \Delta G_{mix} &= \Delta H_{mix} - T\Delta S_{mix} \\ &= \Omega X_A X_B + RT(X_A \ln|X_A| + X_B \ln|X_B|) \end{aligned} \tag{1.2.6}$$

A non-ideal solution of atoms follows the regular solution model, in which if $\epsilon < 0$ the atoms of opposite types tend to be together, making a more random solution, while for

$\epsilon > 0$ the atoms of the same types tend to cluster together resulting in a more ordered or clustered state [17, 32].

The other important factor that determines the stable state and the lowest free energy of the system is the temperature. For a system with $\Delta H_{mix} < 0$ for all temperatures, the system has a random distribution of atoms that results in no order. However, systems having $\Delta H_{mix} > 0$ complicate the situation. At lower temperatures, ΔG_{mix} for such a situation is positive, resulting in a clustered or phase-separated spinoidal state that is unstable and returns to a stable disordered state at higher temperatures. The degree of clustering will decrease with increasing temperature to establish the importance of entropy. These regular solution models are binary alloys, equiatomic or non-equiatomic. Systems with very high positive ΔH_{mix} tend to separate into elements and not form solid solutions. A stable solid solution requires high entropy and lower enthalpy of mixing. The entropy comes into play more significantly as the number of components in the system increase. This stands as the backbone of multi-principal elements system, thus popularly known as the high entropy alloys.

1.2.2 Thermodynamics in Multi-Principal Entropy Alloy

According to the Gibbs phase rule, the increase in the number of elements results in increased possibilities of forming intermetallic phases, an element-rich solid solution, clustering, or a random solid solution. The formation of a stable solid solution is governed by minimising the free energy at constant temperature and pressure. For an ideal solution, the decisive factor is the entropy of the system. For a regular solution, the enthalpy of mixing comes into play, as discussed earlier. Most solid solutions formed are, however, subregular solutions, which do not have a completely random distribution of atoms. Such a distribution results in phase separation if the enthalpy of mixing is positive, and short-range ordering if the enthalpy of mixing is negative. The lowering of free energy to obtain an energetically stable system can be due to a higher positive entropy of mixing or a large negative enthalpy of mixing. However, the large negative enthalpy of mixing competes with the enthalpy of formation of intermetallic, thus destabilising the high-entropy system [4, 7, 8]

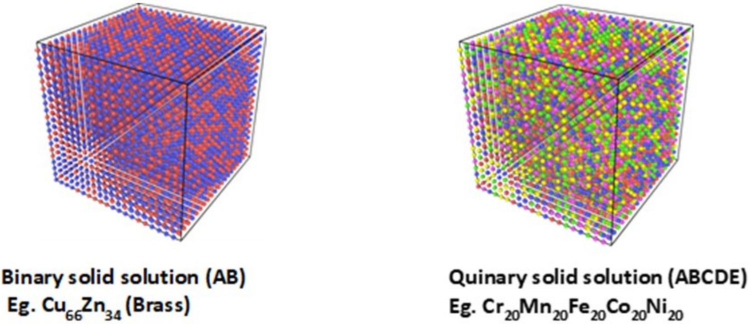
Binary solid solution (AB)
Eg. $Cu_{66}Zn_{34}$ (Brass)

Quinary solid solution (ABCDE)
Eg. $Cr_{20}Mn_{20}Fe_{20}Co_{20}Ni_{20}$

Figure 1.2.1: Conceptualised structure of a complete random solid solution of BCC binary and quinary system in which each colour on the structures represents a pure element.

.

Yeh et al. [3] suggested that the increase in configurational entropy will enhance the chances that solid solution counteracts the formation of intermetallic phases or atom clusters (figure 1.2.1). This is the underlying presumption for high-entropy alloys, where more than four equiatomic elements make up the alloys. The increased number of elements increases the configurational entropy according to equation 1.2.7 where ΔS_{max} is the mixing configuration entropy, and X_i is the molar fraction of the element i.

$$\Delta S_{mix} = -R \sum X_i \ln |X_i| \tag{1.2.7}$$

However, it has been noted that the equiatomic composition does increase the configurational entropy, but it is not a decisive factor for a random solid solution. The important factors other than configurational entropy are the low mixing enthalpy of the system or the low formation enthalpy of the intermetallic material apart from valence electron concentration, size misfit, or electronegativity.

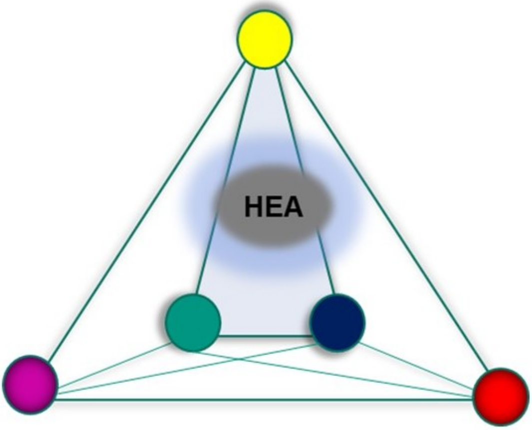

Figure 1.2.2: The schematics represent the possibilities of various fractions of alloying for a quinary system where each apex represents an element. The region marked in grey represents the varied equiatomic alloys that can be formed and the blue region around represents the possibility of MPEAs with non-equiatomic compositions. The lines represent the possible binaries of different compositions between the elements.

There are many non-equiatomic alloys that form stable single phase solid solutions due to low enthalpy of the system and not just high entropy, such as $Al_{20}Li_{20}Mg_{10}Sc_{20}Ti_{30}$, $Cu_{0.5}NiCoAl_{0.5}Fe_{1,2,3,3.5}$, $FeNi_2CrCuAl_{0.6}$ [18–20]. These alloys are more enthalpy-stabilised than entropy-stabilised. This allows a wide range of alloy compositions to be considered for a stable solid solution as shown in figure 1.2.2. Where most random solid solutions can be stabilised due to the high positive entropy of mixing and the large negative enthalpy of mixing, in some cases, a very large negative enthalpy of mixing can also destabilise the system and aid the formation of intermetallic. Therefore, the competition to form a stable random solid solution prevails.

Thermodynamic stability, as discussed, is a function of the enthalpy and entropy of the system along with the temperature. When the enthalpy of mixing is less than zero, the system has a tendency of ordering, and when the enthalpy of mixing is more than zero, the elements separate and do not form a solid solution. The presence of more elements in the system increases the entropy, which in turn counterbalances the effect of enthalpy, resulting in a stable solid solution.

An apparent idea from the basic thermodynamic equation 1.2.7 is that as the number of elements in the system increases, the configuration entropy increases, so the alloy becomes more stable and easily obtains a random solid solution. However, that is not always valid. Such alloys can exhibit short-range ordering, which is a precursor to long-range ordering at a much lower temperature. It has been studied that such multi-elemental alloys are not just stabilised by configurational entropy, but also the mixing enthalpy, vibrational and electronic entropy, and other thermodynamic parameters play a crucial role in stabilising the system [6].

Following the basic thermodynamic principles, the entropy itself can lower the free energy of the system for a system with no enthalpy in action, only for an ideal solution. The entropic contribution comes from the large number and size of atoms along with electronic, magnetic, and vibrational effects.

1.3 Mechanical stability of BCC Alloys

Mechanical stability can be defined in different ways in different principles and disciplines. In this work, mechanical stability of a material is defined as the ability of the materials to sustain the mechanical stress and impact without undergoing drastic failure or sudden phase change. Multi-principal elements systems as discussed earlier are complicated systems and understanding the mechanical stability of these systems is challenging and interesting. MPEAs are strategically designed and developed to exhibit specific properties like high strength over a wide temperature range, deformation resistance at extremely low temperatures, or creep resistance, to mention a few [6]. Therefore it becomes mandatory to investigate and understand the mechanical stability of these alloys, pertaining to deformation mechanism and behaviour at different temperatures and strain conditions.

Refractory MPEAs are usually of BCC structure and designed to support high temperatures with viable strength and ductility. It should be noted that the BCC crystallographic structure is not a closed-packed structure but has a defined closed-packed direction of $\langle 111 \rangle$. $\{110\}$, $\{112\}$ and $\{123\}$ planes allow for slip in the BCC, resulting in 48 slip systems. With more voids and fewer independent slip systems, the dislocation flow is more complex in BCC crystal systems than in the FCC crystal system. With the presence of multi-principle elements in the structure, the investigation of the mechanical stability of these systems becomes inevitable.

1.3.1 Nucleation of Dislocation

Cottrell [44] in 1953 estimated that the energy required under severe stress to nucleate a dislocation without any prior defect is very large. The activation energy for nucleating a dislocation is a function of dislocation loop size and shear stress applied. In order to obtain a critical size

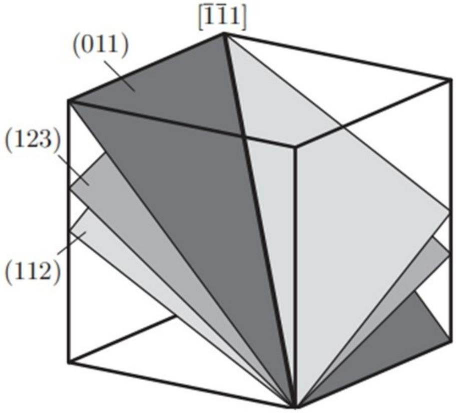

Figure 1.3.1: The schematic shows the BCC structure with its various slip planes. The important slip planes of BCC (011), (123) and (112) are shown here with the slip direction ⟨111⟩ [43].

of the dislocation for a stable nucleation without thermal fluctuation, it is reported to be around 10 eV for pure metals [45]. The thermal fluctuations help in nucleating a dislocation, but the energy aided by thermal fluctuation is only one-thousandth of the required shear stress to overcome the Peierls barrier.

$$E_c = \frac{1}{4} G b^2 r_c [\ln |\frac{2r_c}{r_o}| - 1] \tag{1.3.1}$$

E_c is the energy required to nucleate a dislocation of the critical core radius r_c that has a shear modulus G and a Burgers vector b. Peierls barrier is the energy barrier that a dislocation is required to overcome in order to move to the neighbouring plane. The energy required for this moving from one plane to another is known as the Peierls stress (equation 1.3.1).

In the presence of preexisting dislocations, the stress field interaction lowers the Peierls stress to aid the generation of new dislocations. For the dislocation to nucleate the maximum resolved shear stress $\tau_{\max}$ in that plane should be equal to the theoretical resolved shear stress τ_{th}. The theoretical resolved shear stress τ_{th} is usually calculated to be $G/2\pi$, where it is a function of temperature and interatomic bonds between atoms and crystallographic orientation if the system in question is anisotropic in nature. The τ_{th} is the maximum calculated energy required to allow dislocation nucleation. The τ_{max} required for dislocation nucleation is reduced with aiding agents such as thermal fluctuations or defects. When the nucleation is not largely affected by surrounding defects or thermal fluctuations but by small existing defects, such as vacancies, the shear stress in the range of one-seventh to one-tenth of the shear modulus is sufficient to initiate the nucleation.

The dislocation nucleation can be homogeneous or heterogeneous. Homogeneous nucleation of the dislocation occurs in a defect-free crystalline material under mechanical or thermal energy. Under sufficient energy, dislocations are formed that bring about plastic deformation. In contrast, heterogeneous nucleation of the dislocation is more common and energetically favourable. The presence of various defects reduces the energy barrier required for dislocation nucleation. Such nucleation is aided by impurities, grain boundaries, vacancies, and other pre-existing defects.

The dislocation nucleation as well as the movement is a function of the crystallographic system. Different crystallographic structures have a different number of active slip planes and varying Peierls stress, thus affecting the dislocations in these systems. As the work investigates refractory alloys that predominantly have a BCC crystal structure, dislocations in the BCC structure are discussed in detail in subsection 1.3.3.

1.3.2 Motion of Dislocation

The motion of the dislocations causes plastic deformation. The unrestricted movement of the dislocation allows for easy deformation and thus high ductility. On the other hand, a more obstructed movement of the dislocation results in strain hardening of the system. When the critically resolved shear stress is achieved in the closed-packed plane and direction, the dislocations get enough energy to move. The movement, multiplication, and generation of more new dislocations result in permanent deformation. The energy required is to overcome the Peierls barrier. The Peierls barrier can be defined as an intrinsic barrier that a dislocation requires to overcome in order to glide to the next closed-packed plane or low-indexed crystallographic direction. A more workable material is preferred to have a good combination of ductility and hardening.

The higher Peierls stress restricts the dislocation motion, resulting in reduced ductility and plasticity and an increase in strengthening. In addition, other obstacles, such as precipitates and interstitials, can increase the strength of the materials by restricting the motion of the dislocations. The climb is primarily achieved by the edge dislocations, which are aided by the availability of vacancies and temperature. Screw dislocation, on the other hand, can easily cross-slip to another glide plane [46, 47].

In order to allow dislocation movement leading to glide, close-packed planes and low-indexed crystallographic directions are preferred. These close-packed planes and directions vary for different crystallography. For FCC, the dislocation slip takes place on plane $\{111\}$ and direction (110). For HCP, the plane and direction change to $\{0001\}$ basal plane and [2110]. There can be numerous combinations of these planes and directions.

1.3.3 Dislocations in BCC

BCC crystal system is an open structure with a packing density of 68% in comparison to FCC, which has a packing density of 74%. The favourable planes with the lowest critical resolved shear stress are combinations of $\{110\}$, $\{112\}$ and $\{123\}$ (figure 1.3.1). The slip occurs in the $\langle 111\rangle$ direction on these planes, making $\langle 111\rangle\frac{a}{2}$ the Burgers vector for a complete dislocation. $\{110\}$ is the most densely packed planes whereas $\{112\}$ are the main stack fault planes. In addition to these, at low strain rate or high temperature $\{123\}$ planes are also activated. The three-fold symmetry around the $\langle 111\rangle$ axis of screw dislocation and the high Peierls stress of BCCs make screw dislocation the determining factor for plasticity in BCC. The dislocation motion is usually seen as wavy slip lines because of the cross-slip of the screw dislocations in an open structure. As cross-slip is further aided by temperature, thermal contribution plays a pivotal role in the plasticity of the BCC crystal structure.

At low temperatures, without thermal assistance and an open structure, the motion of the screw dislocations is restricted on $\{110\}$. Along the $\{110\}$ planes, the dislocations with the Burgers vector $\frac{a}{2}[111]$ can interact and lower their strain energy by forming a pure edge dislocation which ends up in the (100) plane. Since (100) is not a close-packed plane, the accumulation of immobile dislocations leads to a reduction in plasticity in BCC elements and alloys at room temperature [49].

At low temperature with thermal assistance or at high strain rates, some transition elements such as iron with BCC crystal structure do show deformation twins. This usually occurs when slip systems are restricted and the fault stress is lower than a resolved shear stress for slip. For BCC, the Burgers vector for deformation twin is $\langle 111\rangle\frac{a}{6}$ on every successive plane of $\{112\}$. It has, however, been theoretically calculated that the presence of stable stacking faults is energetically not favoured and is experimentally

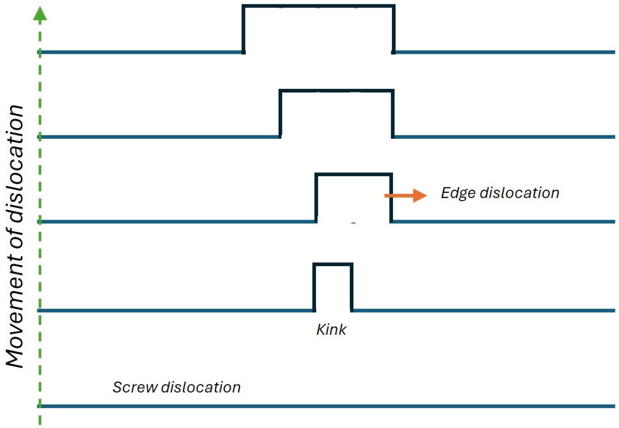

Figure 1.3.2: Schematic of propagation of screw dislocation (blue straight horizontal line) forming kink (black lines jutting out of screw dislocation) in BCC. The kink comprises of screw dislocation and two edge dislocations (vertical black lines). The movement of the edge dislocations aided the screw dislocation to propagate [47, 48].

never identified [49]. However, deformation twins as seen in BCC metals and alloys are favoured by low energy stable twin faults. These faults are generally normal to {112} [47]. The faults can generate at the point of obstructed slip plane. It can be further aided by the change in the local composition in a heterogeneous alloy which alters the planar fault making it energetically favourable than gliding of dislocations [50].

The type of line defect that nucleates at the elastic-plastic transition under load determines whether the BCC system will be brittle or ductile. Based on the wavy slip lines produced in the BCC system, Taylor and Elam [51] concluded that the pencil glide takes place on all zones containing the slip direction ⟨111⟩ family. However, a more detailed analysis showed that the dislocation glide takes place on

{110}, {112} and {123} glide planes. This results in a large number of glide systems that allow for easy cross-slip. The presence of an open structure restricts the easy glide motion of an edge dislocation. In addition, a complex three-dimensional core of a screw dislocation makes dislocation motion a more complicated process in BCC. In addition, the absence of possible stacking faults restricts the motion of dislocations and partials. This can lead to the formation of a three-layer twin along $\frac{1}{6}[111]$ under high stress, as proposed by Sleeswyk [52] and observed by Mahajan [53] in a molybdenum-rhenium alloy.

In the BCC system, the propagation of the dislocation is found to be not as a glide of a single straight dislocation line but as a kink pair. A kink originates when the dislocation moves partially into another plane parallel to the glide plane. The complicated motion of the otherwise immobile screw dislocation is aided by thermal activation by generating a pair of kinks and allowing the kinks to move under stress. This generates a thermally activated dislocation motion in the BCC crystal structures. Shockley [54] suggested that at a higher temperature, the dislocations can no longer be straight but form kinks. Kinks are short portions of the dislocation line that connect long straight dislocations (figure 1.3.2). As the kinks are in line with the Peierls valley, the energy required to overcome them is reduced with temperature and increased strain, and thus makes the dislocation motion more feasible.

The factor determining the deformation in BCC is the screw dislocation movement with a Burgers vector $\frac{a_o}{2}\langle 111\rangle$ below the knee temperature T_{knee} (figure 1.3.3). T_{knee} is the critical temperature below which plasticity in the BCC crystal structure depends on the kink pair mechanism [55]. Above T_{knee}, the motion of the dislocation is athermal and is not affected by the strain rate. The motion of the dislocation below T_{knee} is a function of temperature and strain rate, as it involves the overcoming of a high Peierls stress.

The three-fold $\langle 111 \rangle$ symmetry results in a non-planar screw dislocation [47, 56]. These screw dislocations require a higher Peierls stress than expected. The critically resolved shear stress reduces with temperature, making the Peierls barrier easy to overcome. It can also be noted that an increase in temperature thermally activates the screw dislocation as a pair of kinks. This is largely in contrast to the FCC system, where the Peierls stress required overcoming by the dislocations in motion is not high and the presence of stacking faults lowers the Peierls stress; thus temperature does not play an important role. Therefore, understanding the dislocation motion in a BCC system is best achieved by subjecting the materials to different strain rates and observing the strain rate sensitivity of the systems. Not only because the dislocation movement is a function of temperature and strain rate, but also because the thermal influence can be understood by varying the strain rate [48].

Seeger [48] gave a detailed description of the relationship of temperature and deformation rate below T_k with flow stress as seen in figure 1.3.3 for Nb. The non-planar screw dislocation rises the barrier for the dislocation to overcome. This barrier is overcome by generating a pair of kinks in opposite directions separated by a distance q. Below T_k, the microstrain regime is thermally activated (figure 1.3.3). At an exceedingly low temperature (denoted as lower bend temperature by Seeger [48]) the only activated cross-slip occurs in the (110) plane. Below the knee temperature and above the lower bend temperature, the microstrain segment can be divided into two interaction models, the line tension regime and the elastic interaction regime [58].

The rate-determining factor of the models at this regime is that the critical distance between the kink pair q_P should approach the separation of the Peierls valley a or the dislocation core length. The width of a is a function of the planes: $a_{110} = \frac{\sqrt{2}}{3}a_0$, $a_{112} = \sqrt{2}a_0$ and $a_{123} = \frac{\sqrt{8}}{3}a_0$.

Line tension regime For a considerably small kink whose

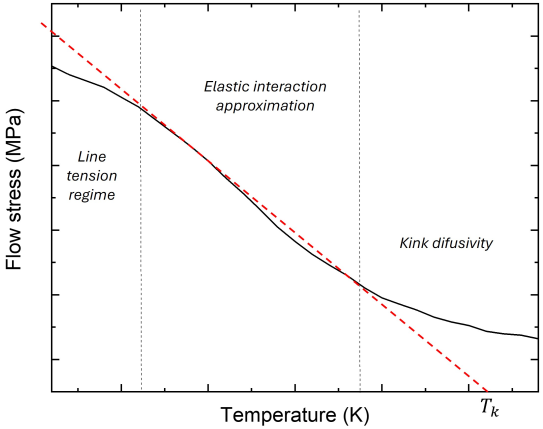

Figure 1.3.3: The different regimes of plastic interaction for Nb having a BCC crystal system as a function of temperature and strain rate has been reported by Seeger et al. [57]. At temperatures below T_k exhibits line tension regime or elastic interaction approximation regime. T_k is a function of strain rate.

separating distances are less q_P, the kinks follow the line tension model under applied shear stress for deformation (figure 1.3.4). At increased stress levels, the dislocation line between the two kink pairs bulges, allowing the curvature to be the dominant factor. This elastic energy of the dislocation is given by the line force or the line tension of the dislocation.

Elastic interaction regime In contrast, at low stress and below T_k, when the kink pair is more than q_P distance apart, their interaction can be considered as a Coulombic potential interaction (figure 1.3.4). On the large separation of the two semi-infinite kinks, the elastic energy between the two is given by the elastic interaction which gives the activated state of the dislocation between the two

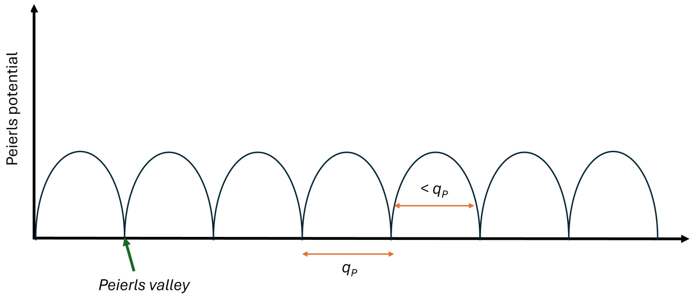

Figure 1.3.4: Graphical representation of Peierls potential indicating the Peierls valley. The gap between two Peierls valley is given as q_P. At the Peierls valley, the Peierls potential is 0 and indicates a dislocation plane.

Peierls potential minima.

In this regime at very low temperatures, dislocations can also be observed in the (110) plane. Beyond a certain critical temperature, the dislocations appear wavy in the (112) planes. This sudden change is attributed to the first-order phase transition commonly seen in BCC structures, where the Peierls width is reduced for (112) planes beyond this critical temperature. This change in the slip system in the BCC is normally observed as an anomalous slip. This anomalous slip can be mitigated by alloying as the presence of other elements can reduce the difference between screw and non-screw dislocation. The presence of impurities or foreign particles can also suppress this phenomenon, as impurities tend to pin the screw dislocation to (110) and allow its easy movement. These motions are thermally assisted and are highly strain rate sensitive [59].

Higher temperatures allow the kink pairs to attract each other and balance the shear stress, thereby reducing the thermal stress components. As a result, athermal stress components become predominant and thus the strain rate sensitivity reduces.

The systems can thus be experimentally analysed to determine the strain rate sensitivity and thus determine the dislocation motion regime that is active for the given temperature. The activation volume associated with it can also be calculated from the response to changes in the strain rate.

1.4 Motivation

Understanding the thermodynamics and mechanical stability of MPEAs is essential to engineer these alloys and enhance their properties as required. In order to understand the thermodynamic stability of the alloys and their phase transitions, detailed studies on MPEAs and their phase stability are required. The number of varied elements in these systems also affects the ordered and disordered phases as a function of temperature. Thus, this thesis aims to understand the effect of configurational entropy on the order-disorder phase transition as a function of temperature. The general goal is to provide a more general understanding of MPEAs.

The approach for understanding the order-disorder phase transition, as a function of the number of elements and temperature, involves mimicking the simple Potts model. The Potts model is typically used for studying ferromagnetic and non-ferromagnetic transitions in magnetic systems. The conditions of varying elements in the system are simulated using Monte Carlo simulations. The same is done for cooling as well as heating the system to show the effect of temperature variation.

For understanding the mechanical stability of MPEAs, this work focusses on experimental observation and analysis of BCC refractory MPEAs. The systems under investigation are stable and mostly single-phase refractory MPEAs that contain the elements Nb, Mo, Cr, Ti, and Al. The system has been designed so that Nb and Mo add to the resistance to high temperature, while Cr, Ti, and Al contribute to the resistance to oxidation [23]. The addition of Ti and Al also reduces the density of the alloys. Of all possible combinations of these elements in various compositions, the MPEAs NbMoCrTiAl, MoCrTiAl, and NbMoTiAl have been reported to be stable equimolar systems [60]. These MPEAs are reported to be fragile in macro-compression testing at room temperature, but their ductility increases at higher temperatures [60]. In comparison, TiNbHfZrTa is ductile at room temperature despite the crystallographic structure of BCC [21]. This thesis therefore focusses on understanding the mechanical stability of these three systems: NbMoCrTiAl, MoCrTiAl, and NbMoTiAl, compared to TiNbHfZrTa.

In this work, nanoindentation was used to study the mechanical stability of these systems. The aim is to understand not only the nanoscale properties but also the dislocation behaviours of the said alloys. Nanoindentation facilitates the testing of ductile as well as highly brittle materials such as refractory alloys, natural stones, and glass [61–68].

Thus, the following questions are addressed in this work:

1. It has been widely discussed that the entropy of mixing together with the enthalpy of mixing governs the thermodynamic stability of MPEAs. The configurational entropy still holds the basis for developing these genres of alloys. However, the question remains whether only the configurational entropy affects the thermodynamic stability of order-disorder phases in multicomponent alloys.

2. The lattice distortion is evident and unavoidable in MPEAs. This affects the solid solution strengthening and, eventually, the mechanical properties of the system. The question that needs to be answered is how it strengthens BCC refractory systems and its eventual effect on the mechanical properties of the system.

3. In addition to lattice distortion, the mechanical properties of refractory MPEAs can also be a function of temperature. BCC systems are known to show a thermally activated stress-initiated deformation mechanism. Therefore, the question is how to understand the temperature-related mechanical properties of refractory BCC MPEAs and the related plastic deformation mechanism.

4. Since MPEAs are influenced by their individual elements, it is to be studied how the cocktail effect of their

various elements affects the thermodynamic and mechanical stability of the system.

Chapter 2

Thermodynamic stability of MPEAs

"You should never be surprised by or feel the need to explain why any physical state is in a high entropy state"

Brian Greene

2.1 Introduction

2.1.1 Order-disorder transition in MPEAs

Alloys transition from long-range ordering to short-range ordering and finally to random order as the temperature increases from 0 K. Order can be defined as the patterning of atoms over a range of distances. Usually, a short-range order is defined for around 10 Å, above which it is considered a long-range order. The transition from short-range ordering to a complete random atomic arrangement is considered as an order-disorder transition. Krivoglaz et al. [69] and Stoloff et al. [70] consolidated the work on the order-disorder transition of alloys until the 1970s. The work has then expanded on the basis of a theoretical and experimental approach based on Cowley and Warren's theoretical method [71, 72].

For a binary system A_cB_{1-c} (where c is the concentration of molar fraction of the atom type A) the ordering is calculated based on the position of the atom type on a particular lattice site. The atomic configuration or position on a lattice site can be defined in three different ways: (i) Occupation of an atom type A is marked 1 otherwise 0, (ii) occupation of an atom type A at a site is given as +1, otherwise -1 similar to a spin variable, and (iii) Fourier series expansion of the concentration wave of an atomic configuration on a site.

Now, as the order-disorder transition is a function of temperature and configuration, identifying and therefore understanding the transition temperature from order to disorder state is important. This phase transition temperature can be calculated from thermodynamics and statistics. From thermodynamics, based on equation 1.2.1, the transition temperature can be estimated for a given enthalpy and entropy. However, since the configurational entropy is given as $-R\sum_{i=0}^{N} c_i \ln c_i$, for a concentration ($c$) of an element type i in an elemental alloy N, the transition entropy is calculated when the configurational entropy ΔS_c

changes as the ordering elements change from order to complete disordering in the system. However, calculating the entropy based on configuration using thermodynamics usually results in an overestimation or underestimation of the order-disorder transition temperature.

The other way to estimate the order-disorder transition temperature is using Monte Carlo simulations. The simulation calculates the change in configurational entropy ΔS_c using the change in the internal energy $U(T)$ for a given temperature or using the change in the internal energy as a function of the density of states $\ln g(E)$. The former follows the Metropolis Monte Carlo method as used in this work and the latter follows the Wang-Landau Monte Carlo method. In both methods, the specific heat is calculated as $\mathrm{d}U/\mathrm{d}T$ and the maxima of this derivative provide the order-disorder transition temperature of the system.

Understanding the ordering in such multi-principal elemental alloys has motivated numerous works on FCC-structured MPEAs, both experimentally and by thermodynamic modelling. One such system is the MoNbTaW, a refractory BCC MPEA, which exhibits an A2-type BCC lattice. Thermodynamic modelling of nearest-neighbour interaction has shown the presence of B2-type ordering in the BCC lattice with lattice preference by Ta and Nb on one site and Mo and W on the other. This phase separation or site specific segregation is energetically favoured at low temperatures, making this alloy a multi-phase solid solution below its order-disorder transition temperature, which is around 1600 K according to the mean field approximation. This drastically alters the mechanical properties of the system [73, 74].

A similar effect is seen in another BCC refractory MPEA NbMoCrTiAl and its derivatives [22]. XRD and differential scanning calorimetry revealed the ordered and disordered phases for NbMoCrTiAl, MoCrTiAl, NbMoTiAl, and TaMoCrTiAl. In what was presumed to be a single-phase A2 structured BCC alloy, the B2 ordered phase could be identified below a certain temperature. This is the order-disorder phase transition temperature. It can be seen that with an increase in the number of elements in system 4 (NbMoTiAl) to 5 (NbMoCrTiAl and TaMoCrTiAl), the transition temperature decreases. However, that is not observed for MoCrTiAl, whose transition temperature is higher than 5 component systems. Therefore, it can be comprehended that entropy plays an important role in lowering the transition temperature. However, for certain alloys, the other thermodynamic interactions can result in a change in the transition temperature that is not so predictable.

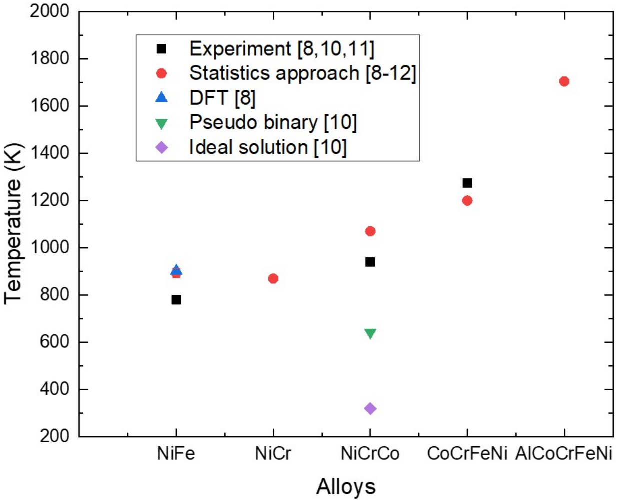

Figure 2.1.1: The order-disorder transition temperature calculated by various methods for FCC multi-principal elements alloys: NiFe, NiCr, NiCrCo, CoCrFeNi and AlCoCrFeNi, representing 2, 3, 4, and 5 component systems respectively [75–79].

The thermodynamic model of the order-disorder transition with the increasing number of elements in the system can be seen in figure 2.1.1. As the number of elements in the FCC ALCoCrFeNi increases from 2 to 5, the transition temperature gradually increases. Transition temperatures are obtained by various methods, such as experiments, density function theory (DFT), or statistical calculations using MC simulations [75–79]. However, all the transition temperatures for all the systems have been reported using the statistical method, which shows that the transition temperature for this family of alloys is increasing with increasing number of elements in the system. This is in comparison to the BCC alloys reported in the previous paragraph. This triggers two observations. Either the increase in configurational entropy is not the only triggering factor controlling the order-disorder transition, or the order-disorder transition temperature has different controlling parameters depending on the crystal structure.

Thus, the material community tries to understand the order-disorder transition in alloys, especially for MPEAs or HEAs, because many thermodynamic factors influence these systems. However, some systems such as NbMoCrTiAl and its family show the effect of entropy on the transition temperature, whereas alloy families such as AlFeCrCoNi do not exhibit the same. This motivated the work to understand the thermodynamics of the order-disorder transition as a function of only the configurational and mixing entropy. The aim is to gain more insight into the stability of the order-disorder transition as a function of entropy, which is supposed to be a key thermodynamic factor for MPEAs.

2.1.2 Regular solution of multi-principal element system

The regular solution model is well developed for the binary alloy system. This model is further extended for complex alloys. Meijering [80] studied the ternary regular solution model in the early 1950s which was extended to a multicomponent system by Morral and Chen [81]. The models are based on a single-phase system, which means a completely random or disordered distribution of elements except for the miscibility gaps. The primary assumption for the model was considering the binary interaction parameters to be positive and equal. Based on the regular solution model of the binary system, the regular solution equations for systems with n number of elements in the system for the enthalpy of mixing (ΔH^{n}_{mix}) and the entropy of mixing (ΔS^{n}_{mix}) can be rewritten in terms of the interaction parameter w_{ij} for an equiatomic composition with a single constant interaction parameter:

$$\Delta H^{n}_{mix} = \frac{n-1}{2nw_{ij}} \tag{2.1.1}$$

$$\Delta S^{n}_{mix} = R \ln |n| \tag{2.1.2}$$

For n number of elements in the system. The critical temperature for binary miscibility can be calculated from $T^{c}_{2} = \frac{w}{2R}$. The critical temperature here indicates the temperature at which the phase separation can be expected. The most basic assumption in calculating and understanding the phase change and critical temperature in alloys with a different number of components is that all interaction parameters are equal.

It should be noted that, according to Bragg Williams theory [82], the critical temperature of miscibility (T^{c}_{2}) and the chemical spinoidal temperature are the same for a binary equiatomic system (T^{S}_{2}). The miscibility point is the temperature below which a single-phase solid solution is absent, whereas the spinoidal point is the temperature at which phase separation takes place due to thermal fluctuations. The difference between the two increases with an increase in the composition of the system. As the temperature decreases, the miscibility gap for a fixed number of components in the system decreases, leading to phase separation. The eutectoid temperature of alloys with increasing components in the system with respect to the critical temperature of the binary system also increases. Also, as the system moves from binary to higher composition, the difference between the miscibility gap and the critical temperature of the spinoidal temperature increases. The spinoidal point temperature for the n component system can be given as

$$T_n^c = w/nR \tag{2.1.3}$$

The spinoidal temperature can be considered equivalent to the critical temperature of the order-disorder transition. As discussed earlier, this transition temperature is an underestimation of the true transition temperature. Although this method caters to all the entropy in a system, the assumption in most situations is that only the configurational entropy is calculated.

2.1.3 Potts model

Ising developed a model to understand the ferromagnetic to non-magnetic transition and to identify the critical temperature for a two-dimensional square lattice [83, 84]. The analysis focusses on the nearest neighbour interaction having two types of spin known as 2 states: up spin and down spin. In general terminology, the states or the numbers of spins are termed as q and the system described is referred to as q state system. This was further developed by Potts to be applicable for nearest-neighbour interaction for different states, i.e. having different spin states. For a 2D square lattice, Potts derived the ratio of the interaction energy and the transition temperature as a function of the states q [85].

$$\frac{2J}{k_B T_c} = \ln|1 + \sqrt{r}| \tag{2.1.4}$$

where, J is the interaction energy, T_c is the critical temperature, and r is the number of configurations for a unit. Each configuration can be written in terms of vector where the angle between two points is given by $\frac{360}{r}$ this ratio of interacting energy and the critical temperature for $r = 2, 3$ and 4 is noted as 0.88, 1.01 and 1.76 respectively [85]. The vector Potts model for $q = 2$ is actually the classical Ising model. For $q \to \infty$, the model is modified as the XY model. The Ising and Potts model was extended further to the two- and three-dimensional systems for different complex network systems using Monte Carlo simulations by Herrero [86].

Tobochink [87], reported that the energy of the Potts model is a function of the total number of spins in the system. The smaller lattice block with an increased spin system for a given q state shows a higher interaction. The MC renormalisation group (MCRG) [88] accurately determines the critical points. The energy average is calculated for two same lattice blocks having different spin states. If the temperatures of the two systems are T_1 and T_2 then

$$\Delta T = T_2 - T_1 \tag{2.1.5}$$

If $\Delta T = 0$, then it is a critical point. $\Delta T > 0$ indicates disordered phase and $\Delta T < 1$ indicates the ordered phase.

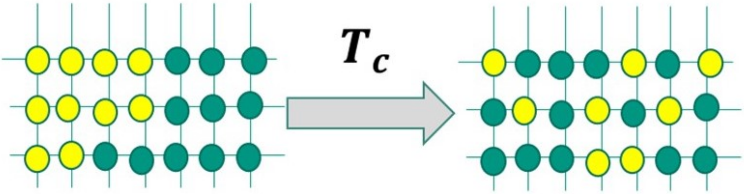

Figure 2.1.2: The illustrated images show the transition from ordered structure (where similar atoms tend to remain together) to disordered structure (where dissimilar atoms tend to remain together) on heating at the transition temperature.

The two-dimensional Potts model with q components shows the first-order transition for $q > 4$ and the higher-order transition for $q \leq 4$ for the square lattice [89, 90]. However, the three-dimensional Potts model with 3 states shows a first-order transition with second-order transition behaviour superposed. The transition type is identified by comparing the change in energy (E) in the temperature range and the specific heat ($\mathrm{d}E/\mathrm{d}T$) over the same temperature range. The specific heat is three times greater for the $q = 4$ state than for $q = 3$ [91–93].

Binder [90] reported that a detailed study of the static and dynamic phenomena of the critical transition for the 2D Potts model was reported by Binder [90]. The studies were carried out on a square grid for states 3, 4, 5, and 6 of q with a grid size of 16×16 and 200×200 and 1000 MC steps. The static property of the order parameter is given as:

$$M(t) = q\frac{N_1(t)}{N-1}/q - 1 \tag{2.1.6}$$

where N_x is the number of sites with a particular spin at a given time t of the simulation [90, 94, 95]. The critical energy for the systems is in agreement with Baxter [89]. The transition temperature is inversely proportional to the q state. For $q = 5, 6$ as reported earlier show the first-order transition at the critical point. It was also noticed that a lower q state resulted in a gradual transition at the critical temperature of larger q states. Binder also developed a kinetic model in which a critical slowdown is observed and no metastable state is obtained. In addition, a longer simulation time was noted to reduce hysteresis.

Bonfim [96] used the 3D Potts model in the cubic system by extending the Hamiltonian given by Ferrenberg [88] and Swendsen [97], using the histogram. It was applied on three different state models that vary the lattice size from 3 to 15 whose transition temperature for infinite lattice is 1.817 ± 0.001. The transition temperature is reported to be a function of the lattice size [98, 99].

The Potts model gives a thermodynamic approach to transition temperature and energy for a defined lattice where the q states represent the spin states that can vary from 2 (usually 180° apart) to ∞ (meaning the angle of difference is minuscule). If considered, the q state represents the different atoms instead of spins, then $q = 2$ indicates a binary system, and so on. The consideration of the lattice structure and the lowest energy state of the system, the transition from a uni-directional spins or ordered state to a randomly orientated spins or disorder state can be easily simulated and calculated.

The extensive development of Potts model to identify the transition temperature helps us to extend this model for an order-disorder transition that is not pertaining to the ferromagnetic to nonmagnetic transition. Drawing a similarity between spin movements in domains to the atomic movements in a lattice, the Potts model parameters can be extended and modified to obtain relevant understanding of energy and temperature transition from ordered to disordered atomic structure or vice versa during heating or cooling.

2.2 Methods

2.2.1 Potts model using Monte Carlo Simulations

This work utilises the Potts model to assess the entropic effect of systems where the number of constituents in the system is equivalent to the number of spins described by Potts and Ising. The model is simplified for calculating the order-disorder transition similar to the ferromagnetic to non-ferromagnetic transition known as the critical temperature in both cases. The number of possible constituent elements q is investigated in different atomic lattice environments, which is also described by coordination Z for different lattice structures. The modification is used to calculate the total interactive energy of atoms distributed in a lattice.

The q state Potts model was simplified to a Hamiltonian ($\hat{\mathcal{H}}$), reducing the complexity of various adjustable parameters. The Hamiltonian can be given as

$$\hat{\mathcal{H}}_i = J \sum_{ij} \delta_{ij} \tag{2.2.1}$$

where j is the total number of neighbouring sites of site i. This is a function of the lattice structure and the number of different components involved. δ_{ij} is a Kronecker delta that is 0 for the interactive bond energy for similar atoms at site i and neighbouring site j. δ_{ij} is 1 for the interactive bond energy for dissimilar atoms at site i and neighbouring site j. The models only account for nearest-neighbour interaction. J represents the interaction energy of the system having an arbitary energy unit.

At low temperatures, similar to the real thermodynamic conditions, the elements segregate into phases. As the temperature increases, the thermal effect results in randomisation of the components in the lattices resulting in a disordered solid solution. The entropic effect becomes prominent at this juncture, as the atomic bond enthalpy is considered 1 for all components of the system. This reduces the enthalpy of the system to 1 and therefore it does not contribute to the system in question. The Potts model, as discussed earlier, has been expanded from the 2D lattice to the 3D lattice and varied the q states. The q state for binary alloys is 2, 3 and 4 are similar to medium entropy alloys, and 5 to 8 can define a high entropy alloy. This work focusses on a 3D lattice with a q state ranging from 2 to 8 on different lattice systems such as simple cubic (SC) ($Z = 12$), body-centred cubic (BCC) ($Z = 8$), face-centred cubic (FCC) ($Z = 6$), and diamond structure ($Z = 4$). The sum of the Hamiltonian of all the sites is the energy of the system under simulation. This thesis further elucidates the order-disorder transition temperature calculation using different approaches, but such calculations are only performed on BCC systems in detail. The focus is on the effect of entropy on the critical temperature of the order-disorder transition in regular binary solutions, medium- and high-entropy alloys.

Monte Carlo Simulations

Monte Carlo (MC) simulations can simulate thermodynamics and statistical physics by using random numbers to sample the phase space of a Hamiltonian. The simulation runs on the smallest time unit called the Monte Carlo time step, and a lattice point is the Monte Carlo unit (MCU) that is randomly chosen. A new state is chosen for the MCU from the available $q - 1$ states and the energy difference between the new and old state is calculated. The q is the state of the system identified as the number of particles or spins or variables describing the system. The probability of the changed state is then given as:

$$\begin{aligned} p &= m, & \Delta E &\leq 0 \\ p &= m \exp[-\frac{\mathrm{d}E}{kT}] & \Delta E &> 0 \end{aligned} \tag{2.2.2}$$

where m is the change in state and E, for i^{th} MCU site and its nearest neighbour, the energy of a state is given as:

$$\hat{\mathcal{H}} = -J\sum_{i}^{mn}(\delta q_i q_j) \tag{2.2.3}$$

$\hat{\mathcal{H}}$ as defined in equation 2.2.3 is equivalent to the Hamiltonian ($\hat{\mathcal{H}}$) in equation 2.2.1 for this calculation.

The Monte Carlo follows two algorithms, namely, Rejection-Kinetic Monte Carlo (rKMC) or Rejection-Free Kinetic Monte Carlo (KMC). The rKMC is the standard algorithm and is defined by the sweep random algorithm. The sites in the system are randomly selected and the events are performed on the basis of the energetically favourable condition. The possible transition from i to j state does not follow any specific pattern. This speeds up the algorithm, and the calculation time is updated after every step. In comparison, the rejection-free KMC is much more thorough and considers all possible transitions from i to j state and the most probable transition is considered using binary search. The transition rate from state i to state j is considered for the rejection KMC whereas the probabilities of transition from state i to state j are considered for the rejection-free KMC as the rate determining step for the algorithm [100, 101].

The dynamics of the system can be either Glauber dynamics or Kawasaki dynamics. In Glauber dynamics, the spin changes at each step without conserving the total concentration of each q state throughout the simulation time. In contrast, Kawasaki dynamics preserves the total concentration of each q state at every spin change throughout the simulation time. Considering the simplest model for understanding the entropic effect, this work focusses on the use of Glauber dynamics [102, 103].

Monte Carlo simulations have been extended to understand long- and short-range ordering in some high-entropy alloys [104–106].

SPPARKS Simulator

SPPARKS (Stochastic Parallel PARticle Kinetic Simulator), a Monte Carlo simulator (Sandia National Laboratories, a US Department of Energy laboratory) is used for this work [107, 108]. This is based on rejection-free KMC in order to consider all possible transition states in the simulation. The algorithm follows a binary tree of probability. The random sweep algorithm allows the selection of sites that randomly resemble the original Potts model [84]. The algorithm is an in-lattice application that defines the rejection and acceptance criteria and executes the probable event. This work focusses on $20 \times 20 \times 20$ lattice size (n) of different coordination numbers, but mainly on BCC ($Z = 8$). The temperature (T) is calculated for the cooling or heating of the total lattice size, which is $20 \times 20 \times 20$ here. The unit of temperature defined by the simulator should be consistent with the energy definition of the system. Therefore, the unit of temperature in these simulations is J/k_B , J is the pre-defined interaction energy of the system [93]. Each system is subjected to a temperature range of $T = 0$ to $T = 6$ at an interval of $(\Delta T) = 0.1$. Under each temperature condition, the simulations were run for the 10^5 MC steps to obtain a stable system at the end of the temperature.

$$E = \frac{\hat{\mathcal{H}}}{n^3 Z m} \tag{2.2.4}$$

The energy per atom (E) is calculated as the energy of the system ($\hat{\mathcal{H}}$) divided by the lattice size (n), the coordination number of the system (Z) and the number of atoms per unit cell of the system (m) (equation 2.2.4). Similarly to Binder, the energy per atom (E) is averaged over 10^3 MC steps to avoid random fluctuations [90]. The transition temperature T_c is given as the temperature at which the energy per atom changes abruptly as shown in Figure 2.3.1. The order-disorder transition is determined in three different ways: (a) by regular solution calculation (pertaining to $q = 2$ or binary system), (b) by the order-disorder energy transition which is comparable to specific heat calculations, and (c) by determining the bond energy based on dissimilar neighbours and generating a phase diagram. The effect of various sizes of the lattice on the transition temperature is also observed, as well as the heating and cooling patterns of the systems on the critical temperature.

The lattice structure for all systems at different temperatures was observed using OVITO data visualisation and analysis software [109]. This software was used not only to visualise the changes that occurred in the various systems with time and temperature. It was used not only to identify the ordering and disordering in the system but also to reprogram and visualise the lattice with similar and dissimilar nearest-neighbour interactions to mimic the bond interaction of atoms.

2.3 Determining order-disorder transition

2.3.1 Regular solution and order-disorder transition

As defined by the regular solution model, especially for a binary system: with two different elements in a system, the transition temperature is when the system moves from an ordered or clustered phase to a randomly distributed state, where the atoms occupy any place in the lattice without a pattern. As discussed earlier, the internal energy or enthalpy, along with entropy and temperature, plays an important role in defining the order-disorder transition (equations 1.2.2 and 1.2.7). As the effect of enthalpy is not considered here, the transition temperature (T_C) is only a function of entropy. For a binary system, the regular solution equations given in equation 1.2.7 can be rewritten with the simulated parameters. As explained by Hill [110], comparing the thermodynamics of solutions with ferromagnetism, the enthalpy term can be rewritten in terms of the potential energy of interactions. This potential energy is not only the atomic bond interaction but also the interactive energy of two atoms at the nearest-neighbour site.

If the two types of atom are namely i and j then the interaction energy (J) is 0 for ϵ_{ii} and ϵ_{jj}, i.e., similar bonds and 1 for ϵ_{ij}, i.e., dissimilar bonds. The X_i and X_j, that is, the mole fraction of each element is the number of each element in the system at the simulation end of every temperature. Equations 2.1.1 and 2.1.2 can be rewritten as follows:

$$\Delta S_{mix} = X_i \ln |X_i| + X_j \ln |X_j| \tag{2.3.1}$$

$$\Delta H_{mix} = Z X_i X_j \left(\frac{\epsilon_{ij} - 1}{\epsilon_{ii} + \epsilon_{jj}}\right) \tag{2.3.2}$$

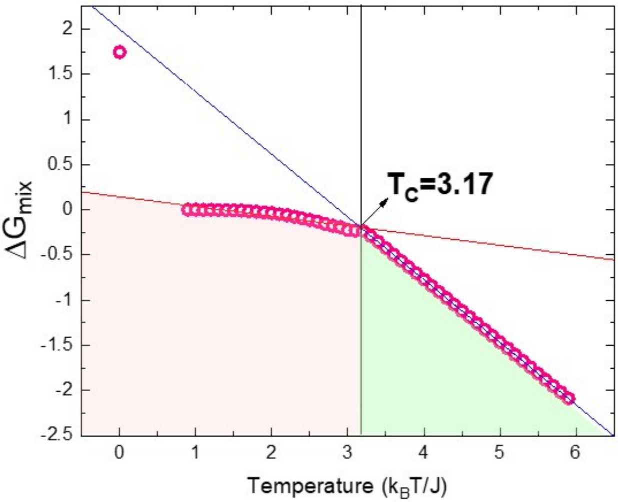

Figure 2.3.1: The free energy of mix plotted over a range of temperature ($T = 0$ to 6) for a binary system. The energy of the system is based on the change in entropy of the binary system and change in enthalpy. The similar neighbouring atoms having 0 energy and dissimilar neighbouring atoms having an energy value 1.

For a binary solution, if $\epsilon_{ii} + \epsilon_{jj} > \epsilon_{ij}$, the system prefers to be in a disordered solution, and if $\epsilon_{ii} + \epsilon_{jj} < \epsilon_{ij}$, the system is energetically favoured to be an ordered solution.

As explained earlier, since the bond interaction is 1 between the elements, the enthalpy effect comes only from the elemental fraction and the neighbour interaction. Using the above ΔS_{mix} and ΔH_{mix} for ΔG_{mix} (equation 1.2.2) the ΔG_{mix} vs T can be plotted as figure 2.3.1 for a binary solution. The temperature at which the free energy changes abruptly is the critical temperature calculated by this simulation for $q = 2$. The change in free energy is comparable to the calculations for the thermodynamic regular solution. Guttman et al. [111] listed the critical temperature (T_C) calculated using different methods for a 3D $q = 2$ system. The listed critical values are for an infinite crystal lattice but are similar to the result obtained from figure 2.3.1 i.e. $T = 3.17$.

As Herrmann reported [93], the change in the critical temperature (T_C) is not sensitive for a lattice size of 15 for a simple cubic 3D system. This is proven true for these simulations also, as seen in figure 2.3.3, where the energy/atom is plotted against temperature for a BCC system for q systems 2, 3 and 5 (systems containing 2, 3 and 5 species) having lattice size (n) 20, 60 and 120 [93]. Here, the sudden change in energy/atom (in figure 2.3.3) is seen to be consistent for the different q states and lattice sizes.

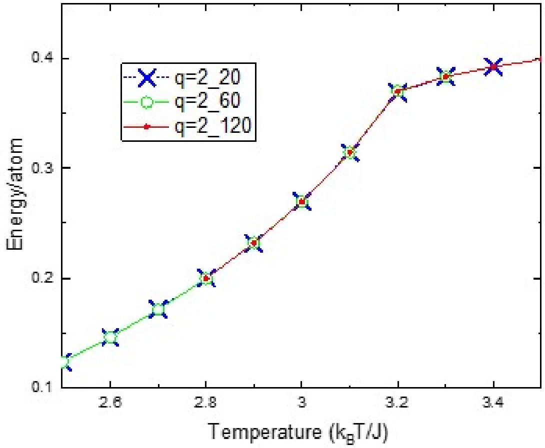

Figure 2.3.2: Energy/atom for BCC system with lattice size $20 \times 20 \times 20$, $60 \times 60 \times 60$, and $120 \times 120 \times 120$ for (a) $q = 2$ over a range of temperature. The plots show that the energy/atom over the temperature replicates despite the varying lattice size.

In a similar way, the critical temperature can be calculated

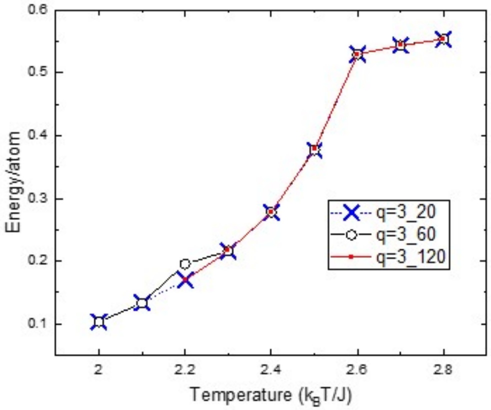

(a) $q = 3$

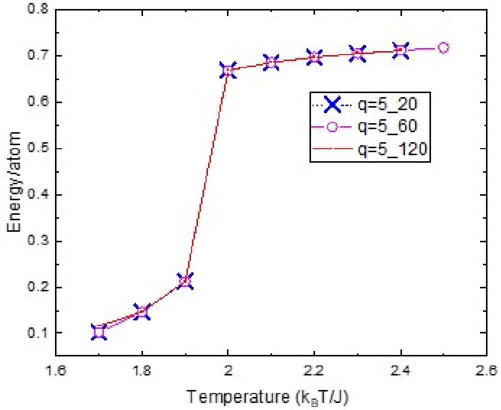

(b) $q = 5$

Figure 2.3.3: Energy/atom for BCC system with lattice size $20 \times 20 \times 20$, $60 \times 60 \times 60$, and $120 \times 120 \times 120$ for (a) $q = 3$ and (b) $q = 5$ over a range of temperature. The plots show that the energy/atom over the temperature replicates despite the varying lattice size.

for higher order q states using simple regular solution thermodynamic equations. However, as the equations become increasingly complicated with additional interactive parameters, the results are more difficult to calculate as well as can greatly underestimate or overestimate the critical temperature.

2.3.2 Energy and order-disorder transition

Figure 2.3.4 shows the energy/atom of a BCC system over a temperature range of $T = 0$ to $T = 6$. The temperature at which the abrupt change of energy can be noticed is the critical temperature for the order-disorder transition. The high-energy state is the completely disordered state and the low-energy state is the ordered state.

All systems were subjected to a temperature range of $T = 0$ to $T = 6$, but the heating protocol can be varied. The protocol can be that of overheating the system or undercooling the system. This in turn can affect the order-disorder transition. In the overheating protocol, the system, in the beginning, is in a stable 0 energy state and gradually heated to a required temperature and stabilised at that temperature. This avoids the random distribution of elements in the system at the beginning of simulations. In the undercooling protocol, the system is in complete disorder, which has the most stable energy of the system. The system is then rapidly undercooled and the required temperature is reached. Schebarchov et al. [112] proved that systems showing second- or higher-order transitions are not affected by undercooling or overheating protocols and energy data overlaps. However, for systems showing first-order transitions, there is always a hysteresis between overheating and undercooling of a system. Observing the energy/atom vs temperature in figure 2.3.5 and 2.3.6for binary, ternary and quinary systems, the hysteresis can be noticed in the five elements system.

During the overheating protocol, the system is heated up. At this point, the transition temperature (T_C) is

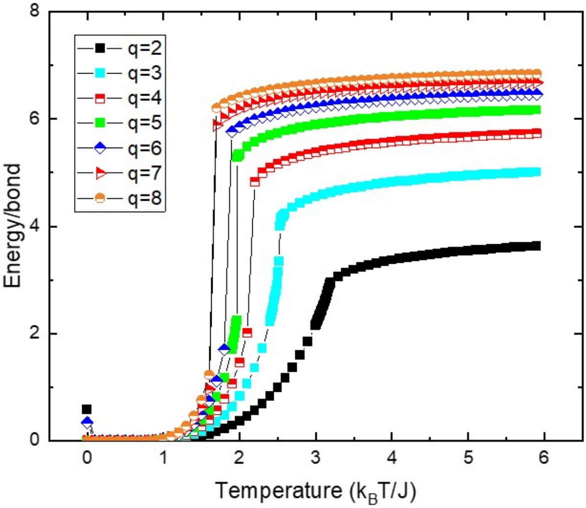

Figure 2.3.4: The energy/atom for BCC over a temperature range of $T = 0$ to $T = 6$ for a lattice size of $20 \times 20 \times 20$. The sharp transition of energy/atom at the temperature indicates the critical temperature T_c. Such a T_c is however absent for $q = 2$ and $q = 3$, which shows a gradual transition.

the lower limit of temperature at which the energy of the system changes. During the undercooling protocol, the upper limit of the temperature at which the abrupt energy change occurs is considered as T_C. As mentioned earlier, since this calculation uses the Glauber dynamics, the undercooling protocol is used further to understand the behaviour of disorder-order [102]. The T_C as obtained from the undercooling protocol is listed in table 2.3.1.

T_C can also be derived from the first-order transition of energy or energy/atom for a q state [90, 91]. The derivative is equivalent to determining the specific heat, and the sharp peak temperature at the singularity of the heat capacity

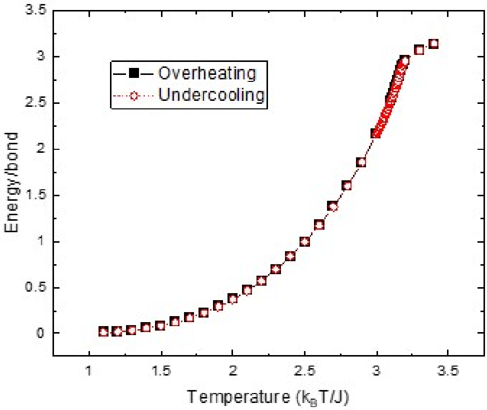

(a) BCC lattice for $q = 2$

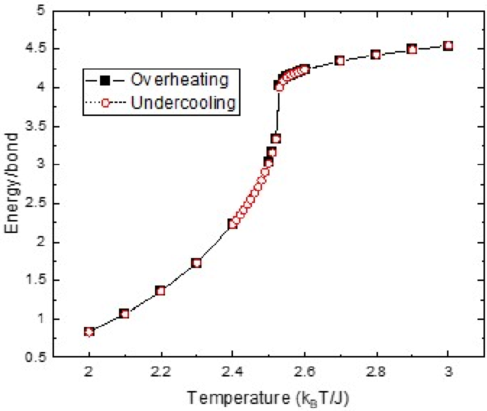

(b) BCC lattice for $q = 3$

Figure 2.3.5: The energy/atom for BCC over a temperature range of $T = 0$ to $T = 6$ for undercooling and overheating for (a) $q = 2$ and (b) $q = 3$ (binary and ternary elemental systems) do not show the hysteresis.

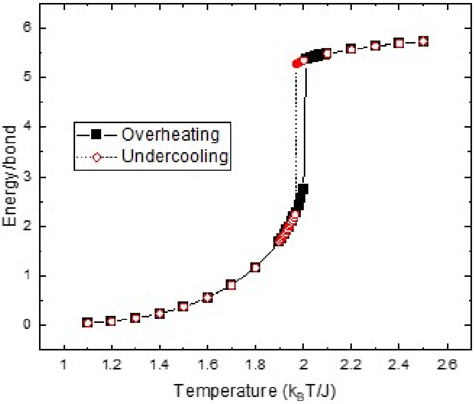

(a) BCC lattice for $q = 5$

Figure 2.3.6: The energy/atom for BCC over a temperature range of $T = 0$ to $T = 6$ for undercooling and overheating for $q = 5$ (quinary elemental systems) shows the hysteresis.

corresponds to T_C. The T_C for various q states are listed in table 2.3.1 and are represented graphically in figure 2.3.8. This is in accordance with Baxter [89, 90], who reported that q state of 5 or more shows a sharp first-order transition that makes identification of T_C easier. Scholten [91] reported that for a q-state clock model of a simple cubic 3D lattice, T_C becomes prominent. This is because as the q state increases, the transition becomes more prominently first-order. However, $q = 2$ does not exhibit a first-order transition, and Baxter [89, 90] explained that this is due to the gradual transition observed in binary solution.

Since in a binary system the spinoidal and miscibility points are the same as seen in the regular solution model, there is normally a gradual transition from order to disorder unless the enthalpy of mixing is very dominant. Therefore, T_C from the calculation of the energy / atom or the

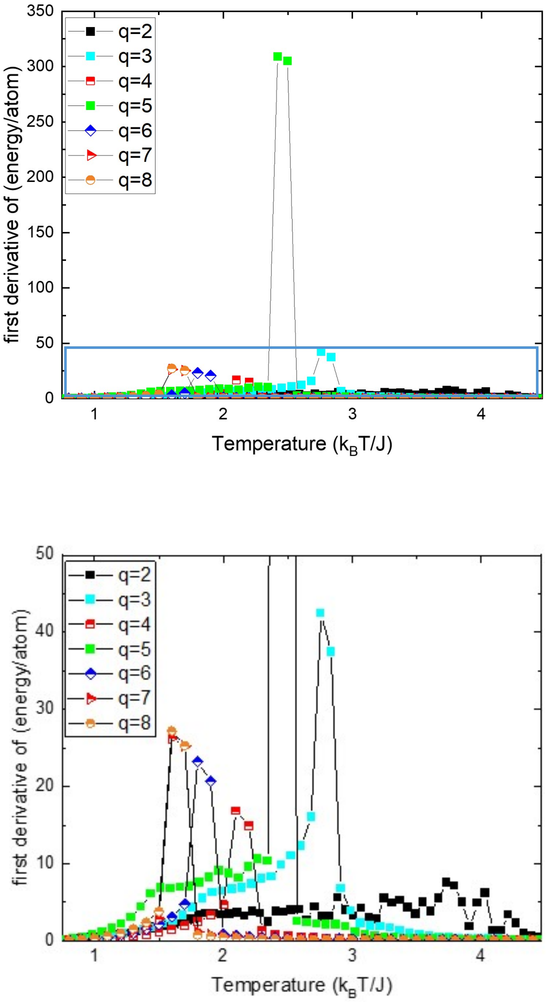

Figure 2.3.7: The first order derivation of energy/atom (heat capacity) over a temperature range of $T = 0$ to $T = 6$ indicates the transition temperature, especially for q states over 4 that specifically shows exhibit first-order transition.

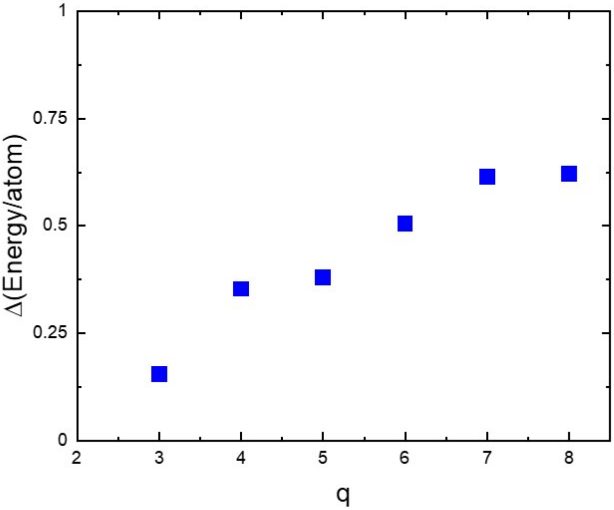

Figure 2.3.8: (a) Indicates the jump from an ordered to a disordered state and the change in the energy involved. (b) The change in energy/atom from the ordered to disordered state varies as a function of q states.

heat-specific transition for $q = 2$ is not deterministic. Baxter [89, 90] also reported that q states 3 and 4 could not be exclusively categorised as a first- or higher-order transition. Thus, determining T_C for q states 3 and 4 is also difficult.

As mentioned above, the data collected are over a temperature interval of $\Delta T = 0.1$. However, q states 2, 3, and 5 are the most important q states for investigation. The lack of first-order transition and the definition of the classical binary alloy make $q = 2$ an important q state to discuss. $q = 3$ and $q = 5$ are equivalent to medium-entropy alloy and high-entropy alloy, respectively, as these number of elements constitute the medium and high-entropy alloys. Therefore, these three systems were observed at temperature intervals of $\Delta T = 0.01$, in order to obtain a more

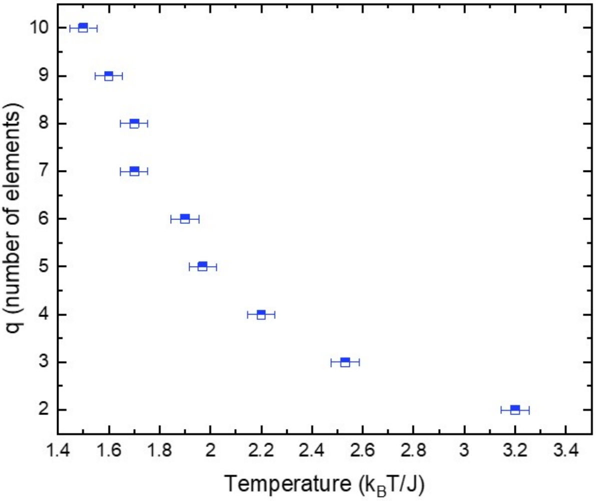

Figure 2.3.9: The order-disorder transition temperature decreases as a function of q states. This is true for all crystal structures, though only BCC crystal structure is indicated here.

specific T_C.

It can be noticed in figure 2.3.8a that the sudden transition in T_C shows a large energy difference (ΔEnergy/atom) between the ordered and disordered phase as the q state increases (figure 2.3.8(b)). The energy difference is almost negligible for the $q = 2$ state. It is in accordance with the regular solution model for multiple elements in a solid solution as reported by Mejering [80] and later by Morral et al. [81] where they indicated that the difference between the miscibility and spinoidal temperature increases with increase in q states or number of elements in the system and the spinoidal temperature keeps decreasing with increasing elements in the system. With a lack of bond interaction, the increased entropy stabilises the disordered phase at a lower temperature.

The change in T_C with the q states can be seen in figure 2.3.9. The energy/atom of a disordered state is proportional to the number of elements in the system or the q states (figure 2.3.13), and the relation is almost linear in nature. Once the disordered state is achieved, the increase in energy / atom as a function of temperature is similar for all q states in the investigation except for the binary state ($q = 2$). The gradual change in the order-disorder phase in $q = 2$ does not increase the energy of the system much as this temperature of the system increases for a binary solid solution.

However, it can be concluded that as the q state increases, the entropy of the systems helps the disorder-to-order transition happen at a lower temperature and more abruptly. This results in achieving a disorder solid solution at a lower temperature when multi-principal elements are present in the system. It can also be noticed that for a given temperature, as the q state increases, the energy of the disordered state also increases. The high energy as in $q = 7$ or $q = 8$ at the transition temperature or above does not help stabilise the system.

Therefore, in relation to the first-order transition that allows a distinct order-disorder transition, q states 4 and 5 prove to be more convenient. This helps us to explain the reason for most high-entropy alloys to be 4 or predominantly 5-element systems. The increasing q state increases the energy/atom in the disordered state. A stable disordered phase is equivalent to a completely random solid solution. An equiatomic 5-element system has high configurational entropy along with substantially low energy of disordered phase in comparison to the higher q-state systems and exhibits a singularity of heat capacity, allowing a distinct order and disordered phase. This helps us to conclude that, as the name suggests: as the high entropy alloy increases, the elements in the system favour entropy. It is also noted that as the elements in the system increase,

q	**Regular solution calculation**	**Energy/atom from Potts model**	**First-order transition of energy/atom**	**Bond energy and phase diagram**
2	3.17	3.2 ± 0.1	3.18 ± 0.1	3.00
3		2.53 ± 0.01	2.52 ± 0.01	2.45
4		2.2 ± 0.1	2.1 ± 0.1	2.12
5		1.97 ± 0.01	1.97 ± 0.01	1.96
6		1.9 ± 0.1	1.8 ± 0.1	1.83
7		1.7 ± 0.1	1.6 ± 0.1	1.65
8		1.7 ± 0.1	1.6 ± 0.1	1.64

Table 2.3.1: The order-disorder transition temperature evaluated for q states 2 to 8 using different methods.

the total energy of the system increases, resulting in higher energy of disordered state.

However, the above argument is without considering the enthalpy of interaction. It can be duly argued that for increasing elements in a system of 7 or more, if the enthalpy of the system can lower the total energy of the system, then a random solid solution can be stable even at low temperatures. For example, $Al_{0.5}CoCrCuFeNiTi_{0.2}$ [113], although it is a single phase FCC, not all elements in the system are equiatomic. There are alloys such as CuAlNiCoCrFeSi [3, 41], CuCoNiCrAlFeTiV [114], which have 7 or more elements in the system but lack a single phase solid solution. The most stable single-phase solid solutions at room temperature contain a maximum of 5 or 6 elements in the system. It could also be concluded that a more stable single-phase solid solution can be obtained from 5 to 6 different elements in a system like MPEAs as usually seen. However, it should be kept in mind that the transition temperature obtained using this method is an underestimation because the enthalpy of the elements is

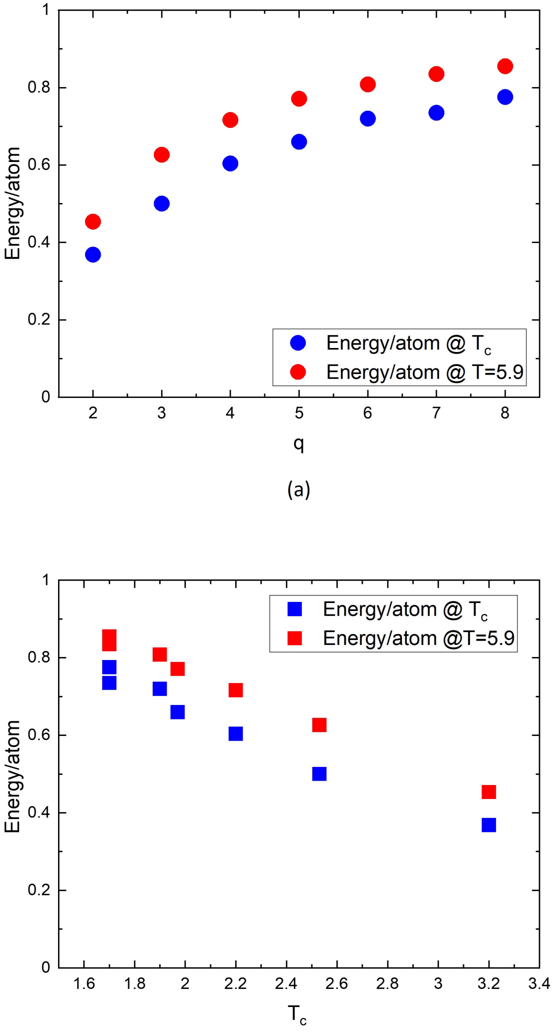

(a)

(b)

Figure 2.3.10: Energy/atom of a disordered state at the transition temperature and $T = 5.9$ as a function of (a) q states and (b) transition temperature (T_C).

not considered.

2.3.3 Order-disorder transition in different crystallographic systems

Although we can say that the thermodynamic principles of entropy and its effect remain the same for all systems, the coordination number of the system can have an effect on the critical temperature of transition.

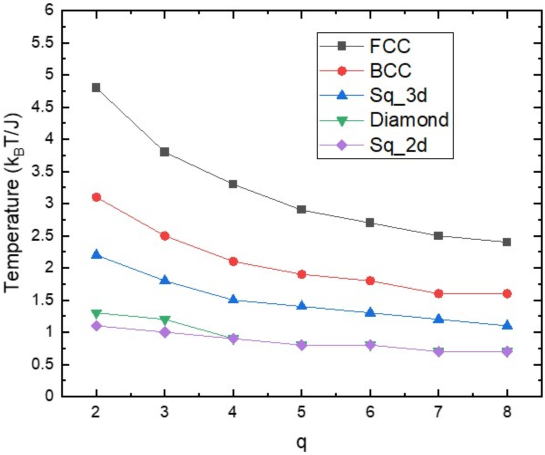

Figure 2.3.11: The critical transition temperature for q states 2 to 8 for various crystallographic lattices: FCC, BCC, Diamond, 2-dimensional Square (Sq_2d) and 3-dimensional square (Sq_3d) lattice

Figure 2.3.11 shows, despite the crystal structure, that the configurational entropy reduces the transition temperature; however, figure 2.3.12 shows that the lower the coordination number of the system, the lower the transition temperature. This can be explained by the fact that a lower coordination number suggests less number of nearest neighbour positions, and thus a higher probability of occupancy and less complicated and similar atom. This allows for a more easy random distribution of elements for crystallographic systems with lower coordination numbers. Therefore, diamond with $Z = 4$ has the lowest T_C for all the q states, and FCC with $Z = 12$ has the highest T_C for all the q states. As tabulated in table 2.3.2, T_C for q state 8 is half of the T_C of q state 2 for all crystallographic systems.

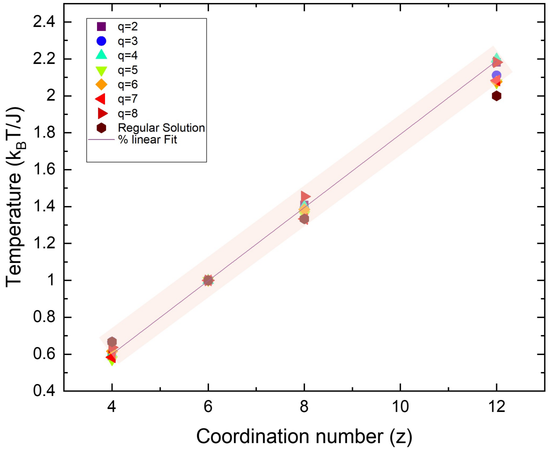

Figure 2.3.12: The transition temperature as a function of coordination number of the crystal systems normalized over calculations done on simple cubic on varying q state. The transition temperature and the coordination numbers show a linear relation for all the q states.

It can thus be concluded that without the interference of the bond energy and the enthalpy of mixing, entropy itself can be defined as a reason to obtain a stable random solid solution at low temperature. According to thermodynamics, a lower coordination number is preferred to obtain a stable random solid solution at a lower temperature.

Most transition metals in the periodic table are BCC or

q \ Z	**2 (Diamond)**	**6 (Square)**	**8 (BCC)**	**12 (FCC)**
2	1.3	2.2	3.1	4.8
3	1.2	1.8	2.5	3.8
4	0.9	1.5	2.1	3.3
5	0.8	1.4	1.9	2.9
6	0.8	1.3	1.8	2.7
7	0.7	1.2	1.6	2.5
8	0.7	1.1	1.6	2.4

Table 2.3.2: The order-disorder transition temperature (T_c) of various 3-dimensional crystal systems for q states 2 to 8.

FCC in the crystal structure. If an alloy of any number of constituents is made up of only FCC elements, the resultant alloy will be FCC in nature, and if all the constituent elements of the alloy are BCC in the crystal structure, the resultant alloy is also BCC. However, especially in multi-element systems, Kube et al. [115] reported that the BCC structure is preferred over the FCC structure because of the large atomic size difference. Thus elements in high-entropy alloys or multi-principal element alloys that would have preferred the FCC crystal structure prefer the BCC structure. This is additionally supported by the order-disorder transition based on the coordination number. As the coordination number of BCC is lower than that of FCC, this makes BCC a more constrain-free system. Therefore, BCC not only sustains the strain energy due to the atomic size difference but also increases the probability of obtaining a random disordered solid solution at a lower temperature than high coordination-numbered FCC.

The understanding of the order-disorder transition in detail as a function of the number of varying elements in the system, i.e. the q state, is focused on the BCC crystal system only.

2.3.4 Interactive energy, phase diagram and order-disorder transition

The other way to understand an order-disorder transition is by constructing a phase diagram that distinctly separates the ordered phase from a disordered phase. A general phase diagram shows the change in phase with the temperature and the constituent of the alloys. The diagram becomes complicated with increasing elements in the system if each axis represents an element. This phase diagram is constructed with the assumption that at $T = 6$ all the systems of different q states are completely disordered. In a completely disordered state, all the atoms at every site have different nearest-neighbour atoms. Since the interactive energy (E_T) of the dissimilar atoms (ϵ_{ij}) is 1 and that between similar atoms (ϵ_{ii} or ϵ_{jj}) is 0, energy at each temperature is the sum of a total number of dissimilar atomic neighbours or dissimilar bonds. As at $T = 6$, the system is considered to be the most random and disordered system, then the energy at $T = 6$ (E_{6kT}) is equivalent to the total number of dissimilar bonds the system can have. Thus, the fraction of dissimilar bonds (C_{ij}) for each temperature can be calculated as:

$$C_{ij} = \frac{E_T}{E_{6kT}} \tag{2.3.3}$$

As the system is made up of both similar and dissimilar bonds, the fraction of dissimilar bonds for every temperature is the following.

$$C_{ii} = 1 - C_{ij} \tag{2.3.4}$$

The phase diagram is constructed for the fraction of similar and dissimilar bonds for the given temperature range as shown in figure 2.3.13. The region above the bond line at higher temperatures is the disorder region, and the region below the bond line is the ordered region.

The transition point for $q = 2$ is where the bond line of similar and dissimilar bonds intersect, it coincides with the presence of 50% dissimilar bonds in the system. A similar transition can be observed for $q = 3$. However, from $q = 4$ onwards the transition is not sharp, but a plateau is at a particular temperature above which the concentration of the dissimilar bond fraction increases. This plateau corresponds to T_C. The transition temperature thus obtained from the phase diagram is listed in table 2.3.1.

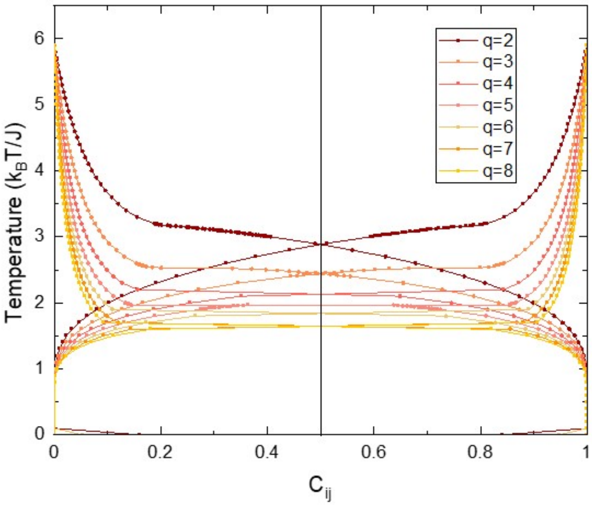

Figure 2.3.13: Phase diagram constructed for BCC q states 2 to 8 over temperature and the fraction of dissimilar atom interaction (C_{ij}). The total fraction of dissimilar (C_{ij}) and similar (C_{ii}) atom interaction at every temperature is 1. The line colour becomes lighter as the q state increases, indicating an increase in the plateau at the transition temperature.

Two elements alloy system (q state 2) As Morral and Chen [81] reported that in a regular solution model for a binary system the phase diagram as a function of temperature and composition, it shows a singular point on the graph representing the miscibility point and the spinoidal point at an equiatomic composition. A parallel can be drawn to this phase diagram constructed as a function of temperature and bond fraction. Since the number of elements in the system is two and the Glauber dynamics of the algorithm do not allow preserving the number of elements in the system, a 50% dissimilar bond suggests an equiatomic fraction of the two species. Thus, the transition is noted in the equiatomic composition. As the transition is smooth and does not show a plateau, no spinoidal decomposition at the transition point is observed. This abides by the regular solution thermodynamic results [81]. The smooth transition is further confirmed by figure 2.3.15 which shows the 2D XZ plane and the 3D BCC cubic lattice as observed by Ovito at $T = 2.9$, 3.0, 3.05, and 3.1. The lattice construction of the bond patterns is the colour map shown in the figure. The histogram as well as the colour distribution in the lattice shows a similar gradient at the temperature of transition, before and after it also. Beyond the transition temperature (T_C) as identified the fraction of dissimilar bonds increases but marginally.

Five elements alloy system (q state 5) The isopleth cross section for a quinary equiatomic system shows the spinoidal point is lower than the miscibility point that marks the transition from a single-phase random solid solution to an ordered phase [81]. This large gap between the miscibility point and the spinoidal point can be compared to the plateau obtained at the T_C in the phase diagram as a function of temperature and bond fraction. It can be suggested that the plateau indicates the miscibility gap resulting from the entropy of mixing and configuration. The plateau length increases with the q states as does the miscibility gap with increasing components in the system. The lattice reconstruction in figures 2.3.16 and 2.3.17 shows that at the $T_C = 1.96$, the plateau equivalent amount of similar and dissimilar bonds are present which is supported by the histogram. At that temperature higher than T_C ($T = 1.97, T = 2$) the lattice reconstruction specifically shows the presence of dissimilar bonds indicating a highly disordered state. Whereas, the temperature below the T_C ($T = 1.9$), the lattice reconstruction explicitly shows the imminence of similar bonds that is a highly ordered state (figure 2.3.16). A more detailed analysis shows the sharp change seen at $T = 1.966$ and $T = 1.977$ (figure 2.3.17) as $T = 1.966$ is the plateau isotherm, thus we can conclude the transition temperature as derived from the phase diagram is $T = 1.966$.

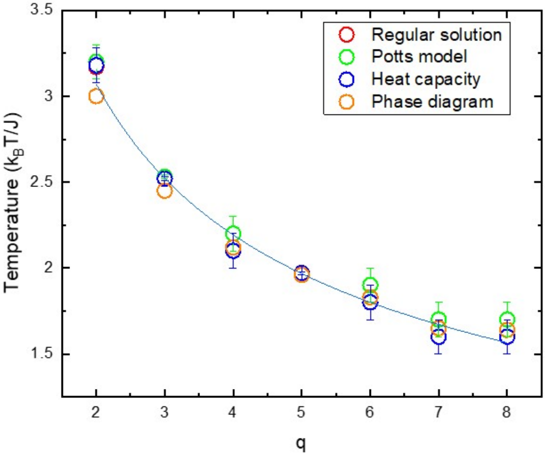

Figure 2.3.14: The transition temperature for different q states obtained using different methods of calculation:regular solution model, energy transition or Potts model, heat capacity variation meaning first order transition of energy and phase diagram from interactive energy transition reveals similar trend.

The plateau for higher-order q states suggests that at the transition temperature the probability of ordering is as high as disordering in the system. This is aided by the increase in the number of components in the system. As the component increases, the probability of pairing itself with another species also increases. Considering whether the probable formation is ordered or disordered, a range of energy can be possible at T_C which is indicated as the vertical line at the transition temperature in figure 2.3.13. This conclusion is comparable to the spinoidal gap observed in multi-elemental systems [81]. At spinoidal temperature, for a given composition of the alloy, an order-disorder phase transition can be observed at a temperature lower than the miscibility point. The added component in the alloy lowers this temperature further. This is in terms of the conclusion drawn from the figures 2.3.4, 2.3.9 and 2.3.13 where the increased q state lowers the temperature of the transition and the primary reason is the entropy of the system. In addition, a first-order transition aids in the spinoidal transformation.

Figure 2.3.14 clearly shows the (T_c) calculated by different methods for the range of states q. It can be seen that, except for q state 5, the results are underestimated for the other q states. This is because the temperature interval for data processing is in every $\Delta T = 0.01$, which for others is $\Delta T = 0.1$. As mentioned earlier a similar temperature difference is considered for $q = 2$. However, the lack of first-order transition in $q = 2$ therefore does not support a consistent result. The results cannot be further compared to order-disorder transition temperatures of alloys because the effect of enthalpy is overlooked here.

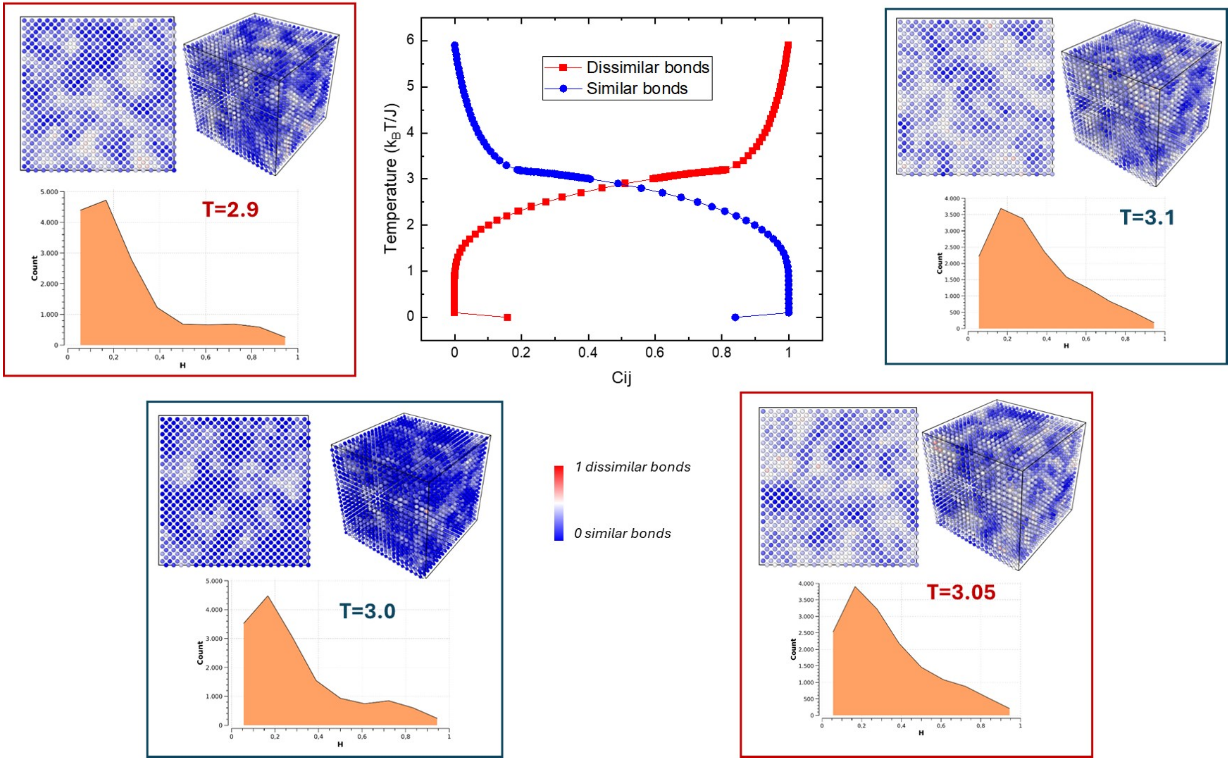

Figure 2.3.15: BCC binary ($q = 2$) lattice phase diagram showing the change of similar and dissimilar bonds for $T = 2.9, 3.0, 3.05$ and 3.1. The similar bond decreases beyond $T = 3.0$, suggesting that $T = 3.0$ is the order-disorder transition temperature for $q = 2$ determined by this method.

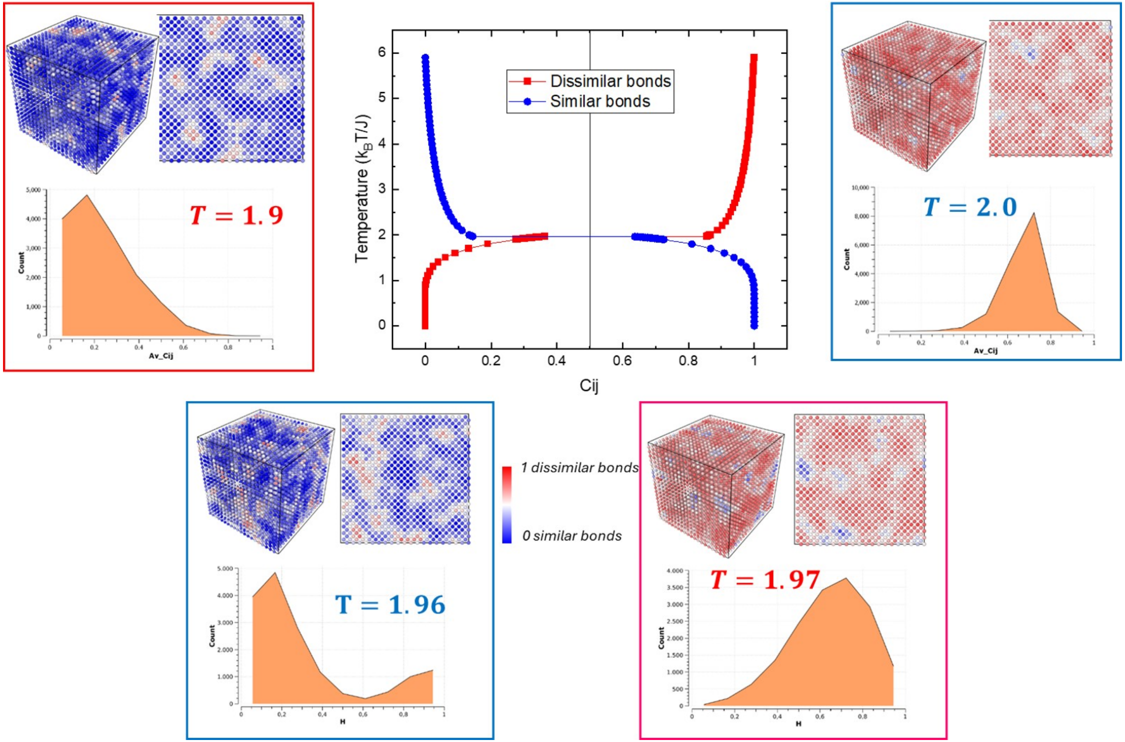

Figure 2.3.16: BCC quinary ($q = 5$) lattice phase diagram showing the change of similar and dissimilar bonds for $T = 1.9, 1.96, 1.97$ and 2.0. The dissimilar bond increases beyond $T = 1.96$, suggesting that $T = 1.96$ is the order-disorder transition temperature for q state 5 determined by this method.

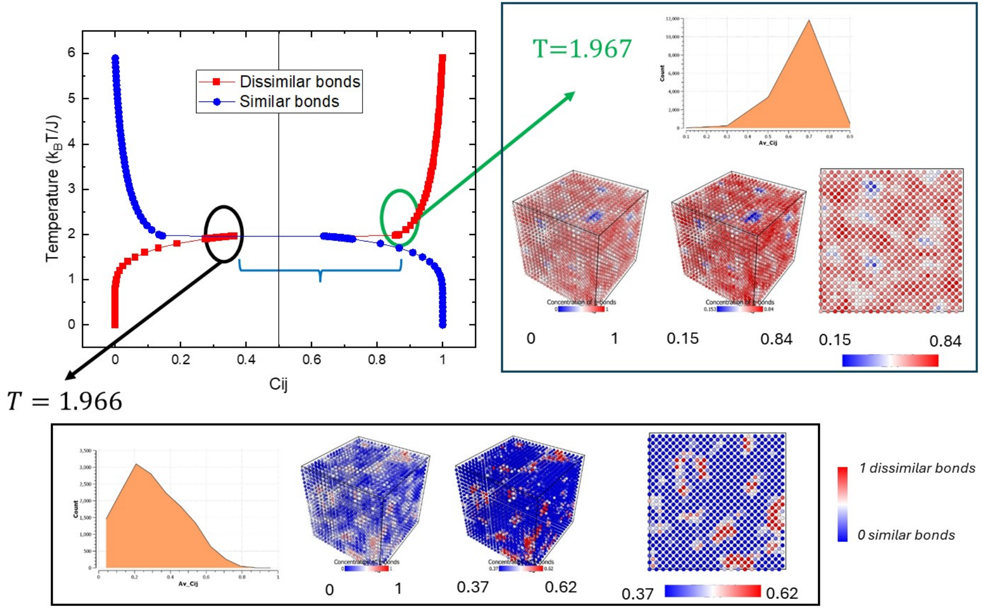

Figure 2.3.17: A detailed observation of the similar and dissimilar bonds of BCC $q = 5$ state at $T = 1.966$ and $T = 1.967$. The system shows more similar bonds in $T = 1.966$ than in $T = 1.967$. When observed in the narrow range of the phase line, small disordered and ordered phases can be seen in $T = 1.966$ and $T = 1.967$ respectively

2.4 Conclusion

This work extends the use of Monte Carlo simulation to understand the effect of the number of components on the order-disorder transition in multi-principal element alloys using the Potts model. This model is a simplistic attempt to understand the effect of the configurational entropy on the order-disorder transition of a crystal system. Although most of the work is concentrated on the BCC crystal structure, the phase transition is also observed for the three-dimensional crystal structure of various coordination numbers. It can be concluded that the lower coordination number aids in a stable disordered state at a lower temperature. This proves that BCC reaches a disordered state at a lower temperature than FCC and that the phase transition becomes more stable at lower temperature with increasing elements in the system and a lower coordination number. The configurational entropy, given by the number of elements in the system or the q states, lowers the temperature of the order-disorder transition. The determination of the phase transition and the transition temperature is obtained using three different methods in this work. The methods being: the regular solution method, the calculation of the change in energy per atom in the system, and interactive energy calculation to obtain a phase diagram.

The increase in elements in the system increases the energy of the disordered system. This energy is primarily contributed by the configuration and probability of having the same atoms or dissimilar atoms at neighbouring sites because of entropy. Without the effect of enthalpy, entropy can increase the energy of the system while lowering the transition temperature. The order-disorder transition for various q states is calculated using different methods. A similar result is obtained with an error of ±0.1 for all the q states. Therefore, it can be concluded that the entropy itself affects the order-disorder transition and the energy of the system. It is also observed, from the phase diagram formed from isopleth cross section of similar and dissimilar phases of various q states, that the gap between the spinoidal point and miscibility point increases with increasing q state. The increased miscibility gap or plateau at a temperature suggests that the order-disorder transition can be observed for a large fraction of dissimilar bonds in the system. It is not restricted to a state of the same number of similar and dissimilar bonds. Therefore, the order-.disorder transition temperature is stretched like a spinoidal transition.

All calculations are performed without including the atomic interaction based on their enthalpy. The additional effect of enthalpy can stabilise even systems with higher q states by lowering the energy of the disordered solid solution. However, that is beyond the scope of this work and leaves a path for further improvement on the simulation for a more comprehensive study of the effects of individual thermodynamic factors on a multi-principal element solid solution.

Chapter 3

Mechanical stability of BCC MPEAs

"The main purpose of science is simplicity and as we understand more things, everything is becoming simpler"

Edward Teller

3.1 Nanoindentation and mechanical properties

The primary mechanical properties obtained from the nanoindentation are hardness and elastic modulus. Hardness (H) is the response to stress of the material in the indentation at a given load (P) over a contact area (A) of the indentation on the material (equation 3.1.1).

$$H = \frac{P}{A} \tag{3.1.1}$$

The total displacement of the indenter from the point of contact with the surface of the material is given as h and $A = f(h_c)$ [116]. Indentation can be performed with different indentation geometry such as Vickers, Berkovich, and wedge-shaped. The contact depth of an indentation (h_c) is a function of the geometry of the indenter and the total displacement (h). The geometry of the indenter tip, along with the stiffness of the contact (S) determines the contact depth: $h_c = h - \beta P/S$. β is a constant, which is 0.75 for the Berkovich indenter.

Under plastic deformation, P and h are not absolute values. The stiffness (S) is the elastic stiffness of the contact, which is mathematically given as the slope of the unloading section of the load on the sample (P) vs the displacement into the sample (h) curve (equation 3.1.2). The stiffness is a response of the sample under investigation and the indentation device.

$$S = \frac{\mathrm{d}P}{\mathrm{d}h} = \frac{2}{\sqrt{\pi}}\sqrt{A}E_r \tag{3.1.2}$$

where E_r is the reduced modulus. The reduced elastic modulus E_r accounts for the deformation of the indenter i, as well as the sample s is calculated as

$$\frac{1}{E_r} = \frac{(1-\nu_i^2)}{E_i} + \frac{(1-\nu_s^2)}{E_s} \tag{3.1.3}$$

Here, ν and E represent Poisson's ratio and elastic modulus, respectively. The elastic modulus of a material is constant but varies with temperature. It can be obtained from nanoindentation experiments, assuming that ν (of the respective material) is known.

However, the hardness of the metal is not only a material property but also a function of the depth of indentation, crystallographic anisotropy, and temperature. The change in hardness with the depth of the indentation is known as the indentation size effect [117]. The hardness is observed to increase as the depth of indentation decreases. The hardness is the response of the statistically stored dislocation (SSD) and geometrically necessary dislocations (GND). SSDs result from homogeneous strain and are a function of the material itself, whereas GNDs are a response to strain to maintain the material continuity. The GNDs increase with the flow stress and are proportional to the plastic strain gradient. The strain gradient reduces with the depth of indentation. Therefore, at low indentation depths, the density of GND is high.

As the indentation depth increases, the plastic strain gradient decreases and the GNDs are distributed over a larger area. This reduces the hardness response of the material as the depth of indentation increases, also known as the indentation size effect (ISE). Nix-Gao model [118] is a mathematical approach to ISE expressed as in the following equation.

$$\frac{H}{H_0} = \sqrt{1 + \frac{h^*}{h}} \tag{3.1.4}$$

Here, H_0 represents the hardness at a large indentation depth or intrinsic hardness and h^* is the characteristic depth which is a function of the shear modulus and the shape of the indentation [118]. Equation 3.1.4 is based on the assumption that, after indentation, the GNDs concentrate in a hemispherical volume underneath a conical indenter tip.

The change in hardness over the depth of indentation reveals the difference in geometrically necessary dislocations and stress hardening in the system. The fluctuation in hardness in randomly distributed indentations in a given sample indicates the anisotropy of the system.

The fluctuation in hardness over different indents is useful for identifying precipitates or the presence of different phases in a sample. In order to obtain an average material property, it is usually preferred to obtain statistically viable data from indents spread over a large area. It is known to result in a highly stressed area below the indentation as a result of the formation and accumulation of GNDs. This is a plastically deformed high-stress zone, and having indentations close to one another can result in overlapping of the stress regions. That results in an overestimation of the hardness of the material. Therefore, it is advisable to keep the distance between indents three times the depth of the indentation [119, 120].

Hardness is also a function of temperature, especially for materials that are thermally sensitive, such as materials with a BCC crystal system. With an increase in temperature, the strain hardening decreases, and thus reduces the hardness response of the material. Nanoindentation can also be performed at higher temperatures by heating the stage and the samples simultaneously. Sapphire is the material of choice as a nanoindentation tip as a result of its heat-resistant response at elevated temperature. This helps in observing the stress response of the material at elevated temperatures. Nanoindentation is a versatile mechanical testing method that does not require extensive sample preparation methods. This makes nanoindentation an alluring method for easily estimating the strength of a material, as well as to use its statistical methods of acquiring data to extend the understanding of the plastic response of the material under strain caused by indentation.

It can be observed in some materials that there is a tendency for material to ‘pile-up’ around the indentation site. This results in a change in contact depth, and thus results in higher calculated hardness and elastic modulus. This is usually observed for materials with low work hardening or low strain. This can also be seen for thin soft films on a hard substrate. Therefore, indents are usually observed optically to identify and measure if any significant ‘pile-up’ occurs. The accurate hardness and elastic modulus is then calculated using the corrected area function. The corrected area function is determined by the correction factor, i.e. the ratio of the contact area projected on the indentation to the geometrical cross-sectional area of the indenter. Without the ‘pile-up’, the correction factor is not a function of the depth of indentation and thus has no effect on determining the mechanical properties [121].

3.1.1 Determining dislocation nucleation by nanoindentation

Schuh et al. [122] developed a method to statistically quantify the activation volume for the nucleation of dislocations experimentally using nanoindentation and, in turn, the activation energy required for the nucleation of dislocation. Nanoindentation can be designed to indent to a very low depth of 50 to 100 nm on a presumably defect-free small sample for 100 to 150 nm using a low load that initiates dislocation nucleation under the indent [123].

When a sample is carefully polished, a dislocation-free region can be obtained on the surface. During indentation, the stress below the indenter gradually increases to be equal to the maximum resolved shear stress of the material. Slip is initiated at this stress, but in a dislocation-free region, dislocation nucleates at this stress to allow plasticity

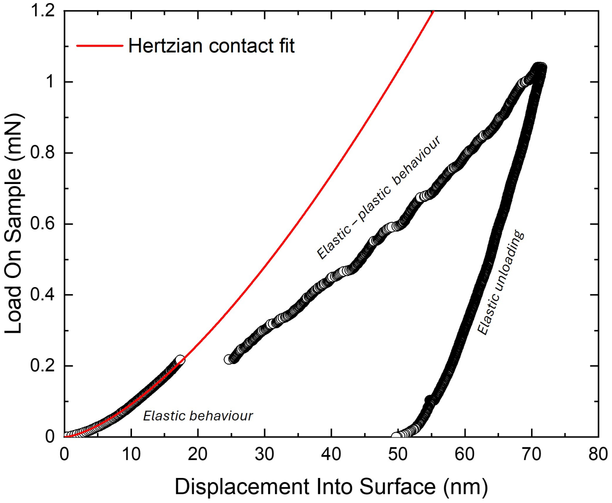

Figure 3.1.1: A typical representation of load on sample vs displacement into the surface for a pop-in experiment that shows the Hertzian contact fit [124] just before the pop-in.

to set in. The nucleation of dislocations can be identified as a plateau in the load on the sample vs. displacement graph. This plateau is called a "pop-in" (figure 3.1.1). The nucleation is assisted by the stress generated during the indentation. For metals or alloys that show no stress-induced phase transformation, the pop-in in the load-displacement curve is expected to be the result of stress-assisted nucleation of the dislocation during the elastic to plastic transition under stress [122, 123, 125].

A pop-in indicates a vacancy or defect that results in a large change in displacement on the surface under the given load on the sample [122]. This phenomenon is considered the nucleation of a defect and the defect generated is a new dislocation in a dislocation-free environment. A series of indents is required to increase the probability of generating new dislocations. The rate of nucleation of dislocations $\dot{N}$ can be expressed as a function of the intrinsic energy barrier for the formation of dislocations ξ, shear stress τ and temperature:

$$\dot{N} = \dot{N}_o \exp[-(\xi - \tau V_n^*)/kT] \tag{3.1.5}$$

where V_n^* is the activation volume involved in nucleation and $\dot{N}_o$ is the pre-exponential attempt frequency factor per unit volume. When the rate of nucleation is integrated over the entire indented volume, the equation can be rewritten as

$$\dot{N} = \dot{N}_o \exp(\frac{E}{kT}) \int_V [\exp(\frac{\tau V_n^*}{kT}) \, \mathrm{d}V] \tag{3.1.6}$$

The probability of the rate of nucleation of the dislocations in the volume of indentation can be statistically expanded over the rate of cumulative distribution frequency (CDF (f)) of pop-ins that occur.

$$f(t) = 1 - \exp(\int_0^t \dot{N}(t) \, \mathrm{d}t) \tag{3.1.7}$$

For a given load rate and the corresponding shear stress, the CDF (f) can be rewritten as

$$f(\tau) = 1 - \exp(\int_0^t \dot{N}(\tau) \, \mathrm{d}\tau) \tag{3.1.8}$$

The equation mentioned above indicates the statistical correlation of the shear stress under indentation with the nucleation of the dislocation.

The above equation can be expressed similarly to the Weibull distribution [126]. This brings a comparison to the weakest link approach for brittle materials as discussed in A.2.

Using statistical distribution and correlation, the cumulative fraction of pop-ins (f) in the correlation of shear stress (τ) from equation 3.1.8 can be written as

$$\ln|-\ln|1-f||=\frac{V_n^*\tau}{kT}+\kappa \tag{3.1.9}$$

where κ is a parameter that has a weak dependence on τ. @ Equation 3.1.9 provides a linear relation to determine the activation volume V^*. The activation volume V^*, here defined as the critical volume occupied by a linear defect to activate nucleation of a dislocation for the onset of plastic deformation from the elastic equilibrium state.

3.1.2 Characterizing dislocation motion by nanoindentation

Plastic deformation and flow stress are influenced by the change in applied strain. The change in strain rate correlates the dislocation interactions with the plastic deformation under an externally applied force. The response to the change in the strain rate is given as the strain rate sensitivity [49].

The strain rate sensitivity (m) is a function of the flow stress (σ) and the strain rate ($\dot{\varepsilon}$) at a constant temperature (T) and strain (ε). It is well established that as the strain rate increases, the flow stress increases based on the equation.

$$\sigma=C\dot{\varepsilon}^m \tag{3.1.10}$$

The slope of the logarithmic representation of σ vs $\dot{\varepsilon}$ gives the strain rate sensitivity (m) (equation 3.1.10). From the tensile tests [49], it is noted that the metals have $m<0.1$ at room temperature. As the strain rate sensitivity increases, the elongation and hence, the ductility increases. Higher strain rate sensitivity is observed in Newtonian viscous solid or superplastic alloys where strain rate hardening suppresses the necking in these alloys [127–129].

$$m = \frac{\mathrm{d}\ln|\sigma|}{\mathrm{d}\ln|\dot{\varepsilon}|} \tag{3.1.11}$$

As the strain rate changes, the flow stress is modified, which is governed by the density of dislocations and their interaction and velocity. The strain rate is related to the velocity of the dislocations (w) and the density of the dislocations (ρ) as:

$$\dot{\varepsilon} = \rho b w \tag{3.1.12}$$

$$w = A\sigma^{m'} \tag{3.1.13}$$

$$m'_V = \frac{1}{m} - \frac{\mathrm{d}\ln|\rho|}{\mathrm{d}\ln|\sigma|} \tag{3.1.14}$$

The above equations are based on uniaxial loading. A is a constant and m' and m'_V are variables related to the strain rate.

This work was further expanded in the context of nanoindentation, where strain rate sensitivity was observed under nanoscale plastic deformation and calculated using nanoindentation [130–133]. Different methods of experiments were used among which Mayo and Nix [134–136] used the constant loading rate method, which reduced the equation 3.1.11 to:

$$m = \frac{\mathrm{d}\ln|\sigma|}{\mathrm{d}\ln|\dot{\varepsilon}|} = \frac{\mathrm{d}\ln|H/C|}{\mathrm{d}\ln|\dot{\varepsilon}|} \tag{3.1.15}$$

The flow stress is written as a function of hardness where the flow stress $(\sigma) = H/C$, where $C = 3$ is the constraint Tabor factor which is a material function of elastic-plastic deformation [137, 138]. The strain rate obtained from the indentation is derived from the true strain and assumes that the hardness is constant over a particular range of depth of indentation. This results in equation 3.1.16 where $\dot{\varepsilon}$ is a function of change in load rate for a load controlled system [139].

$$\dot{\varepsilon} = \frac{\dot{h}}{h} = \frac{1}{2}\left(\frac{\dot{P}}{P}\right) \tag{3.1.16}$$

Since the strain rate sensitivity involves the dislocation velocity (w) and the dislocation density (ρ), the volume (V_m^*) involved in the motion of these dislocations can also be calculated.

The strain rate sensitivity is related to the activation volume as

$$m = \sqrt{3}\frac{kT}{V_m^*} \tag{3.1.17}$$

The above equation (3.1.17) holds for the local multiaxial loading as derived by Wei [140]. The standard activation volume under uniaxial loading is calculated in a similar way by Gibbs [141]. The activation volume of the plastic deformation is the critical volume that a dislocation needs to occupy to facilitate movement. Thus, the activation volume is directly related to the deformation mechanism of the system [142].

In this work (Section 1.3.3,) it has been previously reported that hardness is a function of the depth of indentation for most elements and alloys. This infers that equations 3.1.15 and 3.1.17 also depend on the depth of indentation. Maier et al. [143] suggested an advanced protocol of the strain rate jump test by nanoindentation focussing on the indentation under the same microstructure where the strain rate changes with depth during an indentation protocol. However, in this work, the experiments are focused on using four different constant strain rates. The load responses are identified for a given depth of indentation for every strain rate. This is in order to take into account the effect of indentation depth on hardness.

3.2 Experimental Details

This section lists the materials for experimentation and observation in order to understand dislocation nucleation, dislocation motion, and plasticity of BCC refractory MPEAs. The experimental setups that involve nanoindentation to answer these questions are also described in detail.

3.2.1 Materials

The samples studied are BCC refractory MPEAs namely TiNbHfZrTa and NbMoCrTiAl and their quaternary derivatives NbMoTiAl and MoCrTiAl. Chen et al. [22] have already reported that NbMoCrTiAl and its derivatives NbMoTiAl and MoCrTiAl have a B2 ordered structure. The samples were cast and homogenised at 1300 ° C for 20 hours for NbMoCrTiAl and its derivatives and at 1150 ° C for 48 hours for TiNbHfZrTa. They were provided by the Institut für Angewandte Materialien – Werkstoffkunde (IAM-WK) (Karlsruher Institut für Technologie (KIT)). The specimens for the nanoindentation were metallographically grinded using SiC grinding paper from 300 to 2500 grit papers and then cleaned with ethanol. Then they were mechanically polished with 3μm and 1μm grain size diamond suspension and oxide polishing suspension (OPS) and finally vibro-polished for 16 hours to obtain a stress-free flat mirror-like surface finish. The meticulous preparation of the samples was performed by researchers at IAM-WK, Karlsruher Institut für Technologie (KIT)). The Poisson ratios (ν) for NbMoCrTiAl and its derivatives are calculated from the reported data [23] and that of TiNbHfZrTa was calculated as 0.38 [21].

3.2.2 Nanoindentation

Nanoindentation experiments were performed using a Nano Indenter ® G200 Nanoindenter (Agilent / Keysight Technologies, Inc. California, USA, presently KLA Corporation, California, USA) with diamond Berkovich indenter tips at room temperature and sapphire Berkovich indenter tips for higher temperatures. A Berkovich indenter tip is a three-sided pyramid. A diamond indenter has E of 1141 GPa and ν of 0.07. The E of the sapphire indenter is 420 GPa at room temperature. The ν for sapphire is 0.24. All the nanoindentations were performed after the thermal drift was reduced to $0.05\,\mathrm{nms^{-1}}$.

The hardness, elastic modulus, and theoretical shear stress were calculated by loading the samples in the XP load module and Dynamic Contact Module (DCM). The XP load module has a lower resolution but a higher load-exerting capability with a maximum load applying limit of 500 mN. The DCM on the other hand, has an improved resolution with maximum load applying capability of 30 mN only. The unloading stiffness is determined using the Oliver-Pharr method [116]. However, contact stiffness can also be determined using the Continuous Stiffness Measurement (CSM) method during dynamic loading. The stiffness is determined during loading using an additional oscillation, thus allowing multiple loading and unloading segments during a single loading measurement. This allows for dynamic determination of the unloading stiffness and, subsequently, of the hardness and modulus. The unloading stiffness is measured at 10% of the maximum load. [116]

3.2.3 Indentation at room temperatures

The samples were loaded up to 2000 nm depth from the surface with a constant strain rate ($\frac{\dot{\mathrm{P}}}{\mathrm{P}}$) of $0.05\,\mathrm{s^{-1}}$ using the XP load module and 500 nm depth from the surface with a constant strain rate of $0.05\,\mathrm{s^{-1}}$ using the DCM load module. The strain rate $\dot{\varepsilon}$ is usually defined as an increase in the displacement rate $\dot{h}$ over the displacement h as given by the equation 3.1.17, therefore $\dot{\varepsilon}$ is given as $\frac{1}{2}\frac{\dot{P}}{P}$. The samples were tested in the continuous stiffness mode, which allows continuous recording of the stiffness and thus continuous recording of the elastic modulus and hardness over the depth of the indentation. The results were averaged over 15 indentations that were spaced at 60 μm from each other. In order to avoid the non-uniformity close to the surface and the fluctuation during unloading the mechanical properties are averaged over a depth of 1400 to 1600 nm and 200 to 400 nm for results from the XP load module and DCM load module indentations, respectively.

The indents of constant strain rate of $0.05\,\mathrm{s}^{-1}$ by the XP load module were investigated with UV laser scanning confocal microscope (LSCM) (Keyence Corporations, Osaka, Japan) to measure surface roughness and observe the presence of pile-up from indentation. Indent imprints were observed under the scanning electron microscope (SEM) (FEI Helios Nanolab™ 650, Thermo Fischer Scientific Inc., Massachusetts, USA).

3.2.4 Indentation at elevated temperatures

For elevated temperature experiments, a sapphire Berkovich tip was used with a laser heating stage (SURFACE systems + technology GmbH and Co. KG, Hückelhoven, Germany). The sample and tip were independently heated to reduce the thermal drift of the system. The E is a function of temperature as reported by Wachtman et al. [144] and the relevant data were used for a given temperature. Temperatures ranging from room temperature to 693 K at an interval of 100 K were used to observe the mechanical properties of the samples, subjecting them to $0.05\,\mathrm{s}^{-1}$ strain rate ($\frac{\dot{P}}{P}$) to a depth of 2000 nm using the XP head. Oliver and Pharr method [116, 145] was used to determine E and H from the data unloading. The tip area function and the subsequent stiffness of the system for a Berkovich indenter were calculated as described in the paper [116, 145].

3.2.5 Indentation conditions for determining dislocation nucleation

To understand the nucleation of the dislocation, the samples were subjected to constant load rates ($\dot{P}$) 0.01 $\mathrm{mNs^{-1}}$ and 0.005 $\mathrm{mNs^{-1}}$ indented with a blunt Berkovich indenter to a depth of 70 nm. A series of 100 to 120 indents with a spacing of 15 µm between indents were indented focussing on a single grain to avoid anisotropy of the samples. On careful and meticulous polishing, the first few layers are considered to be stress-free and defect-free, except for some intrinsic defects, making indentation below 100 nm ideal for understanding the nucleation of dislocations. That results in a discontinuity of displacement under the same load or pop-in [123].

It is assumed that the initial contact of a Berkovich tip is a spherical contact because of the tip rounding. The load-displacement curve before the first pop-in is considered completely elastic in nature, thus the spherical contact of the tip with the material allows application of the Hertz elastic contact theory [124]. This allows the load to be expressed as a function of displacement into the surface:

$$P = \frac{4}{3} E_r \sqrt{R} h^{2/3} \tag{3.2.1}$$

where E_r is the reduced elastic modulus as given by equation 3.1.3 and R is the radius of the indenter tip.

The maximum shear stress at the elastic-plastic transition, using the pop-in load and the initial displacement into the surface at that load, is determined as

$$\tau_{max} = 0.31 [\frac{6PE_r^2}{\pi^3 R^2}]^{\frac{1}{3}} \tag{3.2.2}$$

The calculation of the shear stress at the pop-in load is based on the underlying theory of stress-assisted and thermally activated dislocation nucleation. The theory suggests that during indentation, when the shear stress below the indent is as high as the theoretical shear stress of the material, the stress is sufficient to overcome the Peierls barrier and the plasticity in the material is initiated by homogeneous nucleation of dislocation in a defect-free volume [123, 146]. The alloys were subjected to two different load rates to study the effect of changing load rates. The change in load rate indicates the thermomechanical effect on dislocation nucleation.

3.2.6 Indentation conditions for determining strain rate sensitivity

To observe and calculate the strain rate sensitivity of NbMoCrTiAl, MoCrTiAl, NbMoTiAl and TiNbHfZrTa, the samples were subjected to constant strain rates ($\frac{\dot{h}}{h}$) of $0.1, 0.05, 0.01$ and $0.005\,\mathrm{s}^{-1}$ to a depth of 2000 nm using a Berkovich diamond indenter tip using CSM with XP load module at room temperature. A range of 10 indents with a spacing of 30 μm under each strain rate was performed on a single grain to avoid grain orientation anisotropy. The hardness and elastic modulus values were averaged over a depth of 1200 to 1500 nm. The strain rate sensitivity based on a variation of hardness was calculated over depths of 1000, 1200, 1400 and 1600 nm for the four strain rates and the strain rate sensitivity of the samples were also determined.

3.3 Results

This section reports the results obtained from nanoindentation. Firstly, it highlights the mechanical properties obtained from nanoindentation at room temperature, followed by those at higher temperatures. Secondly, this section reports the nanoindentation results for understanding dislocation nucleation and motion is also reported in details. Finally the results of experiment to determine strain rate sensitivity is also discussed in details.

3.3.1 Elastic modulus and hardness at room temperature

It can be noticed in figure 3.3.1a, 3.3.1b and 3.3.2a, the hardness of NbMoCrTiAl and its derivatives decreases with the depth of indentation unlike for TiNbHfZrTa (figure 3.3.2b). This hints at the indentation size effect commonly seen in BCC metals and alloys [130, 147]. So in order to compare the results of all the samples, the properties at the same depth are compared. The comparable values of the hardness are plotted as shown in figure 3.3.5a. The hardness reported from the DCM load module is higher than that of the XP module, confirming the indentation size effect. The hardness reported here is at room temperature. The hardness of TiNbHfZrTa is the lowest in the compared systems.

Hardness is a function of the structural characteristic of a material and thus can vary with the depth of indentation and grain orientation. However, the elastic modulus is a constant for a material at a given temperature and therefore does not change with the change in the depth of indentation, as can be seen in figures 3.3.3 and 3.3.4. However, the modulus can be a function of the crystal orientation. However, for these experiments, the indentations are tried to be within the same grain to rule out the effect of crystallographic orientation and anisotropy (figure 3.3.5a).

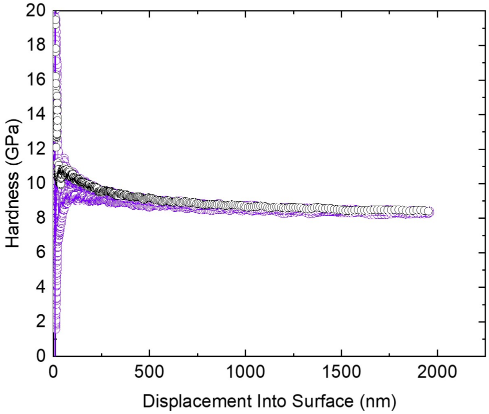

(a) NbMoCrTiAl

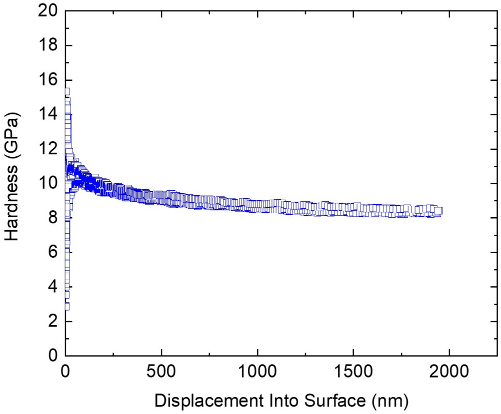

(b) MoCrTiAl

Figure 3.3.1: Hardness plotted over displacement into the sample for (a) NbMoCrTiAl, (b) MoCrTiAl. The hardness reduces over the depth of indentation for NbMoCrTiAl, MoCrTiAl showing the indentation size effect of NbMoCrTiAl and the family of alloys.

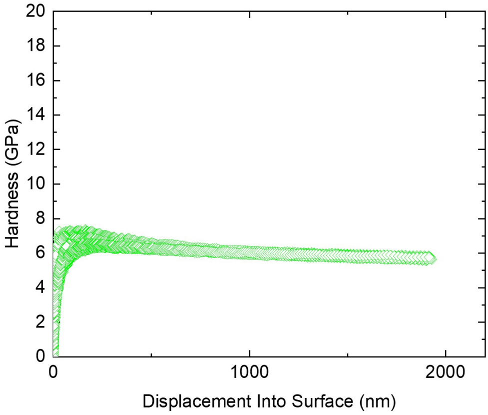

(a) NbMoTiAl

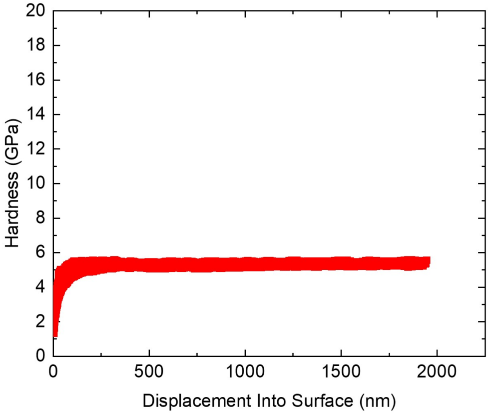

(b) TiNbHfZrTa

Figure 3.3.2: Hardness plotted over displacement into the sample for (a) NbMoTiAl and (b) TiNbHfZrTa. The hardness reduces over the depth of indentation for NbMoTiAl but it remains constant over depth of indentation for TiNbHfZrTa showing the indentation size effect of NbMoCrTiAl and the family of alloys.

Samples	**DCM module 250 to 400 nm (GPa)**	**XP module 1400 to 1600 nm (GPa)**
NbMoCrTiAl	9.58 ± 0.07	8.39 ± 0.09
MoCrTiAl	9.28 ± 0.14	8.25 ± 0.22
NbMoTiAl	7.28 ± 0.08	6.01 ± 0.11
TiNbHfZrTa	6.20 ± 0.04	5.79 ± 0.10

Table 3.3.1: Hardness MPEAs using DCM load module and XP load module that is averaged over a depth of 250 to 400 nm and 1400 to 1600 nm respectively.

Furthermore, as reported by Chen et al. [60] for microhardness, nanohardness reduces with the absence of Cr in the NbMoCrTiAl system. In addition, decreasing the content of Nb increases the modulus, as well as the hardness of the system. As seen from figure 3.3.1a the hardness value from nanohardness is higher than the macrohardness result reported by [60]. Due to the larger load of microhardness indentation compared to nanoindentation, the hardness response is affected by the effect of the indentation size (ISE), as explained in section 3.1. The result is also affected by the crystal orientation anisotropy, as it was mentioned that the nanoidentation was focused on a single grain, whereas the microhardness tends to be spread over various grains because of the larger size of the indents. The effect of anisotropy can also be observed for the elastic modulus reported by this work compared to that reported by Chen et al. [60] using microhardness. During macroindentation testing, the sample covers a larger area which may or may not include voids and porosities resulting from the thermomechanical processing. The presence of these voids and porosity can in turn affect the hardness and elastic modulus reported by microindentation.

Samples	**DCM module 250 to 400 nm (GPa)**	**XP module 1400 to 1600 nm (GPa)**	**Reported (GPa)**
NbMoCrTiAl	192.0 ± 0.7	196.7 ± 2.0	168.0 ± 1.0
MoCrTiAl	202.5 ± 2.7	203.8 ± 2.6	142.0 ± 2.2
NbMoTiAl	194.3 ± 1.8	196.2 ± 7.0	152.0 ± 0.5
TiNbHfZrTa	111.4 ± 0.5	112.0 ± 0.9	88.8 ± 2.0

Table 3.3.2: Elastic modulus of MPEAs using DCM and XP load module, and averaged over a depth of 250 to 400 nm and 1400 to 1600 nm respectively.

It should also be noted that the elastic modulus is lesser for TiNbHfZrTa than for the NbMoCrTiAl family. This indicates that compared to NbMoCrTiAl and its family of alloys, TiNbHfZrTa is less stiff and more formable. However, Young's modulus of TiNbHfZrTa is 20% lower than that reported by Laplanche [148] and similar to that reported by Dirras [149]. The texture and processing treatment of the material affect the modulus. Further nanoindentation experiments will help to elucidate this difference and its effect on the elastic and plastic deformation of the alloys.

The indents, when observed under SEM and LSCM, do not show material pile-up or sink-in around the indents for any of the four alloys. Figure 3.3.6 shows the indented profile using SEM and figure 3.3.7 and 3.3.8 shows surface roughness using LSCM for all samples in the investigation. The figure 3.3.6 highlights one indent of each material, indented to a depth of 2000 mm at $0.5\,\mathrm{s}^{-1}$ using the XP module. More than one indents were observed under the SEM for a better understanding. SEM microscopy images did not reveal cracks in the corners of the indents, suggesting local ductility despite the brittleness reported in macroscopic testing [23, 60]. Slip traces can be identified in different directions around indentation sites. This is

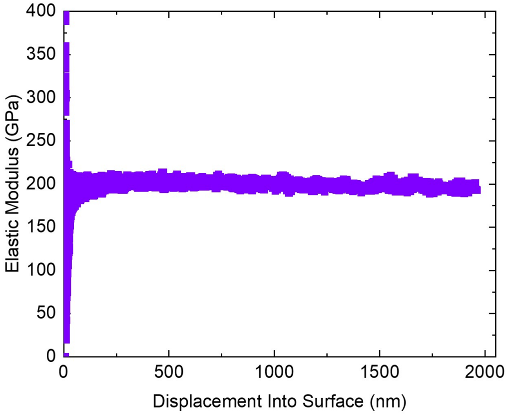

(a) NbMoCrTiAl

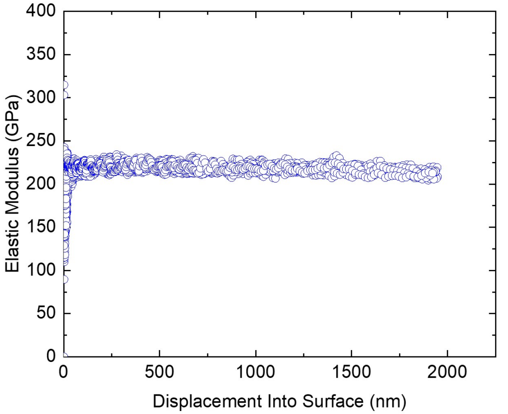

(b) MoCrTiAl

Figure 3.3.3: Elastic modulus plotted over displacement into the sample for (a) NbMoCrTiAl, (b) MoCrTiAl showing the variation of modulus over different indentations. The elastic modulus is a characteristic of material and thus remains constant over the depth of indentation.

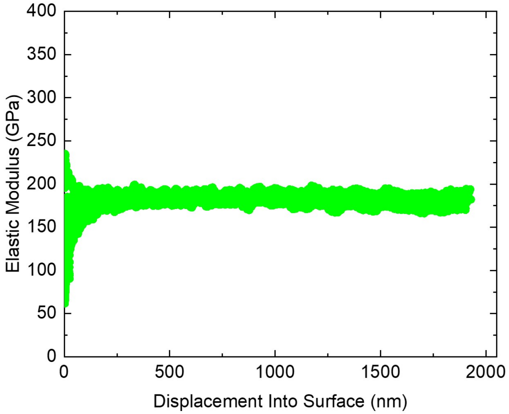

(a) NbMoTiAl

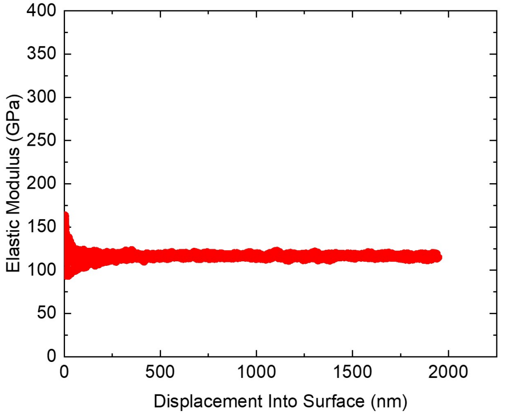

(b) TiNbHfZrTa

Figure 3.3.4: Elastic modulus plotted over displacement into the sample for (a) NbMoTiAl and (b) TiNbHfZrTa showing the variation of modulus over different indentations. The elastic modulus is a characteristic of material and thus remains constant over the depth of indentation.

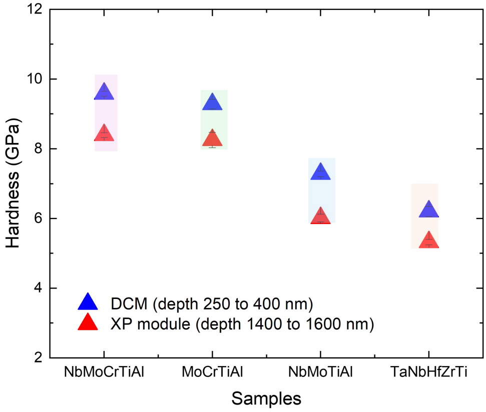

(a)

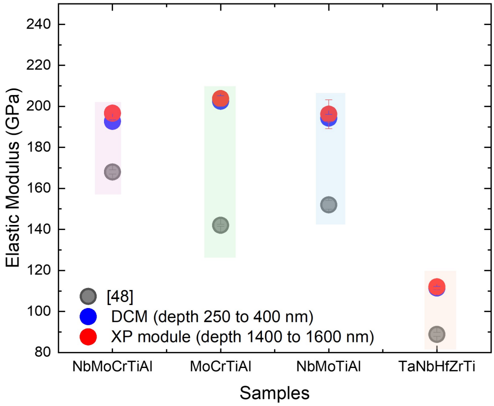

(b)

Figure 3.3.5: (a) Hardness and (b) modulus of elasticity of all the samples obtained at different depths of indentation and using different modes of indentation resolution.

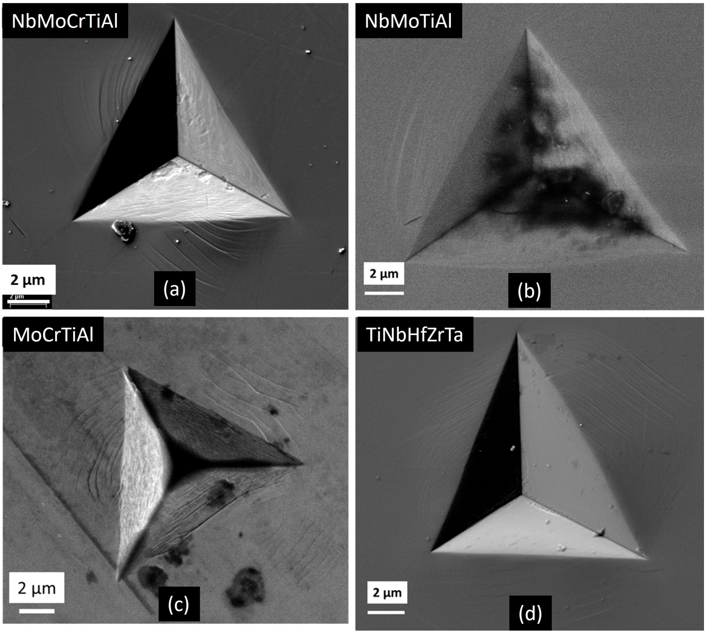

Figure 3.3.6: The indent profile using SEM shows no edge cracking for NbMoCrTiAl, NbMoTiAl, MoCrTiAl and TiNbHfZrTa. The slip line around the indents can be observed more specifically for (a) NbMoCrTiAl and (c) MoCrTiAl

similar to the slip traces observed by Chen et al. [60] under micro-indentation.

The slip traces are planar and sharp for MoCrTiAl, whereas they are planar and more rounded for NbMoCrTiAl and NbMoTiAl. It should be noted that slip traces were not distinctly observed for TiNbHfZrTa. The difference in slip traces between TiNbHfZrTa and the NbMoCrTiAl alloy family indicates the difference in the slip generation and deformation method of these systems. The surface roughness as observed in the figures 3.3.7 and 3.3.8 using the LSCM is less than 0.05 μm for all the samples in the investigation. LSCM uses laser to scan the material for surface

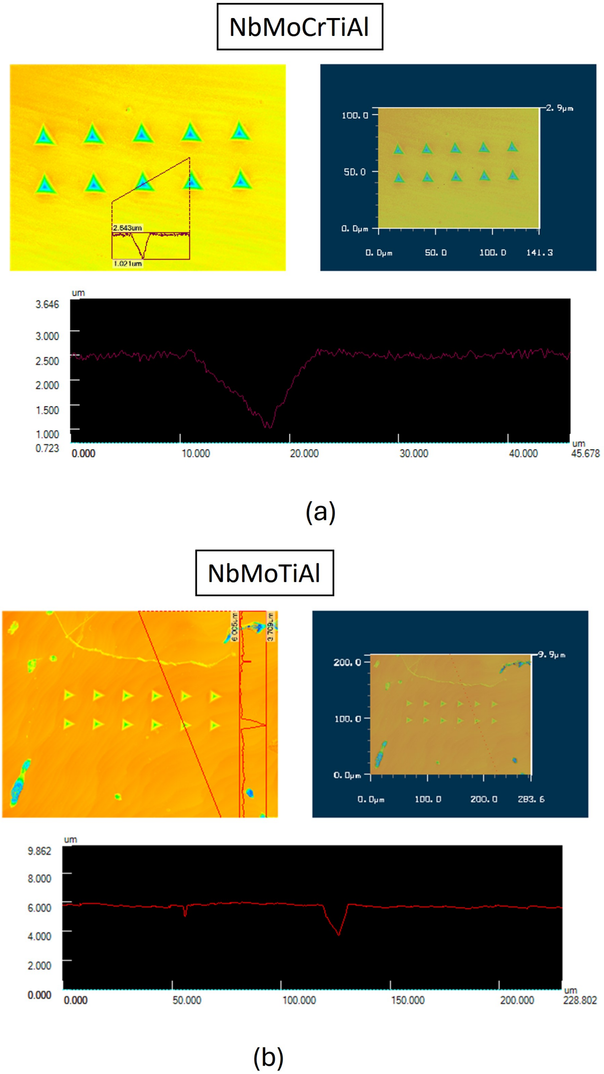

Figure 3.3.7: The indent profile surface roughness of less than 0.05 μm using LSCM for (a) NbMoCrTiAl and (b) NbMoTiAl.

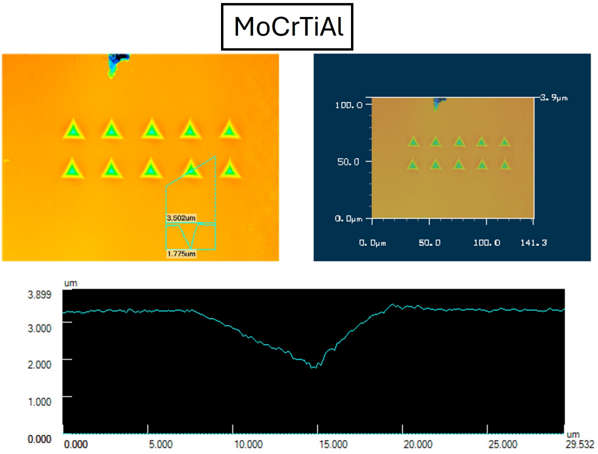

(c)

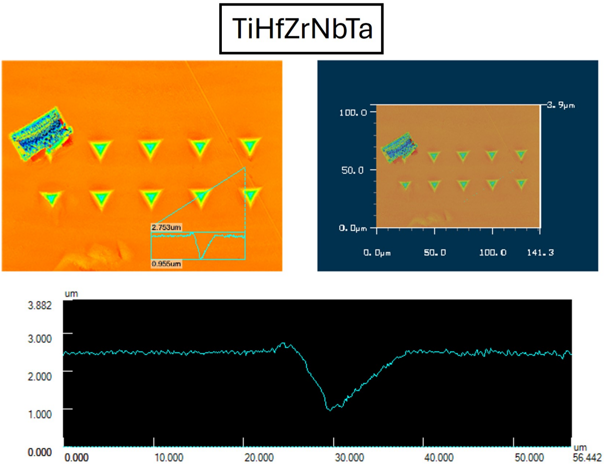

(d)

Figure 3.3.8: The indent profile surface roughness of less than 0.05 μm using LSCM for (a) MoCrTiAl and (b) TiNbHfZrTa.

roughness, and thus can scan the indents and identify the depth profile of the indents. The different colour profiles indicate that all the indents in the same material have the same depth of indentation and are uniform. A line scan as shown passing over one or two indents shows no pile-up or sink-in around the indents, as also observed by the SEM images.

Further mechanical properties can be calculated from the results obtained from the indentation. The maximum theoretical shear stress (τ_{th}) and the shear modulus (G) can be calculated from elastic modulus (E) and Poisson's ratio (ν). The maximum theoretical shear stress is the maximum stress required to allow slip, which gives a better understanding of the deformation mechanism of the materials. However, the slip occurs at the shear stress less than the maximum theoretical shear stress τ_{th} due to the presence of defects such as dislocations.

$$G = \frac{E}{1+\nu} \tag{3.3.1}$$

$$\tau_{th} = \frac{E}{2\pi(1+\nu)} \tag{3.3.2}$$

Table 3.3.3 lists the shear modulus and the maximum shear stress of the MPEAs at room temperature. It can be seen that the maximum shear stress for TiNbHfZrTa is less than that of NbMoCrTiAl and its derivatives. This supports the fact that a lower yield stress is reported for TiNbHfZrTa compared to the other MPEA system [14, 21]. This also hints at a different deformation mechanism for TiNbHfZrTa compared to NbMoCrTiAl and its family of alloys. The shear stress for NbMoCrTiAl and its family of alloys, owing to its variation in elastic modulus, follows a similar pattern. It increases with a decrease in the Nb content and increases with the increase in Cr.

Samples	**(250 to 400 nm)**		**(1400 to 1600 nm)**	
	G (GPa)	$\tau_{\mathbf{th}}$**(GPa)**	**G (GPa)**	$\tau_{\mathbf{th}}$**(GPa)**
NbMoCrTiAl	74.1 ± 0.7	11.8 ± 0.01	75.6 ± 1.0	12.0 ± 0.2
MoCrTiAl	77.9 ± 1.0	12.4 ± 0.2	78.4 ± 0.8	12.5 ± 0.1
NbMoTiAl	74.6 ± 1.8	11.8 ± 0.3	75.5 ± 2.7	12.0 ± 0.4
TiNbHfZrTa	42.8 ± 0.2	6.4 ± 0.1	40.5 ± 0.3	6.5 ± 0.1

Table 3.3.3: The shear modulus and theoretical shear stress calculated from the elastic modulus obtained from the experiments.

3.3.2 Mechanical properties at elevated temperature

The elastic modulus is a function of temperature, as it is dependent on the binding energy of the atoms. As the thermal excitation increases, the modulus of the system decreases. As seen in figures 3.3.9 and 3.3.10, the slope of the modulus decreases with temperature for NbMoCrTiAl and its derivatives. This is the usual trend seen in metals, alloys, high-entropy or medium-entropy systems of multi-principal element systems. The decrease in the elastic modulus with temperature is clear evidence of no magnetic or phase transformation for the given temperature range (Table 3.3.4).

This dependence can be further understood by fitting the empirical fit put forward by Varshni [150], where,

$$E(T) = E_o - \frac{C}{\exp(\frac{T_o}{T}) - 1} \tag{3.3.3}$$

In the above equation, E_o is the elastic modulus at 0 K and C and T_o are constants. The experimental data agree with the fitted results in the temperature range of the investigation for NbMoCrTiAl, NbMoTiAl, and MoCrTiAl. The report of compressive stress decreasing with temperature and increased ductility can be attributed to the thermally sensitive response of the materials. The softening of the elastic modulus with a thermally activated slip process can explain the ductility and lower compressive yield stress above room temperature [47, 151].

Temperature (°C)	**NbMoCrTiAl**	**NbMoTiAl**	**MoCrTiAl**
293	207.0 ± 2.9	199.1 ± 7.8	219.4 ± 6.9
373	192.6 ± 8.3	191.2 ± 1.6	194.7 ± 1.6
473	172.0 ± 8.1	172.8 ± 3.3	181.5 ± 5.7
573	167.2 ± 4.9	160.6 ± 3.6	181.1 ± 5.9
673	155.7 ± 2.4	153.9 ± 5.9	153.3 ± 3.3

Table 3.3.4: Elastic modulus shows a decrease as a function of temperature considered at 1400 to 1600 nm depth of indentation.

The same is reported for TiNbHfZrTa by Laplanche et al. [148], that the elastic modulus decreases with temperature, following the equation proposed by Varshni [150]. The softening of the elastic modulus with temperature for this alloy is related to that of its constituent elements. It was observed that with Hf, Zr, and Ti having a hexagonal closed packed (HCP) crystal structure, they show an increase in elastic modulus with temperature. This is due to the change in structural stability caused by the change in the HCP phase to BCC with increasing temperature [148, 152]. The elastic softening is compensated for by the change in the structure, which increases structural stiffness. Nb, on the contrary, exhibits almost no change in modulus with temperature [153]. This abnormal response arises from the elastic strain that displaces the Fermi surface and electron transfer at the Brillouin zone boundaries. However, the elastic modulus of Ta decreases with temperature; this is a normal phenomenon due to temperature-induced softening [154].

On the basis of this explanation of the relation of the elastic modulus response of the alloy to that of its con-

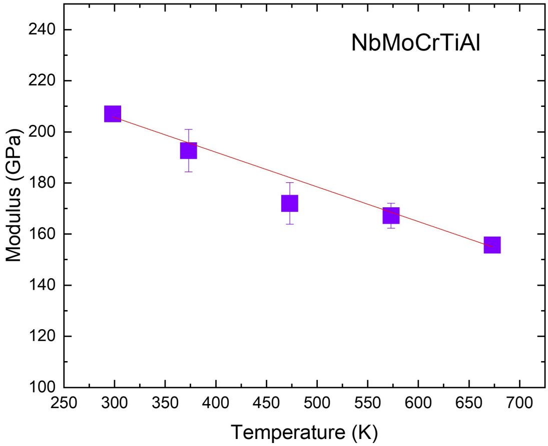

(a)

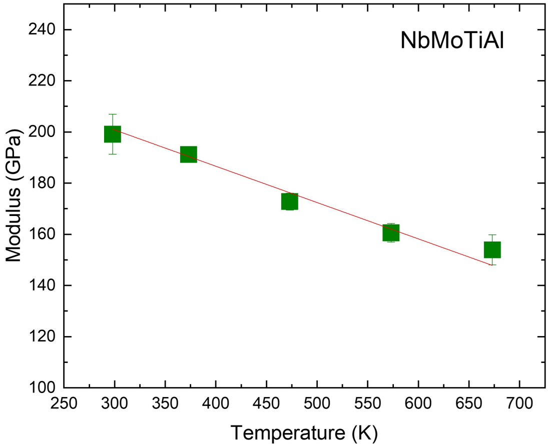

(b)

Figure 3.3.9: The variation of elastic modulus with temperature for (a) NbMoCrTiAl and (b) NbMoTiAl. The red line is the least square approximation fitting based on Varshni's [150] equation relating modulus of elasticity to temperature.

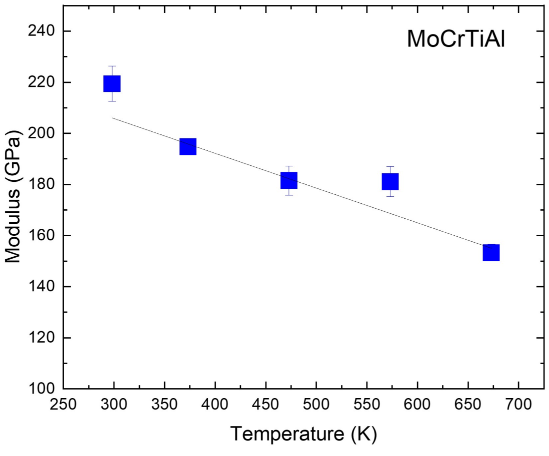

(c)

Figure 3.3.10: The variation of elastic modulus with temperature for (c) MoCrTiAl. The red line is the least square approximation fitting based on Varshni's [150] equation relating modulus of elasticity to temperature.

stituents as a function of temperature, the properties of NbMoCrTiAl and its alloy system are further explained. For the NbMoCrTiAl alloy system, in addition to Nb and Ti, the other elements [152, 153, 155], namely Mo, Cr and Al [156–158] are reported to show temperature-induced softening. For the concerned range of temperature, Cr shows a drop in the elastic modulus around 300 K. At this temperature Cr also undergoes magnetic reordering, which is a transition from antiferromagnetic to paramagnetic. This structural modification leads to modulus to henceforth increases. Beyond this temperature, which is usually less than >473 K [158] elastic modulus gradually decreases, leading to the usual softening. Taking into account the effect of temperature on the modulus of each of the constituent elements, the modulus of the alloys NbMoCrTiAl, NbMoTiAl, and MoCrTiAl as a whole undergoes a reduction in the elastic modulus, and thus the modulus is softened as a whole.

Chen et al. [22] reported that NbMoCrTiAl and its derivatives NbMoTiAl and MoCrTiAl undergo an order-disorder transition from an ordered B2 phase to a disorder A2 phase above 800 K. However, since the experiments were performed in a temperature range up to 673 K, the effect of this transformation on the elastic modulus could not be observed, if any.

The BCC crystal systems are very sensitive to temperature. The activation of the slip system and the yield stress is thermally sensitive. Figure 3.3.11 shows the variation of hardness with temperature for NbMoCrTiAl and its derivatives (table 3.3.5). This temperature-dependent yield response depends on the homologous temperature of the system. In the given temperature range, it can be seen that the hardness decreases from room temperature to 573 K. However, from 550 K the hardness appears to approach the plateau-like regime.

Temperature (K)	**NbMoCrTiAl**	**NbMoTiAl**	**MoCrTiAl**
293	8.37 ± 0.26	6.38 ± 0.3	7.71 ± 0.29
373	7.40 ± 0.32	5.29 ± 0.07	6.84 ± 0.13
473	6.11 ± 0.39	4.61 ± 0.13	5.91 ± 0.21
573	5.49 ± 0.19	4.22 ± 0.06	5.88 ± 0.14
673	6.05 ± 0.12	4.20 ± 0.23	5.03 ± 0.15

Table 3.3.5: Hardness as a function of temperature showing the decrease of it as the temperature increases for the three alloys considered at 1400 to 1600 nm depth of indentation.

For BCC crystal systems, the yield strength and hardness

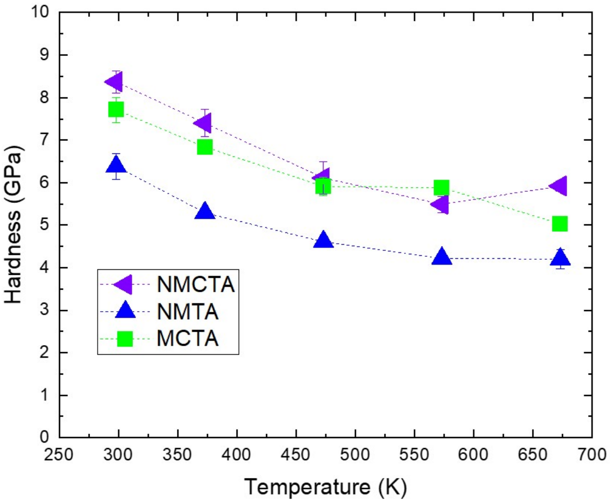

Figure 3.3.11: Nanohardness is observed to decreasing with temperature for NbMoCrTiAl and its derivative alloys. A slight hardness increase is observed for NbMoCrTiAl at 673K

as a function of temperature can be categorised into three different regimes such as the low-temperature, plateau, and high-temperature regime. Seeger [58] categorised these regimes for BCC crystal systems based on the rate-determining step to induce plasticity, primarily the varied movement of the kink under the thermal response in a given temperature range.

The kink pair is the prominent dislocation defect controlling the plasticity and work hardening in a BCC crystal system. A double combination of the screw and edge stair-like dislocation moves under stress from one Peierls valley to another facilitating the dislocation motion. This movement is thermally activated and is thus classified into three thermal regimes. In a lower temperature regime, the strength of the system decreases with temperature, as the kink pair formation and movement are thermally activated. Either the determining points are that the elastic interaction between the kink pairs is high, or the critical kink width or the distance between the dislocation cores to overcome the Peierls potential is too low. The next regime comes into play beyond knee temperature. It is the critical temperature beyond which the strength of the system is athermal, and thus the plateau is reached. The independence of the strain rate continues until the high-temperature regime starts, and diffusion due to thermal excitation leads to a decrease in strength.

For the given system of MPEAs of NbMoCrTiAl, the plateau appears to reach 500 K. As reported by Chen et al. [23] in macroscopic compression tests, NbMoCrTiAl and NbMoTiAl show considerable ductility from 600 K and MoCrTiAl from 400 K. The strength drop is observed at 1273 K, 1073 K, and 873 K for NbMoTiAl, NbMoCrTiAl, and MoCrTiAl, respectively. Since for nanoindentation, the corresponding yield stress of a Berkovich indenter is 7% plastic deformation under uniaxial loading, the work hardening behaviour affects the stress response and, thus, the hardness and strength. In correlating the temperature results from the nanohardness and macro compression tests, it can be concluded that the knee temperature for NbMoCrTiAl and NbMoTiAl is around 573 K and 473 K for MoCrTiAl. This is in accordance with the T_{knee} determined for NbMoCrTiAl by Chen et al. [60]. This can be seen in the fact that the hardness of the elastic modulus and T_{knee} from the nanoindentation are not just a function of the temperature but also the increase in Nb and Cr in the system.

3.3.3 Pop-in and dislocation nucleation

The load on the sample vs. displacement into the surface curve with a sudden burst in the displacement or pop-in is shown in figures 3.3.12 and 3.3.13. During indentation on the surface of a material with no pre-existing dislocations, the dislocation burst occurs when the maximum shear stress beneath the indenter, which should be approximately around $\frac{1}{7}$ to $\frac{1}{8}$ of the shear modulus, approaches the theoretical shear strength of the alloy. The maximum shear stress under the indenter at the pop-in load is calculated using equation 3.3.2 and tabulated in table 3.3.3 for the load rates of 0.01 $\mathrm{mNs^-1}$ and 0.005 $\mathrm{mNs^-1}$. The ratio of maximum shear stress to the reported shear modulus is around $\frac{1}{7}$ to $\frac{1}{9}$. This suggests that the nucleation process for the dislocation in the sample is initiated by stress.

The maximum shear stress (τ_{max}) leading to the pop-in indicating dislocation nucleation reduces with the load rate (figure 3.3.14b and table 3.3.6). Thermal fluctuation tends to persist for longer with a decreasing load rate, allowing lower shear stress beneath the indent to promote the onset of plasticity or the initiation of nucleation of dislocations. This leads to the theory of thermally assisted and stress-initiated homogeneous nucleation of the dislocation in grains without preexisting movable dislocations [123]. As mentioned earlier, the energy requirement for homogeneous nucleation is unusually large, so the process of nucleation is thermally assisted and stress-initiated heterogeneous nucleation. As shear stress is a function of the load rate, a greater change in shear stress with a change in load rate indicates the influence of stress and temperature, which is seen more prominently in MPEAs compared to pure FCC metals such as Pt [123] or pure BCC metal Ta [159].

It can also be noted that the maximum shear stress is a function of the alloying composition with changing load rate. The difference in the maximum shear stress at pop-in is much larger for MoCrTiAl with changing load rate in comparison to that of NbMoCrTiAl. The difference can also be observed in the four components, NbMoTiAl, which is lesser than MoCrTiAl. As the indentations for a particular load rate are concentrated on a single grain,

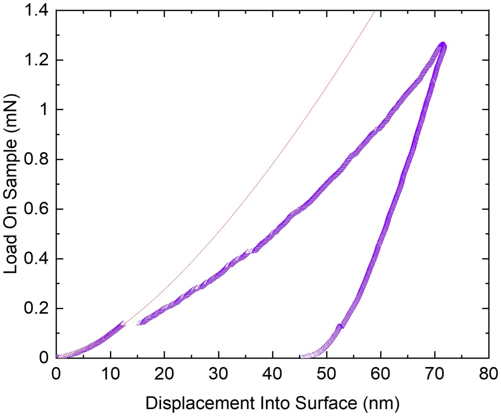

(a) NbMoCrTiAl

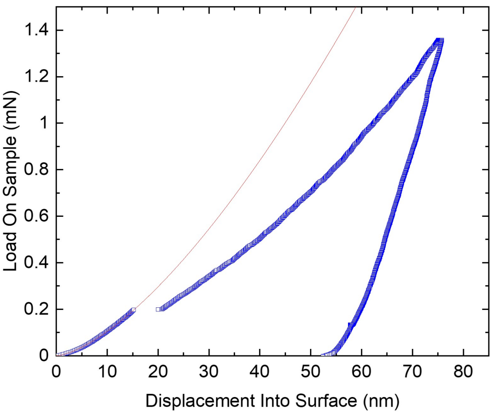

(b) MoCrTiAl

Figure 3.3.12: Load on sample vs displacement into the surface curve for (a) NbMoCrTiAl and (b) MoCrTiAl under 0.01 mNs^{-1} showing the distinct pop-in and the different pop-in length.

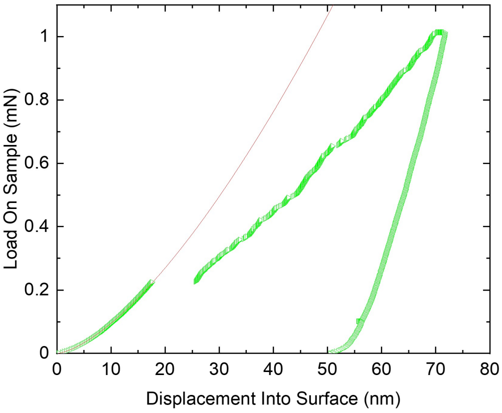

(a) NbMoTiAl

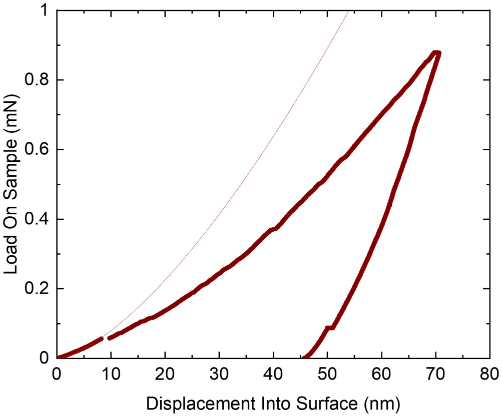

(b) TiNbHfZrTa

Figure 3.3.13: Load on sample vs displacement into the surface curve for (a) NbMoTiAl and (b) TiNbHfZrTa under 0.01 mNs^{-1} showing the distinct pop-in and the different pop-in length.

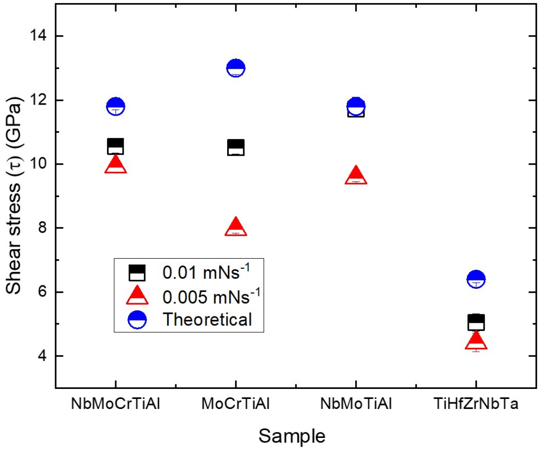

Figure 3.3.14: The variation in the shear stress as a function of varying load rates of 0.01 mNs^{-1} and 0.005 mNs^{-1} and the theoretical shear stress is higher than calculated from the different load rates.

the grain orientation can result in a large difference in the maximum shear stress for different load rates in a system compared to the others.

The pop-in length can be calculated from the load-displacement graph obtained during nanoindentation. It is calculated as the change in displacement over a constant load that results in a sudden discontinuity in the graph (Figures 3.3.12 and 3.3.13). The pop-in length has been reported to be much more pronounced for BCC alloys compared to FCC metals or alloys [123, 160] due to the high Peierls stress required by a dislocation to overcome the Peierls barrier. The requirement of high Peierls stress is a result of the complex dislocation core in BCC [159]. Although the given nanoindentation system could not help determine the exact length of the pop-in, a comparison can be established between TiHfZrNbTa (figure 3.3.13b) and the family of

NbMoCrTiAl MPEAs (figures 3.3.12a,3.3.12b and 3.3.13a).

TiNbHfZrTa shows the pop-in length commonly observed in alloys or elements with a crystal structure of FCC [161] or for systems with multiple preexisting dislocations or where dislocations are generated from surface steps [125]. The family of NbMoCrTiAl MPEAs shows a distinct large jump like most BCC systems [159] compared to that of TiNbHfZrTa. Large pop-in jumps can also indicate homogeneous nucleation of dislocations or unlocking pinned dislocations or dislocations generated from stress concentrators such as interstitial or vacancies. This comparison of the pop-in length gives an indication of the fundamentally different dislocation nucleating process between the TiNbHfZrTa and NbMoCrTiAl families of MPEAs.

Load rate		**0.01mNs^{-1}**		**0.005mNs^{-1}**	
Samples	$\tau_{\mathbf{th}}$ **(GPa)**	$\tau_{\mathbf{max}}$ **(GPa)**	$\tau_{\mathbf{max}}/\mathbf{G}$	$\tau_{\mathbf{max}}$ (GPa)	$\tau_{\mathbf{max}}/\mathbf{G}$
NbMoCrTiAl	11.8 ± 0.1	10.4 ± 0.2	1/7	9.8 ± 0.2	1/8
MoCrTiAl	12.4 ± 0.2	11.8 ± 0.2	1/7	8.1 ± 0.1	1/9
NbMoTiAl	11.8 ± 0.3	11.6 ± 0.2	1/6	9.7 ± 0.1	1/8
TiNbHfZrTa	6.4 ± 0.1	5.4 ± 0.1	1/8	4.4 ± 0.5	1/9

Table 3.3.6: The theoretical shear stress for the alloys calculated from elastic modulus and Poisson's ratio $\tau_{th} = \frac{E}{4\pi(1+\nu)}$ and the shear stress obtained at the point of pop-in under 0.01mNs^{-1} and 0.005mNs^{-1}

3.3.4 Varying strain rate and dislocation motion

The variation of the hardness and elastic modulus as a function of the strain rate for the four materials: NbMoCrTiAl, NbMoTiAl, MoCrTiAl, and TiNbHfZrTa are shown in figure 3.3.15. These results are averaged values of the properties over a depth of 1000 to 1600 nm. It can be seen that both properties show a sudden drop at the strain rate 0.005 s^{-1}.

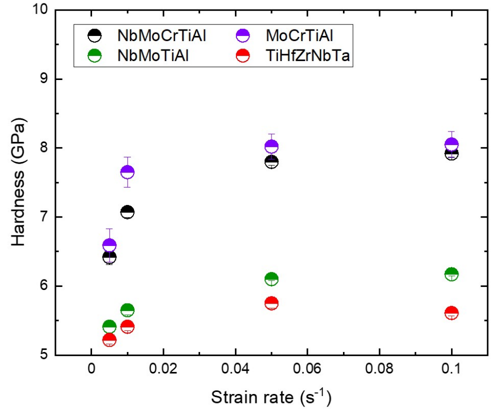

(a)

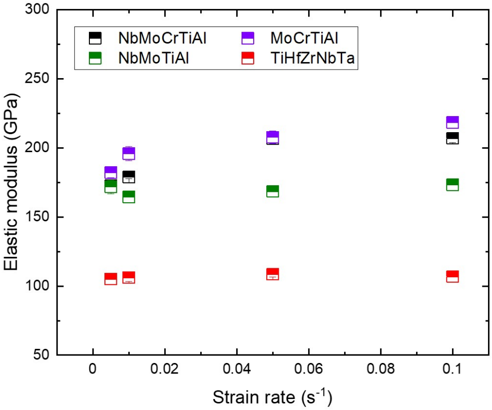

(b)

Figure 3.3.15: The variation of (a) hardness and (b) elastic modulus over 0.005, 0.01, 0.05 and 0.1 s^{-1} for NbMoCrTiAl, NbMoTiAl, MoCrTiAl and TiNbHfZrTa can be seen. Increasing the strain rate increases the hardness and elastic modulus. However, the elastic modulus is not a function of strain rate for TiNbHfZrTa.

As the strain rate sensitivity is intended to be calculated over a varying depth of indentation, the hardness and elastic modulus of each sample are considered over the depth of 1000, 1200 1400 and 1500 nm. As observed in figures 3.3.16 and 3.3.17, the elastic modulus does not vary with changing depth and exhibits a similar trend as seen in figure 3.3.15b.

The hardness over the four concerned depths for the varying strain rates is plotted in figure 3.3.18 and 3.3.19. The variation of hardness over depth for different strain rates is less prominent in TiNbHfZrTa than in NbMoCrTiAl and its derivative alloys. This points to the fact that NbMoCrTiAl and its derivatives, as mentioned in Section 3.3.1, are strongly indentation-size dependent compared to TiNbHfZrTa.

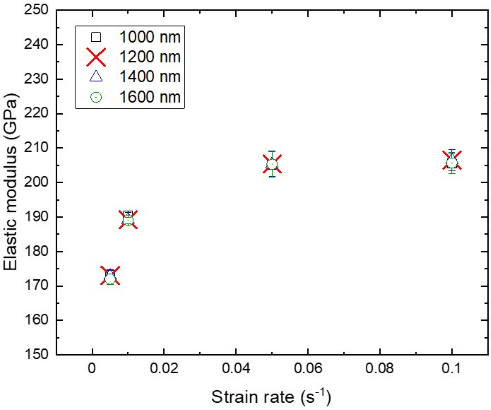

(a) NbMoCrTiAl

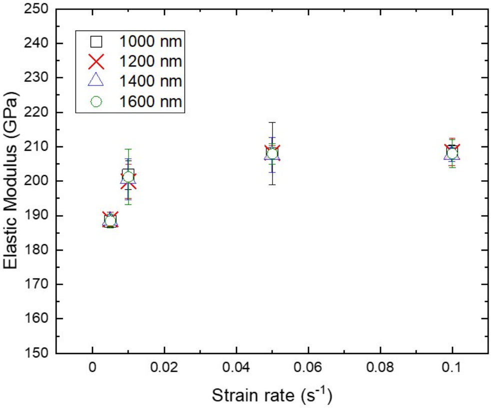

(b) MoCrTiAl

Figure 3.3.16: The elastic modulus over the strain rates at different depths of 1000, 1200, 1400 and 1600 nm for (a) NbMoCrTiAl and (b) MoCrTiAl. The modulus increases with the strain rate but is constant over different depth of indentation for NbMoCrTiAl and MoCrTiAl.

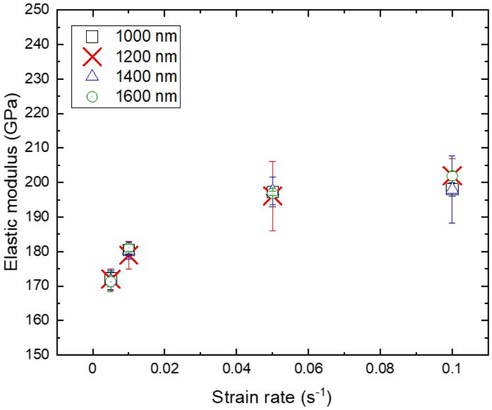

(a) NbMoTiAl

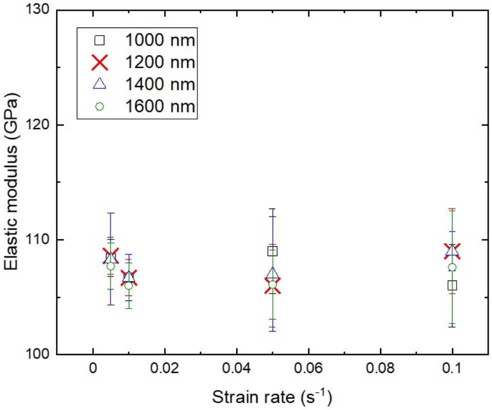

(b) TiNbHfZrTa

Figure 3.3.17: The elastic modulus over the strain rates at different depths of 1000, 1200, 1400 and 1600 nm for (a) NbMoTiAl and (b) TiNbHfZrTa. The modulus increases with the strain rate but is constant over different depth of indentation for MoCrTiAl. The modulus remains constant over different strain rate for TiNbHfZrTa.

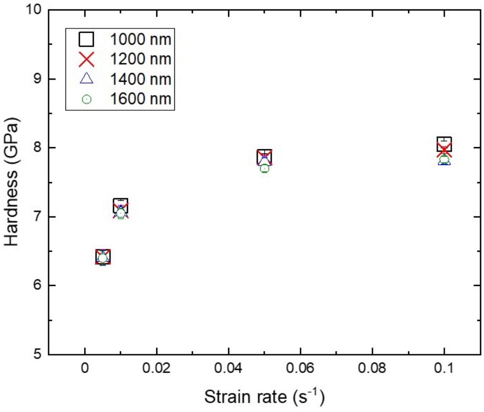

(a) NbMoCrTiAl

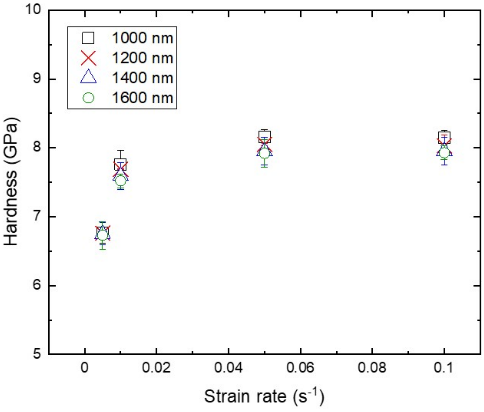

(b) MoCrTiAl

Figure 3.3.18: The hardness over the strain rates at different depths of 1000, 1200, 1400 and 1600 nm for (a) NbMoCrTiAl and (b) MoCrTiAl. The hardness increased with strain rate for NbMoCrTiAl and MoCrTiAl.

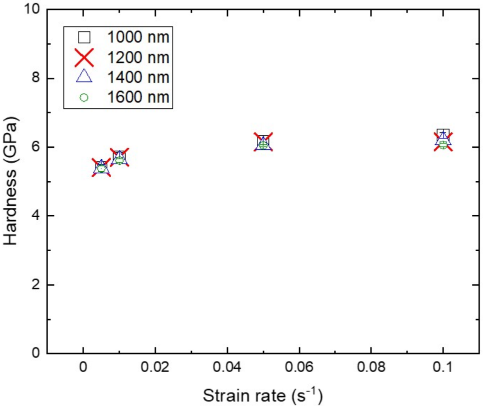

(a) NbMoTiAl

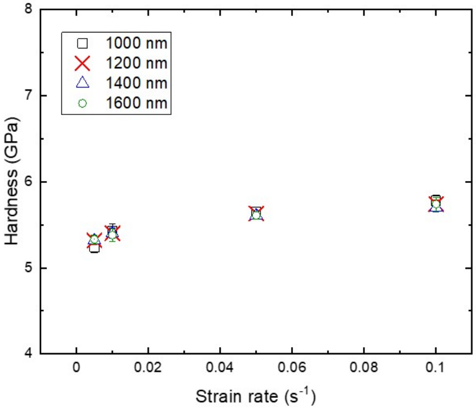

(b) TiNbHfZrTa

Figure 3.3.19: The hardness over the strain rates at different depths of 1000, 1200, 1400 and 1600 nm for (a) NbMoTiAl and (b) TiNbHfZrTa. The variation of hardness over strain rate for NbMoTiAl and TiNbHfZrTa is negligible

3.4 Discussion

3.4.1 Solid solution strengthening

In the athermal regime, the strengthening in the system is the result of solid solution strengthening in a single-phase alloy system. This brings us to the understanding of the strengthening mechanisms of MPEAs, especially solid solution strengthening, and its effect on the nanomechanical properties.

It has been widely established that the elastic interaction between the solute and the dislocation results in solid solution strengthening. The stress field of edge dislocation interacts with the solutes present in the system. Screw dislocation can also interact with solute atoms in an anisotropic system. In a solid solution, the strengthening factors are the modulus mismatch and the atomic size mismatch. The solid solution for MPEAs, on the one hand, is difficult to understand and thus the calculation and implication of the modulus and atomic size mismatch are not straightforward.

In a binary system, the solute and solvent are two different species and the elastic interaction force between the solute and the elastic stress field of the dislocation is given as:

$$f_m = Gb^2\delta = Gb^2(\delta_G + \beta\delta_\alpha) \tag{3.4.1}$$

where G and b are the shear modulus and Burgers vector, respectively. β is a constant depending on the type of dislocation.δ_G and δ_α are the modulus misfit and the lattice misfit, respectively, which are calculated as the change in the modulus and lattice size with the change in solute concentration. This is in line with the Fleischer model [162, 163]. However, this model is defined for the regular concentration of solutes in the system. The interaction of the solutes increases with the dislocations and is no longer individually responsible for a more concentrated solid solution, such as that in MPEAs. Solutes act as a group and stress increases around this group of solutes [21].

This is when the line tension of the dislocation comes into play. The increase in the solute stress is given as

$$\sigma = AG\delta^{4/3}c^{2/3} \tag{3.4.2}$$

Here, c is the concentration of the solute and A is a constant ~ 0.1.

However, this definition changes for MPEAs as there is no defined solute and solvent in an MPEA. This is due to the equimolar and near equimolar composition of the system containing 4 or 5 different elements. So, a multi-element interaction is expected. Nevertheless, on the basis of the solvent-solute model, the modulus mismatch and lattice mismatch for the MPEAs used in this work are calculated.

As explained by Senkov et al. [21] for a BCC crystal system, in a highly concentrated solid solution, every atom will interact with its 8 neighbouring atoms, and not just a solute and solvent interaction, as seen in a binary solid solution system. So, the lattice distortion and modulus mismatch can be written as equation 3.4.3 and equation 3.4.4, respectively.

$$\delta_a = \frac{9}{8}\sum c_j \delta_{a_{ij}} \tag{3.4.3}$$

$$\delta_G = \frac{9}{8}\sum c_j \delta_{G_{ij}} \tag{3.4.4}$$

For the element i as the centre, c_j is the concentration of the other elements and

$$\delta_{a_{ij}} = 2(r_i - r_j)/(r_i + r_j) \tag{3.4.5}$$

$$\delta_{G_{ij}} = 2(G_i - G_j)/(G_i + G_j) \tag{3.4.6}$$

$\delta_{a_{ij}}$ and $\delta_{G_{ij}}$ are the atomic size difference and the shear modulus difference for elements i and j. The average modulus and lattice parameter of the alloy are considered to be the effective matrix. The atomic radius and modulus difference is calculated using the enlisted value for the elements in Appendix A.3. Figure 3.4.1, and tables 3.4.1 and 3.4.2 show the lattice and shear modulus distortion for element in the systems, respectively.

A comparative distortion result for TiHfZrNbTa is shown in figure 3.4.2a, as reported by Senkov [164]. It can be seen that Hf and Zr have little atomic size differences between each other but larger size differences with Ti, Nb, and Ta. The smaller elements exert a local tension around themselves, whereas the larger elements Zr and Hf exert a local compression. For a uniformly distributed alloy, TiHfZrNbTa can be considered as a binary system where the large atoms act as solutes and the smaller atoms act as the solvent matrix. This assumption helped to calculate an atomic lattice misfit of around 9% and without considering the modulus misfit the solute stress in the system is around 221 MPa and the interactive force is around 2.8×10^9N.

	NbMoCrTiAl	**NbMoTiAl**	**MoCrTiAl**
$\delta_{\mathbf{a.Nb}}$	0.0354	0.0062	—
$\delta_{\mathbf{a.Mo}}$	-0.0131	-0.0423	-0.0042
$\delta_{\mathbf{a.Cr}}$	-0.1168	—	-0.1079
$\delta_{\mathbf{a.Ti}}$	0.0511	0.0219	0.0600
$\delta_{\mathbf{a.Al}}$	0.0433	0.0141	0.0521

Table 3.4.1: The lattice misfit calculated for each element with its neighbour for each system NbMoCrTiAl and its family of alloys.

The shear modulus mismatch shows that Ta has the largest shear modulus difference with other elements of the system, thus contributing and dictating the modulus effect on the solid solution model (figure 3.4.2b). In light of

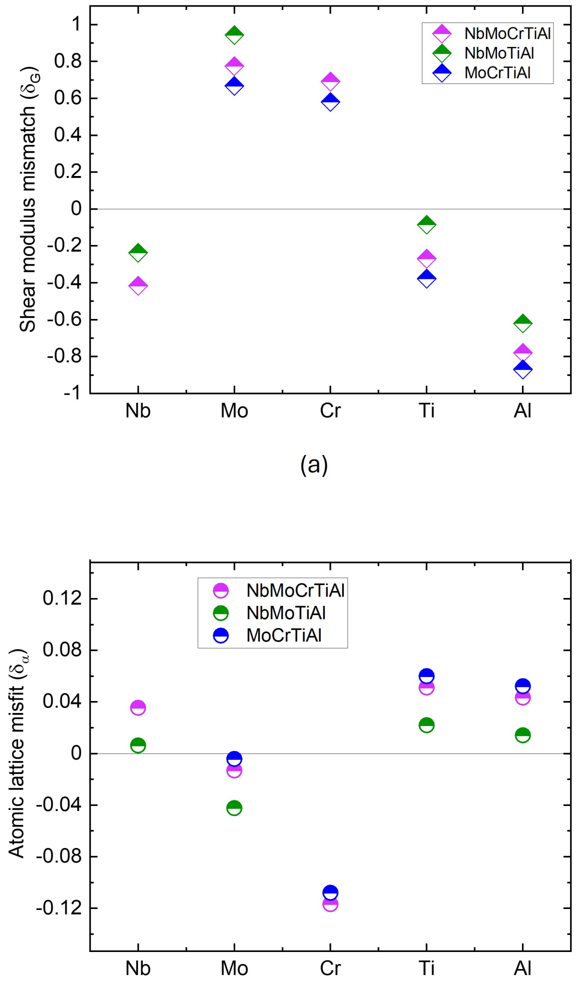

(a)

(b)

Figure 3.4.1: (a) The shear modulus mismatch of each element with each system shows Mo is the element that effects the most and (b) the atomic lattice misfit shows for NbMoCrTiAl and MoCrTiAl, Cr is exerts tension on the lattice.The other elements do not show strong compression on the systems.

	NbMoCrTiAl	**NbMoTiAl**	**MoCrTiAl**
$\delta_{\mathbf{G.Nb}}$	-0.4164	-0.2375	—
$\delta_{\mathbf{G.Mo}}$	0.7751	0.9432	0.6670
$\delta_{\mathbf{G.Cr}}$	0.6909	—	0.5805
$\delta_{\mathbf{G.Ti}}$	-0.2693	-0.0855	-0.3778
$\delta_{\mathbf{G.Al}}$	-0.7801	-0.6201	-0.8697

Table 3.4.2: The shear modulus misfit calculated for each element with its neighbour for each system NbMoCrTiAl and its family of alloys.

Varvenne's [165] model for MPEA, the matrix or the solution is the average of all elements and its properties are the average of all the elements present. The model also states that each element individually acts as a solute to the average matrix. Laplanche et al. [148] proposed, similar to Senkov et al. [21], that Ta provides the strengthening effect due to the large modulus mismatch.

NbMoCrTiAl family of MPEAs, as seen in figure 3.4.1b do not have elements with similar lattice distortion and large lattice distortions. All the lattice distortions of each element are in the range of 2% to each other. However, Ti and Al always resulted in compressive stress in their neighbourhood, and the distortion is not prominent for Nb and Mo. Cr contributes to the largest lattice distortion in the systems.

The effect of lattice mismatch for NbMoCrTiAl systems:

NbMoCrTiAl: for this quinary system, it can be observed that Nb, Ti, and Al exert compressive stress around their neighbours and have a similar lattice mismatch to the average. However, Mo appears to have almost no mismatch and Cr tends to have the most mismatched lattice, exerting tensile stress around itself. The distribution can be imagined as a matrix of large atoms such as Nb, Mo,

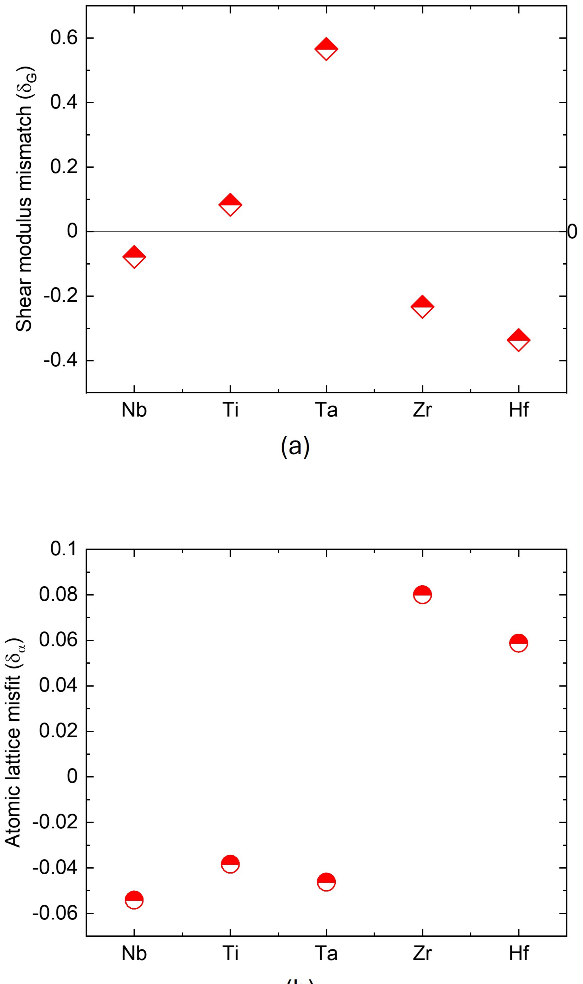

(a)

(b)

Figure 3.4.2: (a) The shear modulus mismatch for TiNbHfZrTa with its constituent elements shows Ta has the highest mismatch and (b) the atomic mismatch for TiNbHfZrTa with its constituent elements show Hf and Zr exerts compression on the lattice where as Nb,Ti and Ta exerts tension on the lattice.

Ti, and Al with Cr as the solute distributed on the surface. So, δ_a can be roughly ~ -0.18. Without the contribution of modulus distortion, the interactive force due to lattice distortion can be calculated as $f_{ma} = 20.25 \times 10^{-10}$N.

NbMoTiAl: in this quaternary system, Mo shows the largest modulus mismatch, exerting tensile stress around itself. Nb again does not show a major difference from the average lattice. Ti and Al impart compressive stress, but the lattice mismatch is not very evident. Thus, it can be considered that the lattice mismatch effect is contributed by Mo alone, and therefore δ_a is 0.05. This results in an interactive force of $f_{ma} = 5.82 \times 10^{-10}$N.

MoCrTiAl: with the presence of Cr, this quaternary system observes the largest lattice mismatch from Cr. This results in $\delta_a \sim 0.16$ and $f_{ma} = 180.1 \times 10^{-10}$N. Ti and Al along with Mo can be considered as the matrix with Cr as the solute in the system.

The above-described lattice mismatch and the interactive force in context with Labusch's solid solution model and statistical model [162, 163], clearly indicate that Cr adds to solid solution strengthening. The lattice mismatch increases with the presence and content of Cr and this can be clearly seen by the nanohardness in this work and the results of the microhardness and compressive test [23, 60]. MoCrTiAl exhibits strength more than that of NbMoCrTiAl, which is also greater than that of the quaternary system without Cr i.e. NbMoTiAl.

With respect to the shear modulus mismatch (figure 3.4.1a) it can be observed from the table and the figure that Cr, Mo, and Al all have large mismatches from the average matrix. As all of the alloys in the investigation contain Mo and Al, the deciding effect is due to the addition of Cr. In NbMoTiAl, without Cr, Mo adds to the modulus mismatch more than Al and thus contributes to the strengthening of this quaternary alloy. Therefore, no decisive factor for shear modulus mismatch can be determined that helps strengthen systems.

Chen et al. [60] took a different route to assess lattice distortion and the consequent hardening in the system [165, 166]. This approach considers that the alloy has an effective lattice parameter because of the size of the individual elements present, and the variation is caused by that. This is an unrealistic approach, but this gives the scope of understanding the solid solution strengthening due to lattice distortion. The lattice parameter (δ) is therefore calculated using the equation suggested by Vegard.

$$\delta = 100\% \sqrt{\sum_i x_i (1 - r_i / r_{mean}^2)} \qquad (3.4.7)$$

r_{mean} is the mean atomic radius for the alloy, which is equal to $\sum_i x_i r_i$, where r_i and x_i are the atomic radii and the atomic molar fraction of the element i in the alloy. As Varvenne et al. [165] suggested, in the case of MPEAs of a specific crystal structure, they can be composed of elements of different crystal structures, resulting in a change in the binding state of the element. That in turn contributes differently to the lattice distortion. An element having the same crystal structure as the alloys has a constant binding state. Because Nb, Mo, and Cr have the same crystal structure as the MPEAs in question, i.e., BCC, the atomic radii in consideration do not change. However, the atomic radii of the alloy changes as a result of other elements such as Al and Ti, because they have FCC and HCP crystal structures, respectively.

Chen et al.[60] developed an overdetermined set of equations based on Vegard's law and calculated the lattice distortion for NbMoCrTiAl and its family of alloys. The recalculated atomic radii of the alloys were in agreement with the atomic radii determined by X-ray diffraction (XRD) and thus this approach was considered valid. The lattice distortion following the discussed rule was calculated and shown in figure 3.4.3a.

The increased amount of Cr in the system decreased the

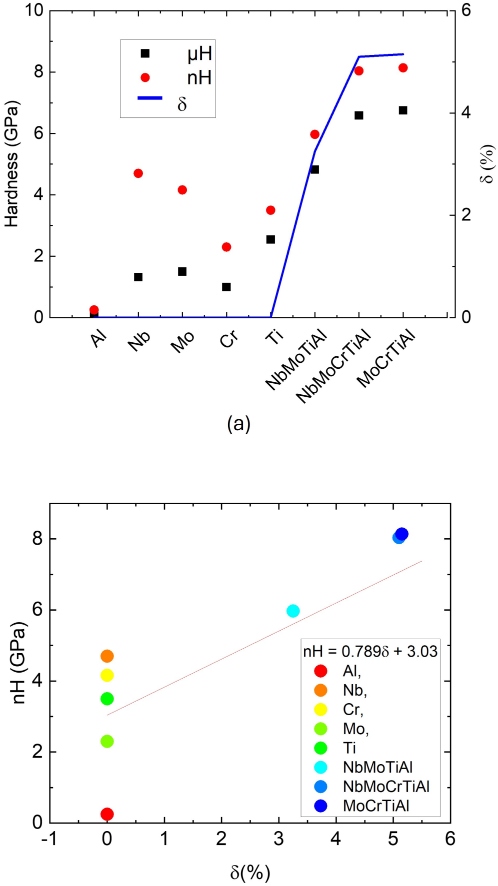

(a)

(b)

Figure 3.4.3: (a) The nanohardness (nH) and the microhardness (μH) vary as the lattice distortion. The pure elements are recorded as zero lattice distortion. The microhardness and nanohardness data of the elements and NbMoCrTiAl and its derivatives are obtained from [60]. (b) The nH is a function of the lattice distortion. A linear approximation links the distortion of the lattice of the three MPEAs with the nanohardness, suggesting the variation in the composition and its effect on the distortion and mechanical properties. The nanohardness of the MPEAs increases with increasing lattice distortion.

lattice parameter and vice versa for the quantity of Nb. The lattice distortion (δ_a) for NbMoTiAl, NbMoCrTiAl, and MoCrTiAl are 3.2%, 5.3% and 5.8% respectively. Cr increases the lattice distortion in this alloy system. Kube [115] reported that the lattice distortion for TiNbHfZrTa using the same equation is 5.5%. The mechanical property of nanohardness (nH) is plotted along with microhardness (μH) [60] and the lattice distortion in the figure. The hardness values of the individual elements are also plotted without lattice distortion [60, 158, 167]. The atomic size difference and the hardness are seen to follow the same trend. The change in nH with decreasing Nb and adding Cr from NbMoTiAl to NbMoCrTiAl is evident as the change in the lattice distortion. This supports the theory of gradual change in property with the change in the lattice parameter proposed by Fleischer and Labusch for the binary alloy system [162, 163, 168].

However, the change in properties is nH and μH is almost constant with the increase in Cr from NbMoCrTiAl to MoCrTiAl. Despite this, a linear correlation of δ_a with nH can be observed as shown in figure 3.4.3b.This is similar to that shown by μH [22] and all the correlations are considered at room temperature. The correlation can be given as nH $= 0.987\delta + 2.967$. As the line energy of the dislocation can be correlated with the change in the shear modulus, the change in shear modulus with the change in composition. The shear modulus calculated from the nanoindentation shows very little deviation from each other, and the correlation with the nanohardness is not linear for the three alloys in the investigation. No correlation was found for μH at room temperature for the same. Thus, the effect of the shear modulus cannot be definitely determined. However, Chen et al. [22, 60] suggest that the presence of ordering in the NbMoCrTiAl family provides strength to the system.

3.4.2 Dislocation nucleation of partials and full dislocations

The statistical analysis of the cumulative frequency of the pop-in results obtained in this work fits the equation 3.1.8 as seen in the figures 3.4.4 and 3.4.5. Data were further analysed according to the equation 3.1.9 to obtain the activation volume for the nucleation of the dislocation from the slope of $\ln|-\ln|1-f||$ versus τ (Figures 3.4.6 and 3.4.7). The activation volume of the samples under different loading rates is tabulated in table 3.4.3.

In table 3.4.3, Ω is the atomic volume given by $\frac{a^3}{2}$, where a is the lattice parameter and b is the Burger vector of the magnitude of (111)/2 full dislocation as is common in BCC elements and alloys. It can be observed (figure 3.4.8) that the activation volume increases with a decrease in load rate for the NbMoCrTiAl family of alloys but remains constant for TiNbHfZrTa.

	Activation volume (b^3)		**Activation volume (Ω)**	
Load Rate (mNs^{-1})	0.01	0.005	0.01	0.005
NbMoCrTiAl	1.28 ± 0.02	1.57 ± 0.01	1.66 ± 0.09	2.04 ± 0.01
MoCrTiAl	1.34 ± 0.02	1.70 ± 0.03	1.74 ± 0.02	2.21 ± 0.04
NbMoTiAl	1.19 ± 0.02	2.13 ± 0.02	1.55 ± 0.02	2.77 ± 0.03
TiNbHfZrTa	0.65 ± 0.02	0.67 ± 0.01	0.84 ± 0.02	0.87 ± 0.01

Table 3.4.3: The activation volume in term calculated for the alloys under 0.01 mNs^{-1} and 0.005 mNs^{-1}

Moreover, the effect of the change in the load rate is more prominent for NbMoTiAl in comparison to that for NbMoCrTiAl and MoCrTiAl, indicating the effect of the alloying fraction or composition on the involved activation volume.

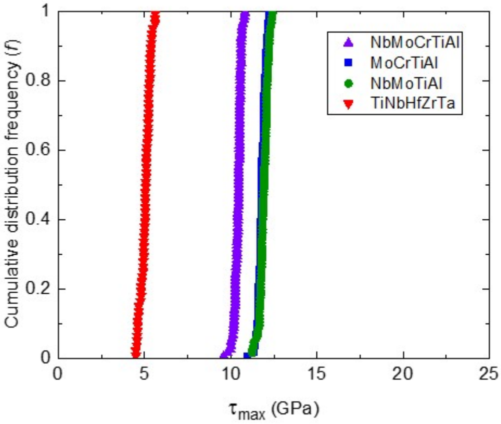

(a)

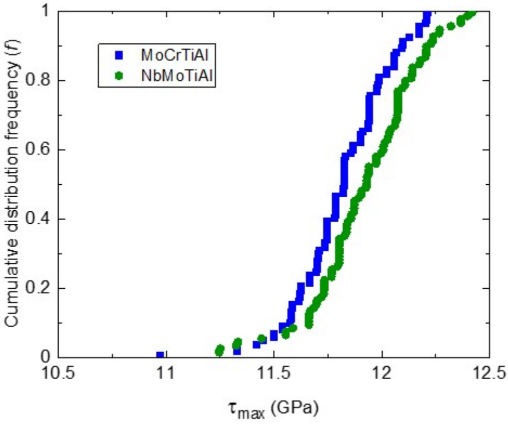

(b)

Figure 3.4.4: (a) and (b) shows the cumulative distribution frequency (f) vs τ_{max} calculated from the pop-in experiments for samples TaNbHfZrTi, NbMoTiAl, MoCrTiAl and NbMoCrTiAl under 0.01mNs^{-1}. The distribution for MoCrTiAl and NbMoTiAl is clearly shown in (b).

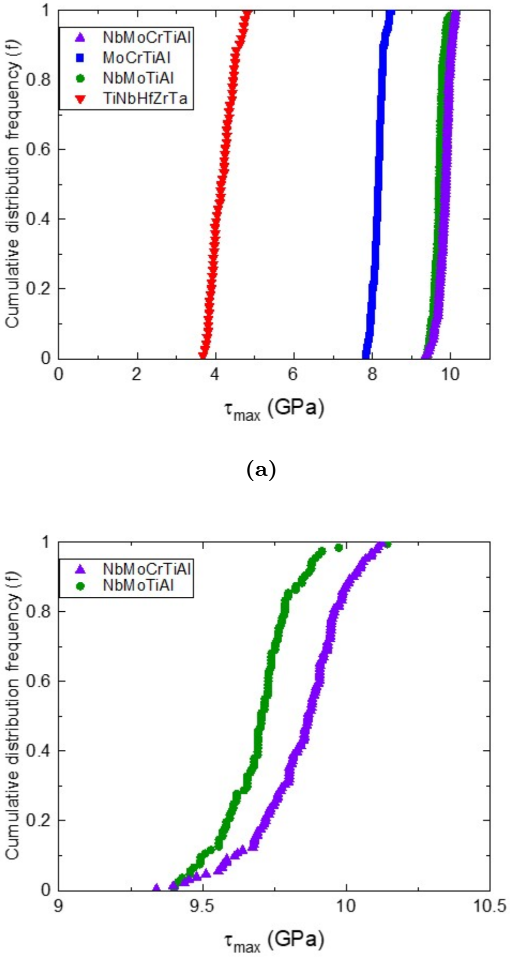

(a)

(b)

Figure 3.4.5: (a) and (b) shows the cumulative distribution frequency (f) vs τ_{max} calculated from the pop-in experiments for samples TaNbHfZrTi, NbMoTiAl, MoCrTiAl and NbMoCrTiAl under0.005mNs^{-1}. The distribution for MoCrTiAl and NbMoCrTiAl is clearly shown in (b).

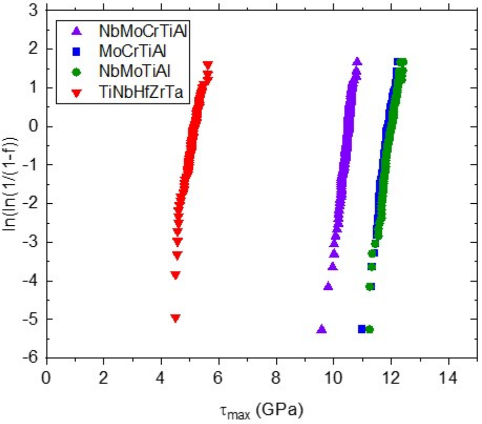

(a)

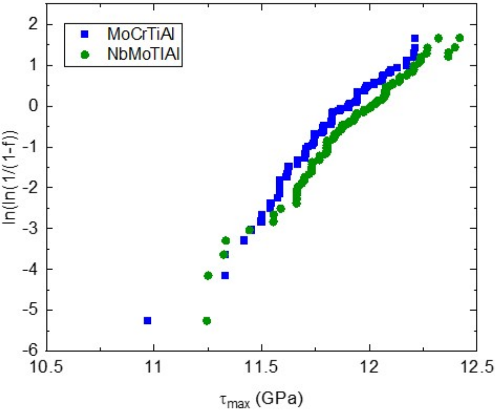

(b)

Figure 3.4.6: (a) shows the linear relation between $\ln|-\ln|1-f||$ and τ for the four samples for $0.01\,\mathrm{mNs^{-1}}$. (b) elaborates the $\ln|-\ln|1-f||$ vs τ for MoCrTiAl and NbMoTiAl

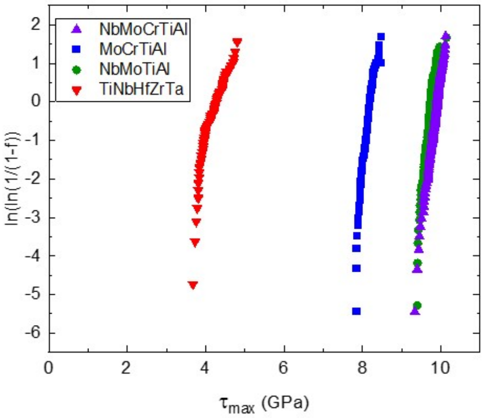

(a)

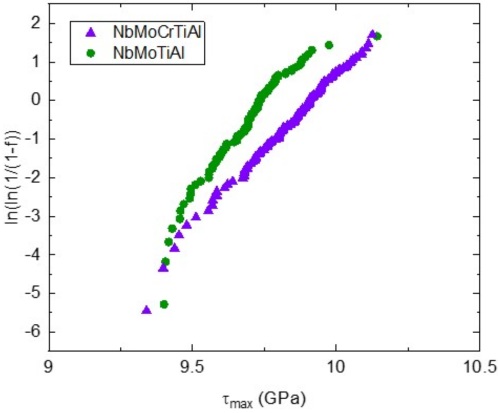

(b)

Figure 3.4.7: (a) shows the linear relation between $\ln|-\ln|1-f||$ and τ for the four samples for $0.005\,\mathrm{mNs^{-1}}$ respectively. (b) elaborates the $\ln|-\ln|1-f||$ vs τ for MoCrTiAl and NbMoCrTiAl.

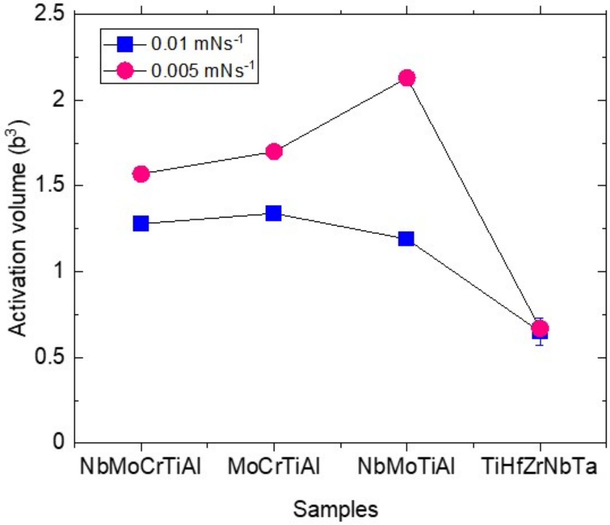

Figure 3.4.8: The variation in activation volume (b^3) for NbMoCrTiAl, NbMoTiAl, MoCrTiAl and TaNbHfZrTi for 0.01 mNs^{-1} and 0.005 mNs^{-1} shows no such effect is observed for TiNbHfZrTa unlike the other MPEAs

Schuh et al. [122] from experiments and Salehinia et al. [147] from MD simulations concluded that heterogeneous nucleation showing the activation volume $1b^3$ involves point defects that facilitate the exchange of atom vacancies in a system, commonly seen in pure BCC metals such as Mo [169]. The energy involved in nucleating a dislocation as in the BCC crystal system by atom-vacancy exchange requires more energy than that required in the FCC crystal system. This is due to the requirement of generating a full dislocation, unlike in FCC where a partial dislocation suffices [169]. However, for Cr, the activation volume involved in nucleating a dislocation is observed to be around $0.3b^3$ [170]. The source of nucleation is still a point defect as in other pure BCC metals, but the presence of a large amount of interstitials and impurities in the open structure of chromium acts as additional sources of stress concentrators. The interstitials reduce the Peierls stress, which reduces the maximum shear stress under indentation and thus energetically favours nucleation of dislocation. Similar phenomena are observed in pure FCC and HCP metals such as Pt and Mg. [123, 171]

The dislocation nucleation behaviour of some MPEAs has also been investigated and reported. Some complex composition alloys such as FeCoCrNiMn (FCC) and TiZrHfNb (BCC) have been reported to cause the movement of a cluster of atoms $(3 \tilde{-} 5\,b^3)$ to initiate dislocation nucleation [172, 173]. This is in contrast to the TiZrNbTa and TiZrNbTaMo HEAs investigated by Wang et al. [174]. They showed that the activation volume of $1b^3$ indicates the nucleation of dislocation through atom vacancy exchange in pure metal BCC.

In this work, the alloys NbMoCrTiAl and its derivative show a similar range of activation volume. It can therefore be concluded that these alloys also initiate dislocation nucleation by atom-vacancy exchange. This is true to the established idea of mechanical behaviour established by Chen et al. [23] who suggested that the NbMoCrTiAl family undergoes deformation by pencil glide. For pencil glide to occur, a full dislocation of $\langle 111 \rangle/2$ is required to nucleate and for a stress-free surface without any pre-existing dislocation and interstitial, atom vacancy exchange is energetically most favourable heterogeneous nucleation of dislocation.

This clearly explains the initiation of plasticity in the MPEA family of NbMoCrTiAl. This family of MPEA has also been reported to have randomly distributed B2 sub-structure and anti-phase boundaries (APB) [22]. The presence of substructures can increase the Peierls stress required to overcome in order to nucleate a dislocation, homogeneous or heterogeneous. Thus, we observe an activation volume that involves slightly more than $1b^3$. As the distribution of the substructure is random and cannot be easily identified, an easy correlation between the location of the indentation and the effect of the substructure cannot be performed.

The activation volume increases with the decrease in the load rate for NbMoCrTiAl and its derivatives, as seen in the figure 3.4.8. The maximum shear stress at the pop-in is also observed to be lower than the theoretical shear stress and then, compared to 0.01 $\mathrm{mNs^{-1}}$, the maximum shear stress at 0.005$\mathrm{mNs^{-1}}$ is lower (figure 3.3.14). This supports the fact that the effect of lowering the thermal fluctuation at the lower load rate allows the event of nucleation to take place at lower stress. The lower thermal fluctuations in the indented region prolong the exposure to the given stress, thus increasing the Peierls stress and affecting the nucleation rate and the dislocation. The increase in the activation volume under a lower load rate supports the theory of pencil glide, since the glide of a full dislocation is a function of temperature in the BCC.

TaHfNbZrTi, like the alloys mentioned above, also undergoes stress-assisted nucleation of the dislocation. However, the activation volume is calculated to be less than $1b^3$ for the Burgers vector of a full dislocation in BCC at $\langle 111\rangle/2$, suggesting that although the atom vacancy exchange is the nucleating procedure, nucleation may involve partial dislocations or preexisting dislocations. Partial dislocations are not generally observed in BCC unless the local stacking fault results in deformation twins. Senkov et al. [21] pointed out that TaHfNbZrTi at room temperature at 60% strain shows deformation twins. According to his work, the presence of twins accommodates the plasticity of this alloy making it more ductile even at room temperature. In order to generate a deformation twin, as studied by Aitken et al. [50] on a representative simulated refractory MPEA BCC AlMoWTa, a $\frac{a}{2}\langle 111\rangle$ complete dislocation split is required into $\frac{a}{3}\langle 111\rangle$, $\frac{a}{6}\langle 111\rangle$ and $\frac{a}{12}\langle 111\rangle$ partials in the $\{112\}$ plane. In a stable $\{112\}$ fault plane, two partial $\frac{a}{3}\langle 111\rangle$ separated by an atomic distance lead to a twin formation, making the $\frac{a}{6}\langle 111\rangle$ the dominant partial. The local chemistry of the non-equiatomic elemental distribution in MPEAs can reduce the stacking fault energy in and around the nearest neighbours under hydrostatic force [175] promoting the nucleation of twins over dislocation slip. This opens up further speculation on the local non-equiatomic distribution of elements in MPEAs and their effect on the generation of favourable faults.

Upon comparing the cumulative probability of the pop-in with τ_{max}/G, Ye et al. [173] suggested that the activation energy can be understood from the distribution of the data. The higher cumulative distribution frequency (CDF) of τ_{max}/G suggests a variation of the shear stress for the pop-in, which is possible for dislocation nucleation involving a lesser energy. Thus, Ye et al. [173] identifies the broader CDF for FCC where the dominating factor of dislocation nucleation and plasticity are the partials. The narrower CDF, in turn, suggests the involvement of a particular energy required in the dislocation nucleation that is considerably high, like that required for nucleating full dislocations. These are commonly seen in BCC that contains the complex dislocation core. Thus, it can be concluded that a broader CDF of τ_{max}/G indicates the involvement of lesser complex dislocation cores or the overcoming of lower Peierls stress.

As shown in figure 3.4.9 the slope of CDF vs τ_{max}/G has a narrower distribution for the NbMoCrTiAl family of MPEAs under 0.01 and 0.005 $\mathrm{mNs^{-1}}$, similar to the BCC reported by Ye suggesting the activation of full dislocations, which are generally required for pencil glide in BCC crystal system. However, it can be observed that the distribution for TiNbHfZrTa is broader than that of the NbMoCrTiAl family of MPEAs, suggesting that the energy involved does not lead to the nucleation of full dislocations. As mentioned above, Senkov et al. [21] reported the presence of twins.

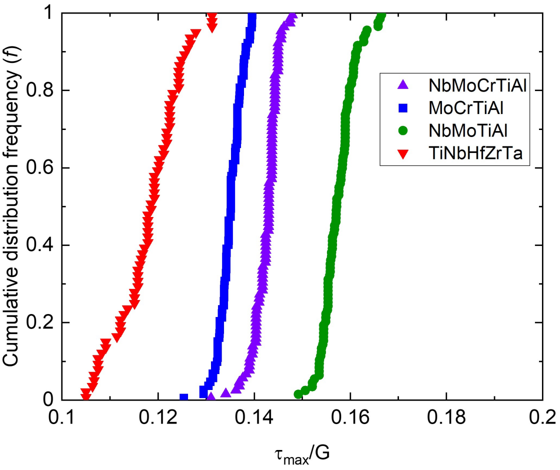

(a)

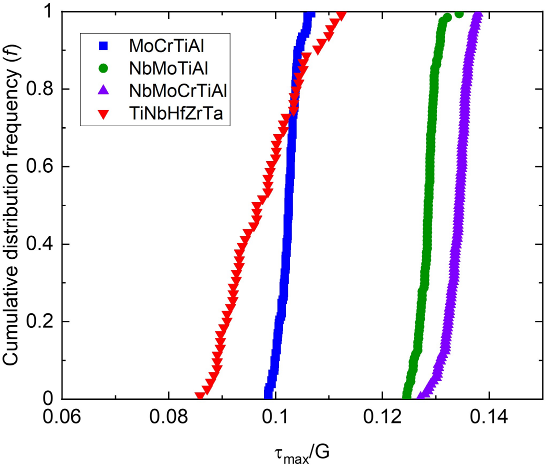

(b)

Figure 3.4.9: The cumulative frequency over τ_{max}/G for (a) 0.01 mNs^{-1} and (b) 0.005 mNs^{-1} shows steep slope for NbMoCrTiAl and its derivatives and the slope steepness reduces for TiNbHfZrTa.

However, Wang et al. [176] reported the presence of deformation twins in TiNbHfZrTa at 77 K along with traces of the HCP phase (ω), but not at room temperature. Chen et al. [177] confirmed the absence of twins in TiNbHfZrTa at room temperature but under deformation, homogenised samples show the presence of deformation bands or kink bands. Kink bands are misorientations along grain boundaries within a crystal with random orientations usually less than the specific twin orientation for the crystal system. Kink bands are usually observed in HCP metals such as Zn, Cd [178] HCP alloys such as Mg-Y-Nd-Zn [179] and certain BCC alloys such as β -Ti alloy [180, 181]. These bands are usually precursors of complete crystal orientation under stress and plasticity at higher strain rates, as observed in TiNbHfZrTa.

The activation volume of TiNbHfZrTa remains unchanged under changing load rates. The change in thermal fluctuation caused by the change in load rate does not affect the dislocation nucleation procedure in this alloy. The fluctuation resulting from the change in the load rate is easily accommodated by generating the accommodation bands like the kink bands, releasing the change in the stress and activating the kink bands to accommodate plasticity. The athermal effect on the activation volume for nucleation can also suggest the activation of pre-existing kinks or accommodation bands in TiHfNbZrTa. The maximum shear stress for this alloy decreases with load rate, suggesting the effect of thermal fluctuation. When comparing the maximum shear stress at pop-in with the theoretical shear stress under different load rates, they are within similar ranges, suggesting the absence of preexisting or pinned dislocations.

3.4.3 Strain rate sensitivity and dislocation motion

The variation of hardness over different strain rates helps to understand the strain rate sensitivity of the materials.

Figures 3.4.10 and 3.4.11 show the logarithmic variation of hardness (H/C) over strain rate (ϵ) for the four samples over four different strain rates. The strain rate sensitivity (m) is thus calculated from the slope of these curves based on the equation 3.1.15 for a hardness averaged over a depth of 1000 to 1600 nm for each alloy. In a similar way, the strain rate sensitivity (m) can also be calculated for each depth of 1000, 1200, 1400 and 1600 nm individually for the varying strain rates for each alloy. This strain rate sensitivity is tabulated in table 3.4.4.

Plastic deformation, as discussed above, is a function of the movement of dislocations. The motions of the dislocations can be quantitatively determined by the volume activated to move the dislocation or the dislocation. The activation volume (V^*) which is strain rate dependent [182, 183] can be easily calculated. The volume required for a dislocation to overcome in order to facilitate the motion is given by this activation volume. The V^* is related to the hardness and the strain rate according to the equations 3.1.17 and 3.4.8.

$$V^* = \sqrt{3}kT(\frac{\mathrm{d}(\ln|\dot{\varepsilon}|)}{\mathrm{d}(H/C)} \tag{3.4.8}$$

To determine the sensitivity of the strain rate, the temperature (T) is also constant, since all experiments are carried out at room temperature (298 K). Based on equation 3.4.8, the slope of hardness over the strain rate (H/C vs $\ln|\dot{\epsilon}|$) of a logarithmic curve as seen in figures 3.4.12 and 3.4.13 is used to determine the activation volume.

Similarly to the strain rate sensitivity calculations, the activation volume is also calculated from hardness averaged over a depth range of 1000 to 1600 nm for each alloy and for particular depths of 1000, 1200, 1400 and 1600 nm for each alloy. The results are tabulated in table 3.4.5 where the volume is expressed in terms of Burgers vector (b) as reported by Chen et al. [23] and Senkov et al. [21]

Depth (nm)	**NbMoCrTiAl**	**NbMoTiAl**	**MoCrTiAl**	**TiNbHfZrTa**
1000	0.06 ± 0.01	0.05 ± 0.01	0.05 ± 0.01	0.03 ± 0.01
1200	0.06 ± 0.01	0.04 ± 0.01	0.05 ± 0.01	0.03 ± 0.01
1400	0.05 ± 0.01	0.04 ± 0.01	0.05 ± 0.01	0.02 ± 0.01
1600	0.05 ± 0.01	0.04 ± 0.01	0.03 ± 0.01	0.02 ± 0.01
Average depth (1000 to 1600nm)	$\mathbf{0.06 \pm 0.01}$	$\mathbf{0.05 \pm 0.01}$	$\mathbf{0.05 \pm 0.01}$	$\mathbf{0.02 \pm 0.01}$

Table 3.4.4: The strain rate sensitivity of NbMoCrTiAl, NbMoTiAl, MoCrTiAl and TiNbHfZrTa over depths of 1000 nm, 1200 nm, 1400 nm, and 1600 nm, and the average over those depths.

The activation volume in the range of 1 to $20b^3$ [184] for a BCC metal or alloy indicates the nucleation of kink pairs and their propagation at room temperature. The MPEAs examined show activation volume in the same range, suggesting kink pair nucleation and propagation. The strain rate dependence of the BCC alloys also indicates the thermally activated nucleation of double kinks in screw dislocation. The MPEAs under observation indicate strain rate dependence suggesting thermally activated double-kink nucleation. It can be further observed from figure 3.4.14a, that m and V^* for dislocation propagation are almost linear over a depth of 1000 to 1600 nm for NbMoCrTiAl. Linearity persists for NbMoTiAl for a depth of 1200 to 1600 nm (Figure 3.4.14b) and for MoCrTiAl for a depth of 1000 to 1400 nm (figure 3.4.15a. However, V^* and m for TiNbHfZrTa increase and decrease, respectively, with increasing depth of indentation (figure 3.4.15b).

Hardness is a function of depth and strain rate, and therefore, as the depth of indentation increases, the hardness reduces. This results in a reduction of the Peierls stress. This leads to a decrease in activation volume and in turn an increase in strain rate sensitivity. This variation is not

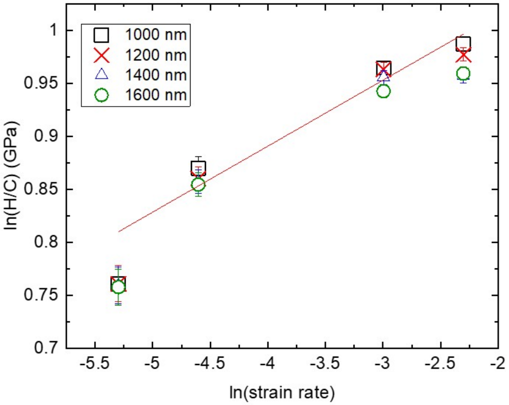

(a) NbMoCrTiAl

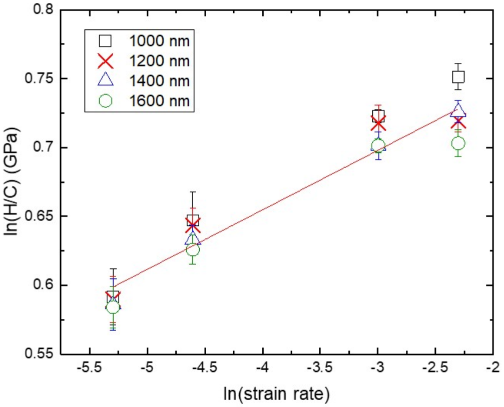

(b) NbMoTiAl

Figure 3.4.10: The logarithmic variation of hardness over strain rate for (a) NbMoCrTiAl and (b) NbMoTiAl show linear correlation. The slope of the linear fit corresponds to m in accordance to equation 3.1.15

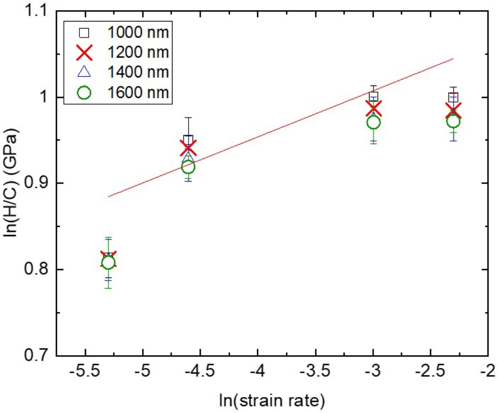

(a) MoCrTiAl

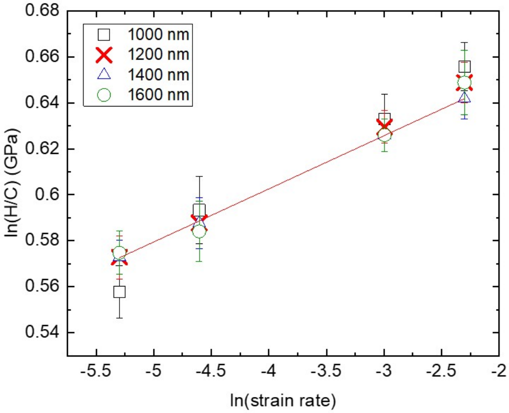

(b) TiNbHfZrTa

Figure 3.4.11: The logarithmic variation of hardness over strain rate for (a) MoCrTiAl and (b) TiNbHfZrTa show linear correlation. The slope of the linear fit corresponds to m in accordance to equation 3.1.15

Depth (nm)	**NbMoCrTiAl**	**NbMoTiAl**	**MoCrTiAl**	**TiNbHfZrTa**
1000	2.30 ± 0.02	3.20 ± 0.02	2.72 ± 0.02	5.49 ± 0.02
1200	2.27 ± 0.01	4.35 ± 0.01	2.51 ± 0.01	6.02 ± 0.01
1400	2.56 ± 0.01	3.98 ± 0.01	2.86 ± 0.01	6.62 ± 0.01
1600	2.54 ± 0.02	4.08 ± 0.02	4.21 ± 0.02	6.44 ± 0.02
Average depth (1000 to 1600nm)	$\mathbf{2.52 \pm 0.02}$	$\mathbf{4.35 \pm 0.02}$	$\mathbf{2.86 \pm 0.02}$	$\mathbf{6.20 \pm 0.02}$

Table 3.4.5: The activation volume (b^3) of NbMoCrTiAl, NbMoTiAl, MoCrTiAl and TiNbHfZrTa over depth of 1000 nm, 1200 nm, 1400 nm, and 1600 nm, and the average over those depths.

observed for the alloys under investigation, suggesting that the hardness, though a function of depth, does not show any changes beyond 1000 nm and therefore do not add additional effect on the activation volume and strain rate sensitivity. However, although as observed previously, the hardness is constant over the depth for TiNbHfZrTa, m and V^* are not constant over the depth.

The strain rate sensitivity of NbMoCrTiAl and its derivatives is comparable but higher than that of TiNbHfZrTa. The activation volume in comparison is lower for NbMoCrTiAl and MoCrTiAl, and increases for NbMoTiAl and TiNbHfZrTa.

Chen et al. [60] have reported that the strain rate sensitivity of NbMoCrTiAl is around 0.018 b^3 under macroscopic compression. The nanoindentation results indicate a slight increase in m of NbMoCrTiAl and its derivatives. Usually, m is observed to be higher when calculated by macroscopic compression than by nanoindentation. It can be understood that, under macroscopic compression, a larger surface area under compression allows dislocations to propagate and annihilate, thus reducing the strain rate sensitivity at a macroscopic level.

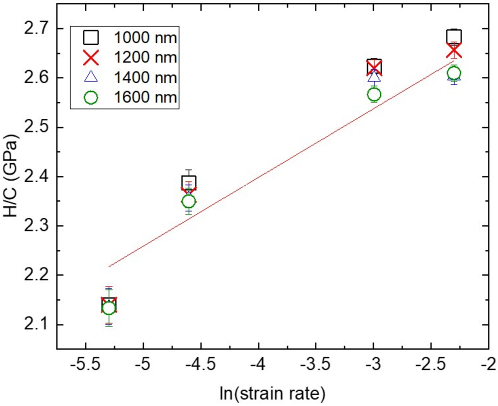

(a) NbMoCrTiAl

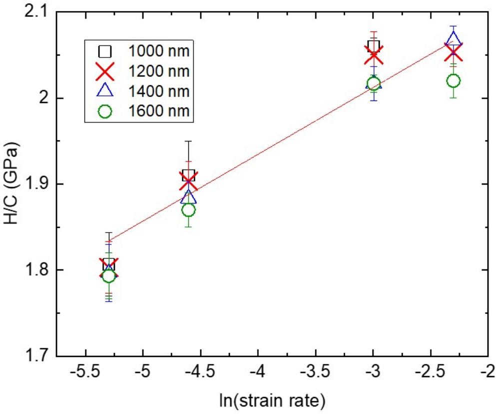

(b) NbMoTiAl

Figure 3.4.12: Hardness over the logarithmic variation of strain rate for (a) NbMoCrTiAl and (b) NbMoTiAl show linear relation. The slope of the linear fit helps in calculation V^* based on the equation 3.4.8

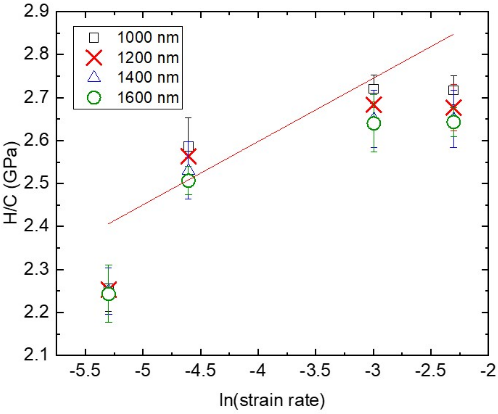

(a) MoCrTiAl

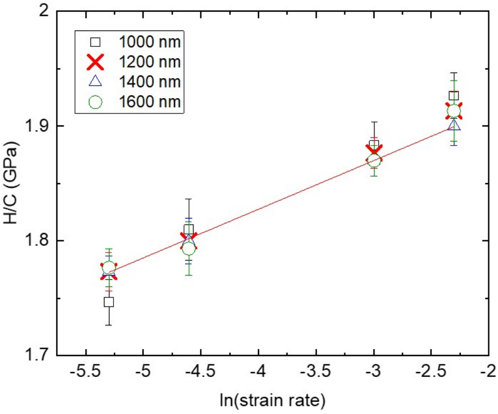

(b) TiNbHfZrTa

Figure 3.4.13: Hardness over the logarithmic variation of strain rate for (a) MoCrTiAl and (b) TiNbHfZrTa show linear relation. The slope of the linear fit helps in calculation V^* based on the equation 3.4.8

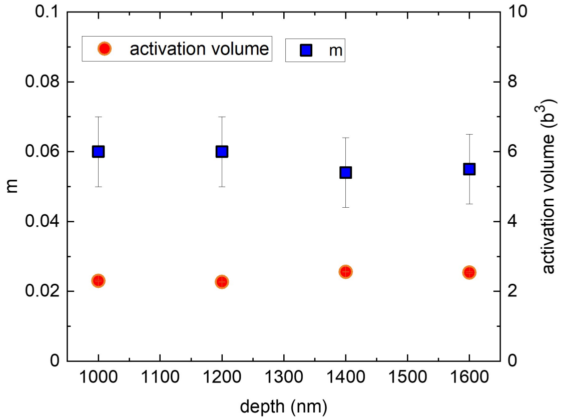

(a) NbMoCrTiAl

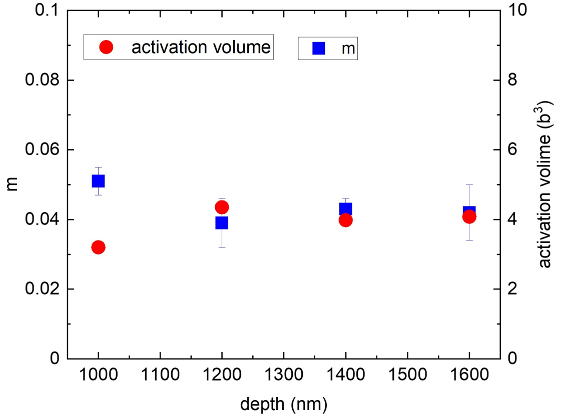

(b) NbMoTiAl

Figure 3.4.14: The strain rate sensitivity (m) and activation volume for varying depths of 1000,1200,1400 and 1600 nm for (a) NbMoCrTiAl and (b) NbMoTiAl remains constant over the depth.

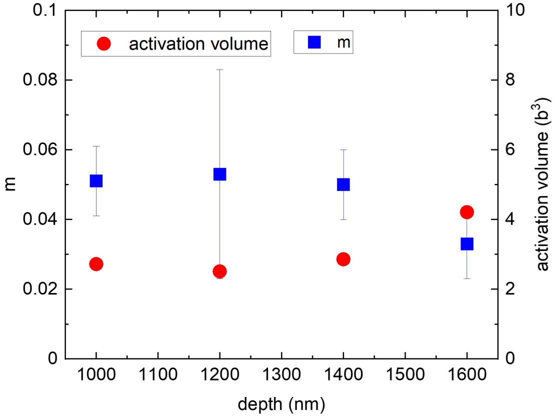

(a) MoCrTiAl

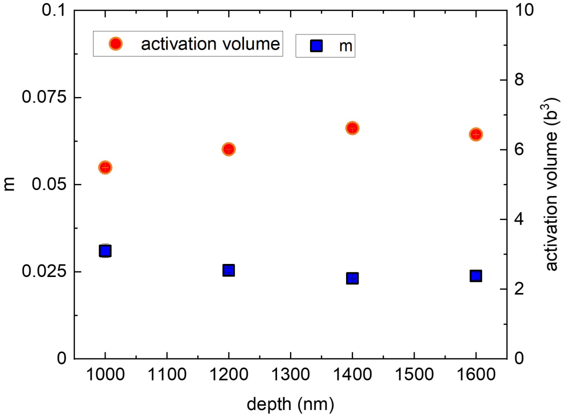

(b) TiNbHfZrTa

Figure 3.4.15: The strain rate sensitivity (m) and activation volume for varying depths of 1000,1200,1400 and 1600 nm for (a) MoCrTiAl remains constant over the depth. However for (b) TiNbHfZrTa the activation volume increases and strain rate sensitivity decreases with depth.

The above calculations are obtained when tested at different strain rates. Under constant strain-rate nanoindentation, in order to obtain a stable hardness, the indentation has to be drilled to a deeper depth for lower strain rates. Along with the thermal drift, the calculated hardness response is usually higher for a lower strain rate, thus resulting in a higher strain-rate sensitivity. In addition, for small areas of indentation under constant strain, the dislocations generated are more entangled in a smaller area, responding to a higher strain rate sensitivity [143]. Therefore, it is usual to observe a higher strain rate sensitivity as a depth of 1000 or 1200 nm compared to 1600 nm.

The m is the lowest for TiNbHfZrTa among the investigated alloys. As mentioned in section 3.4.2, the plasticity in TiNbHfZrTa sets in by nucleation of kink bands or accommodation bands. Kink bands are easy predecessors of kink pairs in screw dislocation and require low Peierls stress for dislocation motion. Therefore, the mobility of the dislocation increases, which in turn reduces the sensitivity to change strain rates for this alloy. This is similar to FCC alloys and metals, which exhibit high ductility at room temperature [47]. As FCC alloys and metals have a low Peierls stress barrier and no thermal activation involved, they usually have little or no sensitivity to the strain rate [142, 143, 185].

TiNbHfZrTa has been reported to exhibit pencil glide similar to most BCC metals and alloys [164]. This indicates the fact that TiNbHfZrTa undergoes plastic deformation by nucleation of the kink pair of screw dislocations like most BCC systems. The nucleation of the accommodation bands in TiNbHfZrTa not only allows easier kink pair nucleation and propagation but also increases the dislocation density in the vicinity. This results in a larger volume of dislocations tangling, and thus a large activation volume is involved. The easier nucleation of the kink bands or accommodation bands results in a higher activation volume to overcome the dislocations during motion. Together, the two mechanisms aid in the ductility of TiNbHfZrTa.

The activation volume for dislocation propagation, similar to the strain rate sensitivity, is affected by the strain rate and the depth of indentation (Figure 3.4.15b). As the sensitivity to the strain rate decreases, the obstacle to overcome by the dislocations increases. Therefore, most FCC systems have to overcome an activation volume larger than $10b^3$, and sometimes as large as 100 to $1000b^3$, indicating the involvement of a forest of dislocations [47]. In addition, the microstructure also influences the activation volume [186]. As the grain size increases, the dislocation annihilation reduces and more entanglement is observed. This is commonly observed in alloys of multiprincipal FCC elements such as FeCoCrMnNi [187] at room temperature and lower temperature. The strain rate sensitivity of TiNbHfZrTa is as low as 0.01, as expected in any FCC system.

The strain rate dependence of the systems under investigation is comparable to the chromium [158] which was reported to be 0.03 ± 0.007. However, Choi et al.[158] also reported that the activation volume for kink pair nucleation and propagation for chromium is as high as $19b^3$ with $\overrightarrow{b} = 2.5\,\text{nm}$. In accordance with the range defined for supporting the theory of thermally activated kink pair nucleation of screw dislocation, chromium exhibits a much higher activation volume in comparison to the alloys in question. However, TiNbHfZrTa shows an activation volume comparable to that of W and Mo [130].

The activation volume calculated for NbMoCrTiAl and MoCrTiAl is smaller than that for NbMoTiAl, despite the fact that all three alloys undergo a dislocation nucleation and propagation mechanism. This can be attributed to the low hardness exhibited by NbMoTiAl as discussed in Section 3.4.1. The hardness of the system is reduced because of the absence of Cr in the system. As reported by Chen et al. [60] for the macroscopic compression tests, the nanoindentation also shows that the change in Cr and Nb contained does not alter the strain rate sensitivity. However, the activation volume increases because of the absence of Cr in the system. The absence of Cr in the systems modifies the effect of lattice mismatch on solid solution strengthening as discussed in section 3.4.1. It can be argued that a modified lattice for NbMoTiAl, in comparison to that for NbMoCrTiAl and MoCrTiAl, increases the entanglement of the dislocations slightly more than in NbMoCrTiAl and MoCrTiAl and results in a higher activation volume in the former alloy than in the latter alloys.

As discussed earlier, the complex non-planar core of the screw dislocation governs the plasticity in the BCC alloys, and the mobility of the screw dislocations is a function of the strain rate and temperature. The strain rate sensitivity at room temperature can help identify if the alloys are in line tension or the elastic interaction zone of the transition theory of double kink propagation of screw dislocation [58]. In that paper Seeger et al. concluded that at lower temperature or equivalent higher stress, a BCC system is highly strain rate sensitive (section 1.3.3), thus mostly falls within the line tension regime. This sensitivity reduces as the temperature increases and the system moves into the elastic interaction zone.

Seeger et al. [48] mathematically defined the line tension and the elastic interaction zone as, respectively,

$$H = H_k + B[1 - \sqrt{\frac{T}{T_k}}] \tag{3.4.9}$$

$$H = H_k + A[1 - \left(\frac{T}{T_k}\right)^2] \tag{3.4.10}$$

In equations 3.4.9 and 3.4.10, H_k is the hardness at the temperature of the knee. This is the athermal hardness of the material, which is not a function of temperature or Peierls stress. T_k or the knee temperature is the temperature beyond which the hardness reaches a plateau and does not vary with temperature. B ($3\sqrt{3}\tau_B$) and A are the constants consisting of the thermal and athermal stress function, respectively.

Chen et al. [60] have speculated, based on micro and nanohardness, that the temperature at which the hardness plateaus is 573 K or above for NbMoCrTiAl and its alloy derivatives. Although exact T_k is not determined for the alloys, based on the strain rate sensitivity calculation of Chen et al. [60], NbMoCrTiAl shows T_k around 573 K. Figure 3.4.16a shows the line tension equation that fits the curves considering that T_k is 573 K. The H_k is 5.4 GPa and shear τ_B is 1.98 GPa as obtained from the intercept and slope from figure 3.4.16a respectively.

A similar calculation can be obtained for NbMoTiAl and MoCrTiAl, considering that T_k for NbMoTiAl and MoCrTiAl is 573 K and 673 K, as the line tension equation fits the curves (figures 3.4.16b and 3.4.17). The H_k and τ_B for these alloys are tabulated in table 3.4.6. For NbMoTiAl, beyond 573 K, the hardness appears to be a plateau, as seen in figure 3.4.18b. Since the maximum temperature of the experiment was 673K, such a plateau cannot be observed for MoCrTiAl. However, the line tension equation fits the data in figure 3.4.17 b, considering that 673 is T_k. It is true that a more detailed observation of the hardness over a larger temperature range can help determine T_k, subsequently H_k, and the athermal and thermal shear stress involved using equations 3.4.9 and 3.4.10 more accurately.

Schoeck [188] suggested the hardness as a function temperature, by thermodynamics, is related to the activation barrier Q :

$$Q = -T[kT\frac{\mathrm{d}\ln|\dot{\varepsilon}|}{\mathrm{d}\sigma}]\frac{\mathrm{d}\sigma}{dT} = -T\frac{V^*}{\sqrt{3}}\frac{d\ln|H/C|}{dT} \qquad (3.4.11)$$

by equation 3.4.11. In this Arrhenius-type equation, C is the Tabor factor and V_m^* is the activation volume for the propagation of the dislocation at temperature T. As the

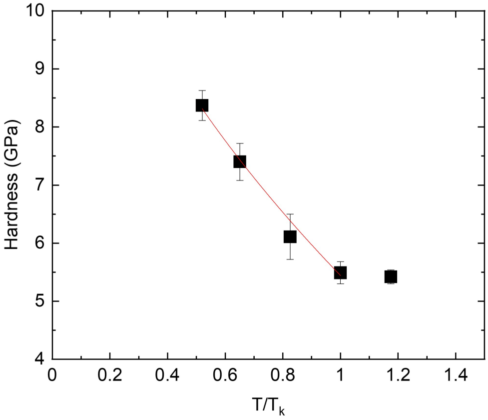

(a) NbMoCrTiAl

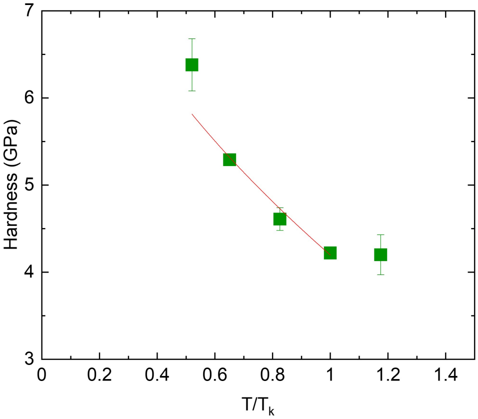

(b) NbMoTiAl

Figure 3.4.16: The line tension equation fits the temperature-dependent hardness for (a) NbMoCrTiAl, (b) NbMoTiAl. The temperature expressed as normalized over the knee temperature.

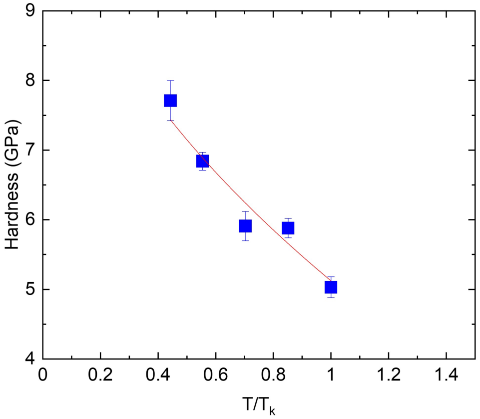

(a) MoCrTiAl

Figure 3.4.17: The line tension equation fits the temperature-dependent hardness for (a) MoCrTiAl. The temperature expressed as normalized over the knee temperature.

underlying deformation mechanism for the alloys is identified at room temperature, the energy barrier corresponding to the activation volume at room temperature can be easily determined.The temperature-dependent activation energy for NbMoCrTiAl and its derivatives at room temperature are tabulated in table 3.4.6 (and figures 3.4.18 and 3.4.19).

Samples	**T_k** (**K**)	**H_k** (**GPa**)	**τ_B** (**GPa**)	**Q** (**eV**)
NbMoCrTiAl	573	5.44 ± 0.02	1.98 ± 0.03	0.133 ± 0.005
MoCrTiAl	573	4.19 ± 0.04	1.11 ± 0.03	0.251 ± 0.005
NbMoTiAl	≥ 673	5.89 ± 0.03	1.65 ± 0.03	0.130 ± 0.005

Table 3.4.6: The knee temperature, knee hardness, athermal shear stress and activation energy of NbMoCrTiAl and its derivatives.

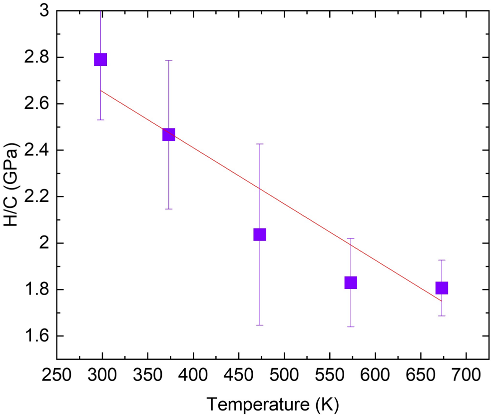

(a) NbMoCrTiAl

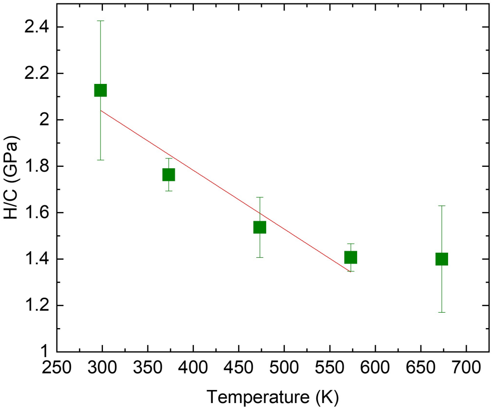

(b) NbMoTiAl

Figure 3.4.18: The hardness of (a) NbMoCrTiAl, (b) NbMoTiAl shows a linear dependence on temperature. The hardness is calculated as H/C with C being the Tabor factor. A plateau is observed at 573K for NbMoCrTiAl and NbMoTiAl.

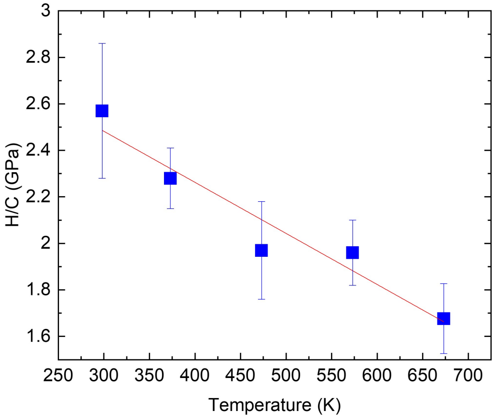

(a) MoCrTiAl

Figure 3.4.19: The hardness of (a) MoCrTiAl shows a linear dependence on temperature. The hardness is calculated as H/C with C being the Tabor factor. No plateau is observed until 673K for MoCrTiAl.

The activation energy calculated (table 3.4.6 is lesser than that of chromium: 0.35 ± 0.04 eV [158]. This is because in chromium, the obstacle increases because of the presence of impurities, which are absent in the alloys under examination. The Gibbs free energy calculation further confirms that the rate-determining mechanism for these alloys is double kink nucleation [189]. It has been observed that for BCC MPEAs that range of 0.1to0.4 eV is usual. However, the higher the value in this range, suggests multiple kinks, cross-kink, and detrapping resulting in more pinned dislocations and therefore require a higher activation energy [190]. The energy expenditure Q is observed to be lower for NbMoCrTiAl and NbMoTiAl compared to MoCrTiAl (table 3.4.6). Since previously reported, MoCrTiAl exhibits similar hardness, strain rate sensitivity, and activation volume for dislocation nucleation and propagation, and the reason for the higher activation energy for kink propagation at room temperature cannot easily be concluded.

3.5 Conclusion

The purpose of this work was to understand the mechanical stability of refractory MPEAs such as NbMoCrTiAl, NbMoTiAl, and MoCrTiAl, which are reported to be brittle at room temperature with the crystal structure of B2 [23]. These alloys were compared with the popularly known refractory MPEA, TiNbHfZrTa, which is known to be ductile at room temperature. Nanoindentation was the experimental method chosen to compare the two types of refractory MPEAs to understand plastic deformation, especially on a nanoscale. The plastic deformation mechanism is understood by understanding the nucleation and motion of the dislocation and their related mechanisms.

Nanoindentation in NbMoCrTiAl and its family of alloys did not show pile-up or sink-in but slipped traces around the indent. This suggested the ductile nature of the alloys on the nano- and micro-scale. However, the possibility of porosity and large stresses at grain boundaries due to large grains can explain the brittleness at room temperature as observed under macroscopic mechanical testing [23]. The theoretical shear stresses are comparable to each other with a slight increase for the system without Nb. These are in contrast to TiNbHfZrTa, which shows very low nanohardness and modulus at room temperature under nanoindentation.

The temperature range in the discussion does not include the temperature for the order-disorder transition as reported by Chen et al. [60] and thus its effect on the change in modulus and hardness could not be observed. The alloys adhere to the generally accepted deformation mechanism in BCC, which is thermally activated dislocation slip. The Seeger model [58] can explain the change in hardness with temperature, as observed here. At room temperature, the alloys are in the low temperature regime, and thus the dislocation motion is expected to be dominated by kink-pair motion and are thermally dependent. The increase in Cr and the absence of Nb in the system help in strengthening and overcome the thermal effect on the dislocation motion and strengthening.

This leads to understanding the solid solution hardening of the system using the classical Labusch [163] and Fleischer model of a binary solid solution [162]. The paraelastic effect of the lattice distortion on the solid solution strengthening can explain the strengthening of NbMoCrTiAl and its family of MPEAs using both Labusch's binary alloys [163] and Vervenne's approach for the FCC high entropy alloy [165]. However, no correlation could be achieved for the strengthening of the solid dieleastic solution, which is due to the shear modulus mismatch [191]. In contrast, the solid solution strengthening of TiNbHfZrTa can be well explained by the classical solid solution strengthening of binary system models [14].

The onset of plasticity was investigated by nanoindentation on a defect-free surface at a very low indentation depth. The load displacement curve showed a sudden jump in displacement in the sample, popularly known as pop-in. This occurs as the maximum shear stress approaches the theoretical shear stress. The pop-in corresponds to the point of dislocation nucleation on a defect-free surface. The activation volume of dislocation nucleation for NbMoCrTiAl and its derivatives were calculated to be $\sim 1b^3$, similar to BCC metals such as Mo and high-entropy alloys such as BCC TiZrNbTa, suggesting heterogeneous nucleation through atom-vacancy exchange. It is a thermally assisted process that is required for heterogeneous nucleation of a full dislocation.

In contrast, TiNbHfZrTa exhibits a lower activation volume than $1b^3$ and does not exhibit a load-rate dependence. In TiNbHfZrTa, the local chemistry of neighbouring atoms reduces the fault energy that initiates accommodation or kink bands. This effect is observed in FCC systems, where the onset of plasticity is by nucleation of partials. This led to the conclusion of accommodation bands and kink bands in TiNbHfZrTa. These bands do not require the generation of full dislocations and thus aid the nucleation process. Therefore, the energy required for dislocation nucleation is lower for TiNbHfZrTa than for NbMoCrTiAl and its family of alloys. This allows for easy onset of plasticity for TiNbHfZrTa.

Like most BCC elements and alloys, the dislocation propagation in NbMoCrTiAl and its derivatives in order to allow plasticity is aided by double-kink nucleation and propagation for complex cored screw dislocations. The dislocation propagation is thermally assisted like most BCC systems and is therefore, strain rate sensitive. Calculating the volume and energy of the activation also suggests the formation and propagation of a kink pair. TiNbHfZrTa, although it has accommodation bands and kink bands, also exhibits strain rate sensitivity. The activation volume calculations for TiNbHfZrTa clarified that the dislocation propagation mechanism is similar to that of kink-pair nucleation and propagation. However, in the presence of accommodation bands, the activation volume required for dislocation propagation to overcome the obstruction to move is higher than that of NbMoCrTiAl and its derivatives.

On the basis of the observations mentioned above, it can be concluded that NbMoCrTiAl and its family of alloys nucleate dislocation by atom-vacancy exchange and propagate these dislocations by kink pair motion. This is commonly observed in BCC crystal systems. Considering that hardness is a function of temperature and strain rate, the rate-determining mechanism for dislocation propagation for NbMoCrTiAl and its derivatives at room temperature is concluded to be a line tension model where the knee temperature is 573 K or higher.

In contrast, nucleation of accommodation bands and kink bands requires a lesser energy than full dislocations. This results in an easier and earlier onset of plasticity in TiNbHfZrTa. This supports the ductility of this alloy at room temperature. Furthermore, the dislocation propagation method for this MPEA is similar to kink pair motion. The easily nucleated accommodation bands and kink bands result in crowding and increasing the activation volume required for dislocation propagation for plastic deformation. This mechanism makes the alloy ductile and tougher at room temperature in comparison to NbMoCrTiAl and its family of alloys.

Because dislocation nucleation and propagation were not tested at elevated temperature, the effect of ordering in NbMoCrTiAl alloys could be fully compared and understood. Thus, the brittleness of NbMoCrTiAl and its family of alloys at room temperature due to ordered phase B2 is beyond the scope of this work.

Chapter 4

Summary

"When I examine myself and my methods of thought, I come to the conclusion that the gift of fantasy has meant more to me than any talent for abstract, positive knowledge"

Albert Einstein

Multi principal elements alloys (MPEAs)—also commonly known as high entropy alloys (HEAs)—have been the centre of intense research over the past decade. The use of five or more elements to form a single-phase solid solution opens a range of possibilities to design various alloy combinations, as well as engineer desired properties. The MPEAs can be obtained in standard crystal systems such as FCC, BCC or as multiphase material. The understanding of the stability of these alloys is intriguing, as the chemistry and elemental interactions make the thermodynamic and mechanical properties more complex. In order to understand these novel material systems, the stability of such alloys is critical and represents the central topic of this work. We approach this topic from two different directions and categorise the term “stability” as thermodynamic stability and mechanical stability. Both were addressed using different methods of simulation and experiments, as summarised in the following.

This dissertation tries to answer the questions posed as motivation in section 1.4 to help understand the stability of refractory BCC MPEAs in the context of thermodynamics and mechanical properties.

1. The simplistic model of correlating Potts model to multi-principal elements alloys using Monte Carlo simulations helped in concluding the effect of entropy on the order-disorder phase stability of the alloys. The lower coordination number suppresses the stability of the ordered state. Besides the coordination number, focusing on the three-dimensional BCC structure helped us understand the effect of increasing the element in a system. The model proposes that the increase in the number of elements increases only the configurational entropy. This increase reflects that the order-disorder transition is a function of configurational entropy. The increasing elements in the system lower the order-disorder transition temperature allowing random solid solutions easily achievable. However, keeping out the effect of enthalpy, the increase in the element of the systems the energy of the system. This is due to the interaction of

the atoms with the dissimilar atoms and as the number of elements in the system increases, the probability of this interaction increases. Thus, entropy independently affects the stability of a random solid solution.

2. A systematic study by nanoindentation on a BCC and a B2 structured refractory multi-principal elements alloys, former exhibiting ductility and the latter exhibiting brittleness at room temperature, shows the relation between mechanical properties and solid solution strengthening. NbMoCrTiAl and its two variations NbMoTiAl and MoCrTiAl exhibited an increase in mechanical properties like elastic modulus, hardness, and maximum theatrical shear stress with reducing Nb content. On the contrary ductile BCC refractory alloy, TiNbHfZrTa exhibited lower mechanical properties than NbMoCrTiAl and its families. Correlating the mechanical properties and the solid solution strengthening, lattice mismatch helped us understand the phenomena more than the shear mismatch in the systems. The varied elements with varying atomic sizes in the system interact to complicate the understanding of lattice mismatch and thus the solid solution strengthening. Some alloys like TiNbHfZrTa which have elements of primarily two ranges of atomic sizes can explain the mechanical properties like a binary solid solution. However, for alloys like NbMoCrTiAl whose elements do not categorize into two atomic radii ranges, helps in modifying the mechanical properties based on a more complicated solid solution where every element in the solute is the solution of all the elements together.

3. The increased number of elements in the system influence the mechanical properties and can influence the properties at elevated temperature. Though the work does not directly study the effect of temperature change in all properties, the thermal effect on the mechanical properties is studied. The temperature-dependent mechanical properties like hardness or elastic modulus, of NbMoCrTiAl and its derivative, are studied. These alloys respond to the thermal dependence of the mechanical properties simi-

lar to other BCC elements like molybdenum, tungsten or chromium. This is further validated by understanding the dislocation nucleation process.

4. The activation volume required by the dislocation to overcome in order to generate new dislocations for the B2 system is similar to other BCC metals and alloys exhibiting pencil glide by atom vacancy exchange. The thermally assisted stress-initiated activation process holds true for these systems. This process is also true for TiNbHfZrTa; however, the activation volume indicates a lack of load rate dependence. This discrepancy pointed to the fact that TiNbHfZrTa do not nucleate full dislocation but partial dislocation to generate accommodation bands or activation on other non-thermal dislocations nucleation like activation of edge dislocations. The dislocation propagation, on the other hand, proved that all the alloys under investigation at room temperature are aided by double kink nucleation and propagation of three-dimensional complex cored screw dislocations. The involved activation volume is slightly more for TiNbHfZrTa than the NbMoCrTiAl alloys indicating the presence of closely spaced dislocations similar to a small forest of dislocations in the former alloy. The constituent elements of these alloys are mostly BCC, however a typical BCC alloy behaves differently than a known BCC metal , whereas B2 structured alloy exhibits standard dislocation nucleation and motion phenomena as observed in other BCC metals and alloys. This impact on the deformation behaviour of MPEAs can be attributed to the cocktail effect.

In this work, all the questions that have been posed in understanding the thermodynamic and mechanical stability of the alloys are not fully explored. However, on the basis of the classically defined parameters of the high-entropy alloys or the multi-principal element alloys, the understanding of mechanical properties was attempted. The work also focused on understanding the difference in the mechanical stability of ductile and brittle BCC refractory multi-principal element alloys. It answers the difference in dislocation nucleation and motion of these alloys. However, thermodynamic stability is answered with a more simplistic approach to these complex alloys.

However, in order to obtain a more detailed understanding of the stability of these alloys, extended work is continued and proposed. An effect of entropy can be further elucidated on a more closed system using Kawasaki dynamics. However, mechanical properties are studied as a function of temperature and microstructure and grain boundaries for NbMoCrTiAl [192] and for other alloys required to be studied. This will help to obtain a more detailed understanding of the alloys and the relationship between the mechanical response to the microstructure and subsequently the alloy compositions.

Appendix A

“Contemporary science is based on the philosophy of materialism, which claims that all reality is material or physical”

Rupert Sheldrake

A.1 Bragg-Williams theory

The regular solution defined in this thesis is best understood by the Bragg-Williams theory, which defines the ordering and disordering in the system. In a crystal lattice, the lattice sites are occupied by the alloying elements, and the interaction between the neighbouring atoms defines the equilibrium of the system and the ordering in the system. According to Bragg and Williams [82], a system in a completely disordered state is one in which any atom can occupy any site in the lattice leading to a single-phase state of the alloy. In an ordered state, atoms of a particular element segregate on particular lattice sites, leading to an orderly arrangement in the lattice. If this ordering is over the entire lattice structure, it leads to a long-range ordering usually seen in the intermetallic.

However, if this ordering is restricted to a certain part of the total alloy system in the lattice, it leads to short-range ordering. As an alloy is a dynamic system, the lowest energy among the ordered and disordered systems motivates the phase formation in the alloy. Usually, a disordered arrangement has more potential energy than an ordered arrangement, and thus segregation is a more stable state unless the complete randomly arranged system has the lowest total free energy of the alloy system due to the interaction parameters and the entropy of the system. It should be noted that since the system follows the free-energy equation, a higher temperature always leads to disorders in the system. Thermal agitation aids the atoms in occupying any site in the lattice. Thus, for a fixed composition in an alloy, it is expected that segregation is in the lower temperature, and beyond a fixed temperature the system is completely disordered. According to Braggs and Williams [82], this fixed temperature, also known as the critical temperature is related to the ordering parameter. Beyond the critical temperature, the ordering parameter is 0 when the system is completely disordered. This shows an analogy to ferromagnetism, and the critical temperature for order-disorder transition is analogous to Curie temperature.

A.2 Weibull distribution and comparison to weakest link approach

In 1951, Wallodi Weibull [126] described a continuous probability distribution which came to be termed a Weibull distribution and is used for understanding various statistical distributions like particle distributions and brittle fracture probability. The probability density function is given as

$$f(x;k,\gamma) = \begin{cases} \frac{k}{\gamma}(\frac{x}{\gamma})^{k-1}\exp(\frac{-x}{\gamma})^{k} & x \geq 0 \\ 0 & x < 0 \end{cases} \tag{A.2.1}$$

Here k is the shape factor and γ is the scale factor. The distribution gives the rate of failure of an event as the power of time. For n maximum number of total occurrences, the probability of an event or failure of the event x can be given as $P^n(x) = P(a_n x + b)$, as x tends to 0, the probability of the occurrence or failure (P) can tend to 0 or 1.

For a random event x, if the probability of the occurrence of a failure is $P(x)$, the probability of survival is $1 - P(x)$. Thus, for n events that occur simultaneously, the probability of survival can be written as $1 - P(x)^n$. The distribution function can be expressed as an exponential function (Poisson distribution) of the following.

$$P(n) = 1 - \exp(-n\varphi(x)) \tag{A.2.2}$$

The Weibull cumulative distribution function is expressed as

$$P(t) = F(t) = \frac{kt^{k-1}}{\gamma^k}\exp(\frac{-t^k}{k}) \qquad t > 0 \tag{A.2.3}$$

as the rate of occurrence or failure is a function of time involving the shape and scale factor as described earlier. These factors can be used to determine various insightful data, especially by simplifying the equation.

$$\ln|-\ln|1-F(t)|| = k\ln|t| - \ln|\gamma^t|| \tag{A.2.4}$$

The complicated equation is then reduced to a linear representation that allows easy calculation of the shape factor and the scale factor of the slope and the intercept. The Weibull distribution and analysis of the shape factor and scale factor are popular in understanding the brittle nature of materials as a part of the weakest link approach.

The weakest link approach analyses the required flaw size for a material, statistically analysing samples with a random number of flaws with varying flaw sizes. If the mean number of critical flaw size is m, the probability of surviving the failure from the flaw is

$$P(f) = 1 - \exp[-\frac{V_{ef}}{V_o}\left(\frac{\sigma^*}{\sigma_o}\right)^m] \tag{A.2.5}$$

The governing factors of failure from flaws are factors: the effective volume (V_{ef}) indicating the geometry of the sample and the stress (σ^*) involved that indicates the dependence on the stress. The probability of the mean number of critical flaws leading to failure in the component when calculated over the complete volume of the sample in question can be written as

$$P(f) = 1 - \exp[-\frac{\sigma^{*\,m}}{b}] \tag{A.2.6}$$

Where the dependent factors can be simply expressed as σ^* indicating the stress dependence and b indicating the geometry dependence and m is a frequency parameter. The result can be linearly expanded as equation A.2.4 identifies the geometric parameter b from the intercept and the frequency parameter m from the slope. Understanding the weakest link approach and the Weibull distribution is helpful in understanding the dislocation nucleation probability distribution and its correlation to the Weibull distribution. The dislocation nucleation involves factors similar to the weakest link approach, namely, the enthalpy of the activation and the stress-activated and thermally assisted factors. The frequency or probability of the dislocation to nucleate in every indentation is

$$F(\tau) = 1 - \exp[\frac{-\eta kT}{V(\dot{\tau})} \exp[\frac{\tau V}{kT}]] \tag{A.2.7}$$

This equation is similar to equation A.2.3, and when expanding the probability of nucleation linearly, equation A.2.4 is simplified to

$$\ln|-\ln|1 - F(\tau)|| = \frac{V}{kT}\tau - \ln|\frac{\eta kT}{V(\tau)}| \tag{A.2.8}$$

The cumulative distribution of the pop-in or the rate of the dislocation nucleation is a function of time and, eventually, that of the shear stress involved in the nucleation of the dislocation, follows an exponential function similar to equation A.2.2.

The cumulative distributions for the theory of dislocation nucleation are similar to those of the weakest link, where the governing factors are exponentially related to the distribution, making the Weibull distribution the most appropriate cumulative distribution fitting and allowing easy accessing of important data as the Weibull parameters coincides with the factors that determine the processes. The shape factor in the Weibull distribution is equivalent to the geometrical factor in the weakest link approach. It can be correlated with kT/V in the nucleation equation where V is the activation energy involved for the nucleation of the dislocation to occur.

The discussion rises with the scale factor in the cumulative distribution and its significance if any in the above-discussed processes.

A.3 Atomic radius and shear modulus

Elements	**Atomic radii (Å)**	**Shear Modulus (GPa)**
Mo	1.36	126
Cr	1.24	115
Al	1.43	26
Nb	1.42	105
Ti	1.44	44
Ta	1.43	69
Zr	1.60	33
Hf	1.57	30

Table 3.4.1: Atomic radius and shear modulus of pure elements that comprise the MPEAs under investigation [193, 194]

List of Abbreviations

2D	2-dimensional
3D	3-dimensional
BCC	Body-centered cubic
CCA	Compositional complex alloy
CDF	Cumulative distribution frequency
CSM	Continuous stiffness measurement
DCM	Dynamic contact module
DFT	Density function theory
FCC	Face-centered cubic
GND	Geometrically necessary dislocation
HCP	Hexagonal close-packed
HEA	High entropy alloy
ISE	Indentation size effect
KMC	Kinetic Monte Carlo
LSCM	Laser scanning confocal microscope
MCRG	Monte Carlo renormalization group
MCU	Monte Carlo unit
MC	Monte Carlo

μH	Microhardness
MPEA	Multi principle elements alloy
nH	Nanohardness
OPS	Oxide polishing suspension
rKMC	Rejection kinetic Monte Carlo
SEM	Scanning electron microscope
SPPARKS	Stochastic parallel particle kinetic simulator
SSD	Statistically stored dislocation
XRD	X-ray diffraction

List of Figures

List of Tables

Bibliography

[1] B. Cantor, I. Chang, P. Knight, A. Vincent, Microstructural development in equiatomic multicomponent alloys, Materials Science and Engineering: A 375–377 (2004) 213–218. `doi:10.1016/j.msea.2003.10.257`.

[2] H. M. Daoud, A. M. Manzoni, N. Wanderka, U. Glatzel, High-temperature tensile strength of $Al_{10}Co_{25}Cr_8Fe_{15}Ni_{36}Ti_6$ compositionally complex alloy (high-entropy alloy), JOM 67 (10) (2015) 2271–2277. `doi:10.1007/s11837-015-1484-7`.

[3] J.-W. Yeh, S.-J. Lin, T.-S. Chin, J.-Y. Gan, S.-K. Chen, T.-T. Shun, C.-H. Tsau, S.-Y. Chou, Formation of simple crystal structures in Cu-Co-Ni-Cr-Al-Fe-Ti-V alloys with multiprincipal metallic elements, Metallurgical and Materials Transactions A 35 (8) (2004) 2533–2536. `doi:10.1007/s11661-006-0234-4`.

[4] D. Miracle, O. Senkov, A critical review of high entropy alloys and related concepts, Acta Materialia 122 (2017) 448–511. `doi:10.1016/j.actamat.2016.08.081`.

[5] O. N. Senkov, D. B. Miracle, K. J. Chaput, J.-P. Couzinie, Development and exploration of refractory high entropy alloys – A review, Journal of Materials

Research 33 (19) (2018) 3092–3128. `doi:10.1557/jmr.2018.153`.

[6] E. George, W. Curtin, C. Tasan, High entropy alloys: A focused review of mechanical properties and deformation mechanisms, Acta Materialia 188 (2020) 435–474. `doi:10.1016/j.actamat.2019.12.015`.

[7] E. P. George, D. Raabe, R. O. Ritchie, High-entropy alloys, Nature Reviews Materials 4 (8) (2019) 515–534. `doi:10.1038/s41578-019-0121-4`.

[8] M.-H. Tsai, J.-W. Yeh, High-entropy alloys: A critical review, Materials Research Letters 2 (3) (2014) 107–123. `doi:10.1080/21663831.2014.912690`.

[9] F. Tian, A review of solid-solution models of high-entropy alloys based on ab initio calculations, Frontiers in Materials 4 (2017). `doi:10.3389/fmats.2017.00036`.

[10] B. Gludovatz, A. Hohenwarter, D. Catoor, E. H. Chang, E. P. George, R. O. Ritchie, A fracture-resistant high-entropy alloy for cryogenic applications, Science 345 (6201) (2014) 1153–1158. `doi:10.1126/science.1254581`.

[11] Z. Zhang, M. M. Mao, J. Wang, B. Gludovatz, Z. Zhang, S. X. Mao, E. P. George, Q. Yu, R. O. Ritchie, Nanoscale origins of the damage tolerance of the high-entropy alloy CrMnFeCoNi, Nature Communications 6 (1) (2015) 1–6. `doi:10.1038/ncomms10143`.

[12] O. Schneeweiss, M. Friák, M. Dudová, D. Holec, M. Šob, D. Kriegner, V. Holý, P. Beran, E. P. George, J. Neugebauer, A. Dlouhý, Magnetic properties of the CrMnFeCoNi high-entropy alloy, Physical Review B 96 (1) (2017) 014437. `doi:10.1103/physrevb.96.014437`.

[13] J.-H. Pi, Y. Pan, L. Zhang, H. Zhang, Microstructure and property of AlTiCrFeNiCu high-entropy alloy,

Journal of Alloys and Compounds 509 (18) (2011) 5641–5645. `doi:10.1016/j.jallcom.2011.02.108`.

[14] O. N. Senkov, J. M. Scott, S. V. Senkova, F. Meisenkothen, D. B. Miracle, C. F. Woodward, Microstructure and elevated temperature properties of a refractory TaNbHfZrTi alloy, Journal of Materials Science 47 (9) (2012) 4062–4074. `doi:10.1007/s10853-012-6260-2`.

[15] J. W. Qiao, M. L. Bao, Y. J. Zhao, H. J. Yang, Y. C. Wu, Y. Zhang, J. A. Hawk, M. C. Gao, Rare-earth high entropy alloys with hexagonal close-packed structure, Journal of Applied Physics 124 (19) (2018) 195101. `doi:10.1063/1.5051514`.

[16] J. Li, Diffusive origins, Nature Materials 14 (7) (2015) 656–657. `doi:10.1038/nmat4326`.

[17] Y. H. Jo, S. Jung, W. M. Choi, S. S. Sohn, H. S. Kim, B. J. Lee, N. J. Kim, S. Lee, Cryogenic strength improvement by utilizing room-temperature deformation twinning in a partially recrystallized vcrmnfeconi high-entropy alloy, Nature Communications 8 (1) (2017) 1–8. `doi:10.1038/ncomms15719`.

[18] C.-J. Tong, M.-R. Chen, J.-W. Yeh, S.-J. Lin, S.-K. Chen, T.-T. Shun, S.-Y. Chang, Mechanical performance of the AlxCoCrCuFeNi high-entropy alloy system with multiprincipal elements, Metallurgical and Materials Transactions A 36 (5) (2005) 1263–1271. `doi:10.1007/s11661-005-0218-9`.

[19] K. Pradeep, C. Tasan, M. Yao, Y. Deng, H. Springer, D. Raabe, Non-equiatomic high entropy alloys: Approach towards rapid alloy screening and property-oriented design, Materials Science and Engineering: A 648 (2015) 183–192. `doi:10.1016/j.msea.2015.09.010`.

[20] D. Ma, B. Grabowski, F. Körmann, J. Neugebauer, D. Raabe, Ab initio thermodynamics of the

CoCrFeMnNi high entropy alloy: Importance of entropy contributions beyond the configurational one, Acta Materialia 100 (2015) 90–97. `doi:10.1016/j.actamat.2015.08.050`.

[21] O. Senkov, G. Wilks, J. Scott, D. Miracle, Mechanical properties of $Nb_{25}Mo_{25}Ta_{25}W_{25}$ and $V_{20}Nb_{20}Mo_{20}Ta_{20}W_{20}$ refractory high entropy alloys, Intermetallics 19 (5) (2011) 698–706. `doi:10.1016/j.intermet.2011.01.004`.

[22] H. Chen, A. Kauffmann, S. Seils, T. Boll, C. Liebscher, I. Harding, K. Kumar, D. Szabó, S. Schlabach, S. Kauffmann-Weiss, F. Müller, B. Gorr, H.-J. Christ, M. Heilmaier, Crystallographic ordering in a series of Al-containing refractory high entropy alloys Ta–Nb–Mo–Cr–Ti–Al, Acta Materialia 176 (2019) 123–133. `doi:10.1016/j.actamat.2019.07.001`.

[23] H. Chen, A. Kauffmann, B. Gorr, D. Schliephake, C. Seemüller, J. Wagner, H.-J. Christ, M. Heilmaier, Microstructure and mechanical properties at elevated temperatures of a new Al-containing refractory high-entropy alloy Nb-Mo-Cr-Ti-Al, Journal of Alloys and Compounds 661 (2016) 206–215. `doi:10.1016/j.jallcom.2015.11.050`.

[24] B. S. Murty, J. W. Yeh, S. Ranganathan, P. P. Bhattacharjee, High-entropy alloys, Elsevier, Amsterdam, 2019.

[25] S. V. Divinski, A. V. Pokoev, N. Esakkiraja, A. Paul, A mystery of “sluggish diffusion” in high-entropy alloys: The truth or a myth?, Diffusion Foundations 17 (2018) 69–104. `doi:10.4028/www.scientific.net/df.17.69`.

[26] J.-W. Yeh, Alloy design strategies and future trends in high-entropy alloys, JOM 65 (12) (2013) 1759–1771. `doi:10.1007/s11837-013-0761-6`.

[27] D. B. Miracle, High entropy alloys as a bold step

forward in alloy development (12 2019). `doi:10.1038/s41467-019-09700-1`.

[28] Y. Zhang, T. T. Zuo, Z. Tang, M. C. Gao, K. A. Dahmen, P. K. Liaw, Z. P. Lu, Microstructures and properties of high-entropy alloys, Progress in Materials Science 61 (2014) 1–93. `doi:10.1016/j.pmatsci.2013.10.001`.

[29] Y. Zhang, Y. Zhou, J. Lin, G. Chen, P. Liaw, Solid-solution phase formation rules for multi-component alloys, Advanced Engineering Materials 10 (6) (2008) 534–538. `doi:10.1002/adem.200700240`.

[30] F. Otto, Y. Yang, H. Bei, E. George, Relative effects of enthalpy and entropy on the phase stability of equiatomic high-entropy alloys, Acta Materialia 61 (7) (2013) 2628–2638. `doi:10.1016/j.actamat.2013.01.042`.

[31] W. Hume-Rothery, Atomic diameters, atomic volumes and solid solubility relations in alloys, Acta Metallurgica 14 (1) (1966) 17–20. `doi:10.1016/0001-6160(66)90267-7`.

[32] D. A. Porter, K. E. Easterling, M. Y. Sherif, Phase Transformations in Metals and Alloys, 3rd Edition, CRC Press, 2009.

[33] Y.-F. Kao, S.-K. Chen, T.-J. Chen, P.-C. Chu, J.-W. Yeh, S.-J. Lin, Electrical, magnetic, and hall properties of AlxCoCrFeNi high-entropy alloys, Journal of Alloys and Compounds 509 (5) (2011) 1607–1614. `doi:10.1016/j.jallcom.2010.10.210`.

[34] M.-H. Tsai, Physical properties of high entropy alloys, Entropy 15 (2013) 5338–5345. `doi:10.3390/e15125338`.

[35] K. Kulkarni, G. P. S. Chauhan, Investigations of quaternary interdiffusion in a constituent system of high entropy alloys, Aip Advances 5 (9) (2015). `doi:10.1063/1.4931806`.

[36] J. Dąbrowa, W. Kucza, G. Cieślak, T. Kulik, M. Danielewski, J.-W. Yeh, Interdiffusion in the fcc-structured Al-Co-Cr-Fe-Ni high entropy alloys: experimental studies and numerical simulations, Journal of Alloys and Compounds 674 (2016) 455–462. `doi:10.1016/j.jallcom.2016.03.046`.

[37] M. Vaidya, K. Pradeep, B. Murty, G. Wilde, S. Divinski, Bulk tracer diffusion in CoCrFeNi and CoCrFeMnNi high entropy alloys, Acta Materialia 146 (2018) 211–224. `doi:10.1016/j.actamat.2017.12.052`.

[38] W. Kucza, J. Dąbrowa, G. Cieślak, K. Berent, T. Kulik, M. Danielewski, Studies of “sluggish diffusion” effect in Co-Cr-Fe-Mn-Ni, Co-Cr-Fe-Ni and Co-Fe-Mn-Ni high entropy alloys; determination of tracer diffusivities by combinatorial approach, Journal of Alloys and Compounds 731 (2018) 920–928. `doi:10.1016/j.jallcom.2017.10.108`.

[39] D. Gaertner, J. Kottke, G. Wilde, S. V. Divinski, Y. Chumlyakov, Tracer diffusion in single crystalline CoCrFeNi and CoCrFeMnNi high entropy alloys, Journal of Materials Research 33 (19) (2018) 3184–3191. `doi:10.1557/jmr.2018.162`.

[40] S. Ranganathan, Alloyed pleasures: Multimetallic cocktails, Current science 85 (2003) 1404–1406.

[41] J. W. Yeh, Y. L. Chen, S. J. Lin, S. K. Chen, High-entropy alloys – a new era of exploitation, Materials Science Forum 560 (2007) 1–9. `doi:10.4028/www.scientific.net/msf.560.1`.

[42] Y. Zhang, T. Zuo, Y. Cheng, P. K. Liaw, High-entropy alloys with high saturation magnetization, electrical resistivity and malleability, Scientific Reports 3 (1) (2013) 1–7. `doi:10.1038/srep01455`.

[43] C. Bohnert, Numerische Untersuchung des Verformungs- und Bruchverhaltens von

einkristallinem Wolfram auf mikroskopischer Ebene, Vol. 52, KIT Scientific Publishing, 2016. `doi:10.5445/KSP/1000049866`.

[44] A. H. Cottrell, D. L. Dexter, Dislocations and plastic flow in crystals, American Journal of Physics 22 (4) (1954) 242–243. `doi:10.1119/1.1933704`.

[45] D. R. Gaskell, D. E. Laughlin, Introduction to the thermodynamics of materials, CRC Press, Boca Raton, FL, 2017.

[46] D. Hull, D. J. Bacon, Introduction to dislocations, Butterworth-Heinemann, Oxford, 2001.

[47] P. M. Anderson, J. P. Hirth, J. Lothe, Theory of dislocations, Cambridge University Press, New York, 2017.

[48] A. Seeger, Peierls barriers, kinks, and flow stress: Recent progress, Zeitschrift für Metallkunde 93 (8) (2002) 760–777. `doi:10.3139/146.020760`.

[49] G. E. Dieter, Mechanical metallurgy, Vol. 3 of McGraw-Hill series in materials science and engineering, McGraw-Hill, New York, 1986.

[50] Z. H. Aitken, Y.-W. Zhang, Revealing the deformation twinning nucleation mechanism of BCC HEAs, MRS Communications 9 (1) (2019) 406–412. `doi:10.1557/mrc.2019.16`.

[51] G. I. Taylor, C. F. Elam, The distortion of iron crystals, Proceedings of the Royal Society of London. Series A, Containing Papers of a Mathematical and Physical Character 112 (761) (1926) 337–361. `doi:10.1098/rspa.1926.0116`.

[52] A. W. Sleeswyk, $\frac{1}{2}$<111> screw dislocations and the nucleation of {112}<111> twins in the b.c.c. lattice, The Philosophical Magazine: A Journal of Theoretical Experimental and Applied Physics 8 (93) (1963) 1467–1486. `doi:10.1080/14786436308207311`.

[53] S. Mahajan, Nucleation and growth of deformation twins in Mo-35 at. % Re alloy, Philosophical Magazine 26 (1) (1972) 161–171. `doi:10.1080/14786437208221027`.

[54] W. Shockley, Solid state physics in electronics and in metallurgy, JOM 4 (8) (1952) 829–842. `doi:10.1007/bf03398148`.

[55] A. Seeger, The temperature and strain-rate dependence of the flow stress of body-centred cubic metals: A theory based on kink-kink interactions, International Journal of Materials Research 72 (6) (1981) 369–380. `doi:10.1515/ijmr-1981-720601`.

[56] V. Vítek, Thermally activated motion of screw dislocations in B.C.C. metals, physica status solidi (b) 18 (2) (1966) 687–701. `doi:10.1002/pssb.19660180221`.

[57] A. Seeger, U. Holzwarth, Slip planes and kink properties of screw dislocations in high-purity niobium, Philosophical Magazine 86 (25–26) (2006) 3861–3892. `doi:10.1080/14786430500531769`.

[58] A. Seeger, The flow stress of high-purity refractory body-centred cubic metals and its modification by atomic defects, Le Journal de Physique IV 05 (C7) (1995) C7–45–C7–65. `doi:10.1051/jp4:1995704`.

[59] A. Seeger, Why anomalous slip in body-centred cubic metals ?, Materials Science and Engineering: A 319-321 (2001) 254–260. `doi:10.1016/S0921-5093(01)00958-3`.

[60] H. Chen, A. Kauffmann, S. Laube, I.-C. Choi, R. Schwaiger, Y. Huang, K. Lichtenberg, F. Müller, B. Gorr, H.-J. Christ, M. Heilmaier, Contribution of lattice distortion to solid solution strengthening in a series of refractory high entropy alloys, Metallurgical and Materials Transactions A 49 (3) (2017) 772–781. `doi:10.1007/s11661-017-4386-1`.

[61] G. M. Pharr, D. S. Harding, W. C. Oliver, Measurement of fracture toughness in thin films and small volumes using nanoindentation methods, in: Mechanical Properties and Deformation Behavior of Materials Having Ultra-Fine Microstructures, NATO ASI Series, vol. 233, Springer Netherlands, Dordrecht, 1993, pp. 449–461. `doi:10.1007/978-94-011-1765-4_29`.

[62] A. Shimamoto, K. Tanaka, Y. Akiyma, H. Yoshizaki, Nanoindentation of glass with a tip-truncated berkovich indenter, Philosophical Magazine A 74 (5) (1996) 1097–1105. `doi:10.1080/01418619608239710`.

[63] T. Sawa, K. Tanaka, Nanoindentation of natural diamond, Philosophical Magazine A 82 (10) (2002) 1851–1856. `doi:10.1080/01418610208235696`.

[64] K. Kese, D. J. Rowcliffe, Nanoindentation method for measuring residual stress in brittle materials, Journal of the American Ceramic Society 86 (5) (2003) 811–816. `doi:10.1111/j.1151-2916.2003.tb03380.x`.

[65] C. Schuh, T. Nieh, A nanoindentation study of serrated flow in bulk metallic glasses, Acta Materialia 51 (1) (2003) 87–99. `doi:10.1016/s1359-6454(02)00303-8`.

[66] L. Taylor, D. Papadopoulos, P. Dunn, A. Bentham, J. Mitchell, M. Snowden, Mechanical characterisation of powders using nanoindentation, Powder Technology 143–144 (2004) 179–185. `doi:10.1016/j.powtec.2004.04.012`.

[67] S. Nowak, P. Ochin, A. Pasko, O. Maciejak, P. Aubert, Y. Champion, Nanoindentation analysis of the mechanical behavior of Zr-based metallic glasses with Sn, Ta and W additions, Journal of Alloys and Compounds 483 (1–2) (2009) 139–142. `doi:10.1016/j.jallcom.2008.07.178`.

[68] S. H. Nandam, Y. Ivanisenko, R. Schwaiger, Z. Śniadecki, X. Mu, D. Wang, R. Chellali, T. Boll, A. Kilmametov, T. Bergfeldt, H. Gleiter, H. Hahn, Cu-Zr nanoglasses: Atomic structure, thermal stability and indentation properties, Acta Materialia 136 (2017) 181–189. `doi:10.1016/j.actamat.2017.07.001`.

[69] M. A. Krivoglaz, A. A. Smirnov, The theory of order-disorder in alloys, Macdonald, London, 1964.

[70] N. S. Stoloff, C. C. Koch, C. T. Liu, O. Izumi, High-Temperature Ordered Intermetallic Alloys II, Materials Research Society, Pittsburgh, PA, 1987.

[71] J. M. Cowley, An approximate theory of order in alloys, Physical Review 77 (5) (1950) 669. `doi:10.1103/physrev.77.669`.

[72] J. M. Cowley, Short- and long-range order parameters in disordered solid solutions, Physical Review 120 (5) (1960) 1648–1657. `doi:10.1103/physrev.120.1648`.

[73] W. P. Huhn, M. Widom, Prediction of A2 to B2 phase transition in the high-entropy alloy Mo-Nb-Ta-W, JOM 65 (12) (2013) 1772–1779. `doi:10.1007/s11837-013-0772-3`.

[74] M. Widom, W. P. Huhn, S. Maiti, W. Steurer, Hybrid Monte Carlo/molecular dynamics simulation of a refractory metal high entropy alloy, Metallurgical and Materials Transactions A 45 (1) (2013) 196–200. `doi:10.1007/s11661-013-2000-8`.

[75] E. Meshkov, I. Novoselov, A. Shapeev, A. Yanilkin, Sublattice formation in CoCrFeNi high-entropy alloy, Intermetallics 112 (2019) 106542. `doi:10.1016/j.intermet.2019.106542`.

[76] M. Rahaman, First-principles investigations of ordering in binary alloys, Ph.D. thesis, KTH Royal Institute of Technology (2013).

[77] Z. Pei, R. Li, M. C. Gao, G. M. Stocks, Statistics of the NiCoCr medium-entropy alloy: Novel aspects of an old puzzle, npj Computational Materials 6 (1) (2020) 1–6. `doi:10.1038/s41524-020-00389-1`.

[78] D. M. King, S. C. Middleburgh, L. Edwards, G. R. Lumpkin, M. Cortie, Predicting the crystal structure and phase transitions in high-entropy alloys, JOM 67 (10) (2015) 2375–2380. `doi:10.1007/s11837-015-1495-4`.

[79] P. Singh, A. V. Smirnov, D. D. Johnson, Atomic short-range order and incipient long-range order in high-entropy alloys, Physical Review B 91 (22) (2015) 224204. `doi:10.1103/physrevb.91.224204`.

[80] J. L. Meijering, Segregation in regular ternary solutions, Philips Res. Rep. 5 (1950) 333–356.

[81] J. E. Morral, S. Chen, A regular solution model for a single-phase high entropy and enthalpy alloy, Journal of Phase Equilibria and Diffusion 38 (4) (2017) 382–390. `doi:10.1007/s11669-017-0578-z`.

[82] W. L. Bragg, E. J. Williams, The effect of thermal agitation on atomic arrangement in alloys, Proceedings of the Royal Society of London. Series A - Mathematical and Physical Sciences 151 (874) (1935) 540–566. `doi:10.1098/rspa.1935.0165`.

[83] E. Ising, Beitrag zur Theorie des Ferromagnetismus, Zeitschrift für Physik 31 (1) (1925) 253–258. `doi:10.1007/bf02980577`.

[84] C. Domb, R. B. Potts, Order-disorder statistics IV. A two-dimensional model with first and second interactions, Proceedings of the Royal Society of London. Series A. Mathematical and Physical Sciences 210 (1100) (1951) 125–141. `doi:10.1098/rspa.1951.0235`.

[85] R. B. Potts, Some generalized order-disorder transformations, Mathematical Proceedings of the Cam-

bridge Philosophical Society 48 (1) (1952) 106–109. `doi:10.1017/s0305004100027419`.

[86] C. P. Herrero, Ising model in small-world networks, Physical Review E 65 (6) (2002) 066110. `doi:10.1103/physreve.65.066110`.

[87] J. Tobochnik, Properties of the q-state clock model for q = 4, 5, and 6, Physical Review B 26 (11) (1982) 6201–6207. `doi:10.1103/physrevb.26.6201`.

[88] A. M. Ferrenberg, D. P. Landau, Critical behavior of the three-dimensional Ising model: A high-resolution Monte Carlo study, Physical Review B 44 (10) (1991) 5081–5091. `doi:10.1103/physrevb.44.5081`.

[89] R. J. Baxter, Potts model at the critical temperature, Journal of Physics C: Solid State Physics 6 (23) (1973) L445–L448. `doi:10.1088/0022-3719/6/23/005`.

[90] K. Binder, Static and dynamic critical phenomena of the two-dimensional q-state Potts model, Journal of Statistical Physics 24 (1) (1981) 69–86. `doi:10.1007/bf01007636`.

[91] P. D. Scholten, L. J. Irakliotis, Critical behavior of the q -state clock model in three dimensions, Physical Review B 48 (2) (1993) 1291–1294. `doi:10.1103/physrevb.48.1291`.

[92] O. F. de Alcantara Bonfim, Finite-size effects and phase transition in the three-dimensional three-state Potts model, Journal of Statistical Physics 62 (1–2) (1991) 105–115. `doi:10.1007/bf01020861`.

[93] H. J. Herrmann, Monte Carlo simulation of the three-dimensional Potts model, Zeitschrift für Physik B Condensed Matter and Quanta 35 (2) (1979) 171–175. `doi:10.1007/bf01321243`.

[94] C. P. Herrero, Antiferromagnetic Ising model in scale-free networks, The European Physical Jour-

nal B 70 (3) (2009) 435–441. `doi:10.1140/epjb/e2009-00240-2`.

[95] R. J. Baxter, Derivation of the order parameter of the chiral Potts model, Phys Rev Lett 94 (13) (2005) 130602. `doi:10.1103/physrevlett.94.130602`.

[96] O. F. d. A. Bonfim, Critical dynamics of the q - state Potts model in two dimensions, Europhysics Letters (EPL) 4 (3) (1987) 373–376. `doi:10.1209/0295-5075/4/3/020`.

[97] R. H. Swendsen, S. Krinsky, Monte Carlo renormalization group and Ising models with $n >\sim 2$, Physical Review Letters 43 (3) (1979) 177–180. `doi:10.1103/physrevlett.43.177`.

[98] D. L. Lin, H. Che, W. Lai, T. F. George, Critical temperature of Ising films with cubic lattices, Physical Review E 49 (3) (1994) 2155–2160. `doi:10.1103/physreve.49.2155`.

[99] D. Hajdukovic, On the location of the critical point of the q-state Potts model on the hypercubic lattice, Journal of Physics A: Mathematical and General 16 (6) (1983) L193–L198. `doi:10.1088/0305-4470/16/6/004`.

[100] A. Bortz, M. Kalos, J. Lebowitz, A new algorithm for Monte Carlo simulation of Ising spin systems, Journal of Computational Physics 17 (1) (1975) 10–18. `doi:10.1016/0021-9991(75)90060-1`.

[101] A. Sadiq, A new algorithm for the Monte Carlo simulation of spin-exchange kinetics of Ising systems, Journal of Computational Physics 55 (3) (1984) 387–396. `doi:10.1016/0021-9991(84)90028-7`.

[102] R. J. Glauber, Time-dependent statistics of the Ising model, Journal of Mathematical Physics 4 (2) (1963) 294–307. `doi:10.1063/1.1703954`.

[103] K. Kawasaki, T. Yamada, Time-dependent Ising

model with long range interaction, Progress of Theoretical Physics 39 (1) (1968) 1–25. `doi:10.1143/ptp.39.1`.

[104] Y. Gao, H. Bei, Strength statistics of single crystals and metallic glasses under small stressed volumes, Progress in Materials Science 82 (2016) 118–150. `doi:10.1016/j.pmatsci.2016.05.002`.

[105] F. Körmann, A. V. Ruban, M. H. Sluiter, Long-ranged interactions in bcc NbMoTaW high-entropy alloys, Materials Research Letters 5 (1) (2016) 35–40. `doi:10.1080/21663831.2016.1198837`.

[106] M. M. Nygård, W. A. Sławiński, G. Ek, M. H. Sørby, M. Sahlberg, D. A. Keen, B. C. Hauback, Local order in high-entropy alloys and associated deuterides – a total scattering and reverse Monte Carlo study, Acta Materialia 199 (2020) 504–513. `doi:10.1016/j.actamat.2020.08.045`.

[107] A. Slepoy, A. P. Thompson, S. J. Plimpton, A constant-time kinetic Monte Carlo algorithm for simulation of large biochemical reaction networks, The Journal of Chemical Physics 128 (20) (May 2008). `doi:10.1063/1.2919546`.

[108] J. A. Mitchell, F. Abdeljawad, C. Battaile, C. Garcia-Cardona, E. A. Holm, E. R. Homer, J. Madison, T. M. Rodgers, A. P. Thompson, V. Tikare, E. Webb, S. J. Plimpton, Parallel simulation via SPPARKS of on-lattice kinetic and Metropolis Monte Carlo models for materials processing, Modelling and Simulation in Materials Science and Engineering 31 (5) (2023) 055001. `doi:10.1088/1361-651x/accc4b`.

[109] A. Stukowski, Visualization and analysis of atomistic simulation data with OVITO–the Open Visualization Tool, Modelling and Simulation in Materials Science and Engineering 18 (1) (2009) 015012. `doi:10.1088/0965-0393/18/1/015012`.

[110] T. L. Hill, An Introduction to Statistical Thermodynamics, Dover Books on Physics, Dover Publications, 1997.

[111] L. Guttman, Monte Carlo computations on the Ising model. The body-centered cubic lattice, The Journal of Chemical Physics 34 (3) (1961) 1024–1036. `doi:10.1063/1.1731628`.

[112] D. Schebarchov, T. P. Schulze, S. C. Hendy, Degenerate Ising model for atomistic simulation of crystal-melt interfaces, The Journal of Chemical Physics 140 (7) (2014) 74704. `doi:10.1063/1.4864462`.

[113] M.-R. Chen, S.-J. Lin, J.-W. Yeh, M.-H. Chuang, S.-K. Chen, Y.-S. Huang, Effect of vanadium addition on the microstructure, hardness, and wear resistance of $Al_{0.5}$CoCrCuFeNi high-entropy alloy, Metallurgical and Materials Transactions A 37 (5) (2006) 1363–1369. `doi:10.1007/s11661-006-0081-3`.

[114] J. Yeh, S. Chen, S. Lin, J. Gan, T. Chin, T. Shun, C. Tsau, S. Chang, Nanostructured high-entropy alloys with multiple principal elements: novel alloy design concepts and outcomes, Advanced Engineering Materials 6 (5) (2004) 299–303. `doi:10.1002/adem.200300567`.

[115] S. A. Kube, J. Schroers, Metastability in high entropy alloys, Scripta Materialia 186 (2020) 392–400. `doi:10.1016/j.scriptamat.2020.05.049`.

[116] W. Oliver, G. Pharr, An improved technique for determining hardness and elastic modulus using load and displacement sensing indentation experiments, Journal of Materials Research 7 (6) (1992) 1564–1583. `doi:10.1557/jmr.1992.1564`.

[117] G. M. Pharr, E. G. Herbert, Y. Gao, The indentation size effect: a critical examination of experimental observations and mechanistic interpretations, Annual

Review of Materials Research 40 (1) (2010) 271–292. doi:10.1146/annurev-matsci-070909-104456.

[118] W. D. Nix, H. Gao, Indentation size effects in crystalline materials: A law for strain gradient plasticity, Journal of the Mechanics and Physics of Solids 46 (3) (1998) 411–425. doi:10.1016/s0022-5096(97)00086-0.

[119] N. M. Pugno, A general shape/size-effect law for nanoindentation, Acta Materialia 55 (6) (2007) 1947–1953. doi:10.1016/j.actamat.2006.10.053.

[120] A. C. Fischer-Cripps, Nanoindentation testing, in: Nanoindentation, Mechanical Engineering Series, Springer, New York, 2011, pp. 21–37. doi:10.1007/978-1-4419-9872-9_2.

[121] K. W. McElhaney, J. J. Vlassak, W. D. Nix, Determination of indenter tip geometry and indentation contact area for depth-sensing indentation experiments, Journal of Materials Research 13 (5) (1998) 1300–1306. doi:10.1557/JMR.1998.0185.

[122] C. A. Schuh, A. C. Lund, Application of nucleation theory to the rate dependence of incipient plasticity during nanoindentation, Journal of Materials Research 19 (7) (2004) 2152–2158. doi:10.1557/jmr.2004.0276.

[123] J. K. Mason, A. C. Lund, C. A. Schuh, Determining the activation energy and volume for the onset of plasticity during nanoindentation, Physical Review B 73 (5) (2006) 054102. doi:10.1103/physrevb.73.054102.

[124] H. Hertz, Ueber die Berührung fester elastischer Körper., crll 1882 (92) (1882) 156–171. doi:10.1515/crll.1882.92.156.

[125] F. Pöhl, Pop-in behavior and elastic-to-plastic transition of polycrystalline pure iron during sharp nanoin-

dentation, Scientific Reports 9 (1) (2019) 15350. `doi:10.1038/s41598-019-51644-5`.

[126] W. Weibull, A statistical distribution function of wide applicability, Journal of Applied Mechanics 18 (3) (1951) 293–297. `doi:10.1115/1.4010337`.

[127] F. Li, On the origin of the high strain rate sensitivity in a superplastic Al-4.5% Mg alloy, Scripta Metallurgica et Materialia 32 (3) (1995) 463–468. `doi:10.1016/s0956-716x(99)80083-1`.

[128] R. Limbach, B. P. Rodrigues, L. Wondraczek, Strain-rate sensitivity of glasses, Journal of Non-Crystalline Solids 404 (2014) 124–134. `doi:10.1016/j.jnoncrysol.2014.08.023`.

[129] T. G. Nieh, J. Wadsworth, Homogeneous deformation of bulk metallic glasses, Scripta Materialia 54 (3) (2006) 387–392. `doi:10.1016/j.scriptamat.2005.04.052`.

[130] V. Maier, C. Schunk, M. Göken, K. Durst, Microstructure-dependent deformation behaviour of bcc-metals – indentation size effect and strain rate sensitivity, Philosophical Magazine 95 (16–18) (2014) 1766–1779. `doi:10.1080/14786435.2014.982741`.

[131] J. Gil Sevillano, E. Aernoudt, Low energy dislocation structures in highly deformed materials, Materials Science and Engineering 86 (1987) 35–51. `doi:10.1016/0025-5416(87)90441-1`.

[132] J. Gil Sevillano, I. Ocaña Arizcorreta, L. Kubin, Intrinsic size effects in plasticity by dislocation glide, Materials Science and Engineering: A 309–310 (2001) 393–405. `doi:10.1016/s0921-5093(00)01733-0`.

[133] D. Tabor, The hardness of metals, Oxford classic texts in the physical sciences, Oxford University Press, Oxford, 2000.

[134] M. Mayo, W. Nix, A micro-indentation study of

superplasticity in Pb, Sn, and Sn-38 wt% Pb, Acta Metallurgica 36 (8) (1988) 2183–2192. `doi:10.1016/0001-6160(88)90319-7`.

[135] M. Mayo, W. Nix, Measuring and understanding strain rate sensitive deformation with the nanoindenter, in: Strength of Metals and Alloys (ICSMA 8), Elsevier, 1989, pp. 1415–1420. `doi:10.1016/b978-0-08-034804-9.50224-2`.

[136] M. Mayo, R. Siegel, Y. Liao, W. Nix, Nanoindentation of nanocrystalline ZnO, Journal of Materials Research 7 (4) (1992) 973–979. `doi:10.1557/jmr.1992.0973`.

[137] A. Atkins, D. Tabor, Plastic indentation in metals with cones, Journal of the Mechanics and Physics of Solids 13 (3) (1965) 149–164. `doi:10.1016/0022-5096(65)90018-9`.

[138] A. G. Atkins, D. Tabor, Hardness and deformation properties of solids at very high temperatures, Proceedings of the Royal Society of London. Series A. Mathematical and Physical Sciences 292 (1431) (1966) 441–459. `doi:10.1098/rspa.1966.0146`.

[139] B. N. Lucas, W. C. Oliver, G. M. Pharr, J.-L. Loubet, Time dependent deformation during indentation testing, MRS Online Proceedings Library 436 (1996) 233–238. `doi:10.1557/proc-436-233`.

[140] Q. Wei, Strain rate effects in the ultrafine grain and nanocrystalline regimes—influence on some constitutive responses, Journal of Materials Science 42 (5) (2007) 1709–1727. `doi:10.1007/s10853-006-0700-9`.

[141] G. B. Gibbs, The thermodynamics of thermally-activated dislocation glide, physica status solidi (b) 10 (2) (1965) 507–512. `doi:10.1002/pssb.2220100212`.

[142] L. Lu, R. Schwaiger, Z. Shan, M. Dao, K. Lu,

S. Suresh, Nano-sized twins induce high rate sensitivity of flow stress in pure copper, Acta Materialia 53 (7) (2005) 2169–2179. `doi:10.1016/j.actamat.2005.01.031`.

[143] V. Maier, K. Durst, J. Mueller, B. Backes, H. W. Höppel, M. Göken, Nanoindentation strain-rate jump tests for determining the local strain-rate sensitivity in nanocrystalline Ni and ultrafine-grained Al, Journal of Materials Research 26 (11) (2011) 1421–1430. `doi:10.1557/jmr.2011.156`.

[144] J. B. Wachtman, W. E. Tefft, D. G. Lam, C. S. Apstein, Exponential temperature dependence of Young's modulus for several oxides, Physical Review 122 (6) (1961) 1754–1759. `doi:10.1103/physrev.122.1754`.

[145] G. Pharr, W. Oliver, F. Brotzen, On the generality of the relationship among contact stiffness, contact area, and elastic modulus during indentation, Journal of Materials Research 7 (3) (1992) 613–617. `doi:10.1557/jmr.1992.0613`.

[146] S. Pathak, J. L. Riesterer, S. R. Kalidindi, J. Michler, Understanding pop-ins in spherical nanoindentation, Applied Physics Letters 105 (16) (2014) 161913. `doi:10.1063/1.4898698`.

[147] I. Salehinia, D. Bahr, The impact of a variety of point defects on the inception of plastic deformation in dislocation-free metals, Scripta Materialia 66 (6) (2012) 339–342. `doi:10.1016/j.scriptamat.2011.11.028`.

[148] G. Laplanche, P. Gadaud, L. Perrière, I. Guillot, J. Couzinié, Temperature dependence of elastic moduli in a refractory HfNbTaTiZr high-entropy alloy, Journal of Alloys and Compounds 799 (2019) 538–545. `doi:10.1016/j.jallcom.2019.05.322`.

[149] G. Dirras, H. Couque, L. Lilensten, A. Heczel,

D. Tingaud, J. P. Couzinié, L. Perrière, J. Gubicza, I. Guillot, Mechanical behavior and microstructure of $Ti_{20}Hf_{20}Zr_{20}Ta_{20}Nb_{20}$ high-entropy alloy loaded under quasi-static and dynamic compression conditions, Materials Characterization 111 (2016) 106–113. `doi:10.1016/j.matchar.2015.11.018`.

[150] Y. P. Varshni, Temperature dependence of the elastic constants, Physical Review B 2 (10) (1970) 3952–3958. `doi:10.1103/physrevb.2.3952`.

[151] W. Callister, D. Rethwisch, Materials Science and Engineering: An Introduction, 8th Edition, Wiley, 2009.

[152] T. Chihi, M. Fatmi, B. Ghebouli, M. Ghebouli, Ab initio study of the parent (BCC) and martensitic (HCP) phases of nonferrous Ti, Zr, and Hf metals, Chinese Journal of Physics 54 (1) (2016) 127–134. `doi:10.1016/j.cjph.2016.03.014`.

[153] Y. Talmor, E. Walker, S. Steinemann, Elastic constants of nionium up to the melting point, Solid State Communications 23 (9) (1977) 649–651. `doi:10.1016/0038-1098(77)90541-5`.

[154] W. Köster, Zur Analyse der in der Theorie des Ferromagnetismus vorkommenden Größe σ_i, Zeitschrift für Physik 124 (7–12) (1948) 545–565. `doi:10.1007/bf01668891`.

[155] H. Ogi, S. Kai, H. Ledbetter, R. Tarumi, M. Hirao, K. Takashima, Titanium's high-temperature elastic constants through the hcp–bcc phase transformation, Acta Materialia 52 (7) (2004) 2075–2080. `doi:10.1016/j.actamat.2004.01.002`.

[156] R. Farraro, R. B. Mclellan, Temperature dependence of the Young's modulus and shear modulus of pure nickel, platinum, and molybdenum, Metallurgical Transactions A 8 (10) (1977) 1563–1565. `doi:10.1007/bf02644859`.

[157] J. Tallon, A. Wolfenden, Temperature dependence of the elastic constants of aluminum, Journal of Physics and Chemistry of Solids 40 (11) (1979) 831–837. `doi:10.1016/0022-3697(79)90037-4`.

[158] I.-C. Choi, C. Brandl, R. Schwaiger, Thermally activated dislocation plasticity in body-centered cubic chromium studied by high-temperature nanoindentation, Acta Materialia 140 (2017) 107–115. `doi:10.1016/j.actamat.2017.08.026`.

[159] M. M. Biener, J. Biener, A. M. Hodge, A. V. Hamza, Dislocation nucleation in bcc Ta single crystals studied by nanoindentation, Physical Review B 76 (16) (2007) 165422. `doi:10.1103/PhysRevB.76.165422`.

[160] H. Conrad, W. Hayes, Thermally-activated deformation of the body centered cubic metals at low temperatures, Tech. Rep. TDR-169(3240-11)TN-7, Commander Space Systems Division, United States Air Force (Mar. 1963). `doi:10.21236/ad0402793`.

[161] C. A. Schuh, J. K. Mason, A. C. Lund, Quantitative insight into dislocation nucleation from high-temperature nanoindentation experiments, Nature Materials 4 (8) (2005) 617–621. `doi:10.1038/nmat1429`.

[162] R. Fleischer, Substitutional solution hardening, Acta Metallurgica 11 (3) (1963) 203–209. `doi:10.1016/0001-6160(63)90213-x`.

[163] R. Labusch, A statistical theory of solid solution hardening, physica status solidi (b) 41 (2) (1970) 659–669. `doi:10.1002/pssb.19700410221`.

[164] J.-P. Couzinié, O. Senkov, D. Miracle, G. Dirras, Comprehensive data compilation on the mechanical properties of refractory high-entropy alloys, Data in Brief 21 (2018) 1622–1641. `doi:10.1016/j.dib.2018.10.071`.

[165] C. Varvenne, A. Luque, W. A. Curtin, Theory of

strengthening in fcc high entropy alloys, Acta Materialia 118 (2016) 164–176. doi:10.1016/j.actamat.2016.07.040.

[166] I. Toda-Caraballo, P. Rivera-Díaz-del Castillo, A criterion for the formation of high entropy alloys based on lattice distortion, Intermetallics 71 (2016) 76–87. doi:10.1016/j.intermet.2015.12.011.

[167] A. Kehrel, C. Moelle, H. J. Fecht, Mechanical properties of nanostructured niobium on a microscopic scale, in: Nanophase Materials, NATO ASI Series, vol. 260, Springer Netherlands, Dordrecht, 1994, pp. 287–292. doi:10.1007/978-94-011-1076-1_34.

[168] R. Fleisgher, Solution hardening, Acta Metallurgica 9 (11) (1961) 996–1000. doi:10.1016/0001-6160(61)90242-5.

[169] L. Wang, H. Bei, T. Li, Y. Gao, E. George, T. Nieh, Determining the activation energies and slip systems for dislocation nucleation in body-centered cubic Mo and face-centered cubic Ni single crystals, Scripta Materialia 65 (3) (2011) 179–182. doi:10.1016/j.scriptamat.2011.03.036.

[170] D. Wu, T. Nieh, Incipient plasticity and dislocation nucleation in body-centered cubic chromium, Materials Science and Engineering: A 609 (2014) 110–115. doi:10.1016/j.msea.2014.04.107.

[171] H. Somekawa, C. A. Schuh, Effect of solid solution elements on nanoindentation hardness, rate dependence, and incipient plasticity in fine grained magnesium alloys, Acta Materialia 59 (20) (2011) 7554–7563. doi:10.1016/j.actamat.2011.08.047.

[172] C. Zhu, Z. Lu, T. Nieh, Incipient plasticity and dislocation nucleation of FeCoCrNiMn high-entropy alloy, Acta Materialia 61 (8) (2013) 2993–3001. doi:10.1016/j.actamat.2013.01.059.

[173] Y. Ye, Z. Lu, T. Nieh, Dislocation nucleation during

nanoindentation in a body-centered cubic TiZrHfNb high-entropy alloy, Scripta Materialia 130 (2017) 64–68. `doi:10.1016/j.scriptamat.2016.11.019`.

[174] L. Wang, C. Fu, Y. Wu, R. Li, Y. Wang, X. Hui, Ductile Ti-rich high-entropy alloy controlled by stress induced martensitic transformation and mechanical twinning, Materials Science and Engineering: A 763 (2019) 138147. `doi:10.1016/j.msea.2019.138147`.

[175] G. Sainath, B. K. Choudhary, Deformation behaviour of body centered cubic iron nanopillars containing coherent twin boundaries, Philosophical Magazine 96 (32–34) (2016) 3502–3523. `doi:10.1080/14786435.2016.1240377`.

[176] X. Wang, Y. Zhang, Y. Qiao, G. Chen, Novel microstructure and properties of multicomponent CoCrCuFeNiTix alloys, Intermetallics 15 (3) (2007) 357–362. `doi:10.1016/j.intermet.2006.08.005`.

[177] H. Chen, T. Hanemann, S. Seils, D. Schliephake, A. S. Tirunilai, M. Heilmaier, K.-P. Weiss, A. Kauffmann, Influence of temperature and plastic strain on deformation mechanisms and kink band formation in homogenized HfNbTaTiZr, Crystals 11 (2) (2021) 81. `doi:10.3390/cryst11020081`.

[178] E. Orowan, A type of plastic deformation new in metals, Nature 149 (3788) (1942) 643–644. `doi:10.1038/149643a0`.

[179] W. Xi, W. Sun, G. D. Han, Formed kink band and long-period stacking structure relaxed stress induced by 10–12 twin in deformed magnesium alloy, Materials Characterization 103 (2015) 170–174. `doi:10.1016/j.matchar.2015.03.020`.

[180] S. Sadeghpour, S. Abbasi, M. Morakabati, L. Karjalainen, Effect of dislocation channeling and kink band formation on enhanced tensile properties of a new beta Ti alloy, Journal of Alloys and Compounds

808 (2019) 151741. `doi:10.1016/j.jallcom.2019.151741`.

[181] A. Churchman, The yield phenomena, kink bands and geometric softening in titanium crystals, Acta Metallurgica 3 (1) (1955) 22–29. `doi:10.1016/0001-6160(55)90006-7`.

[182] D. Caillard, J.-L. Martin, Thermally activated mechanisms in crystal plasticity, Pergamon materials series, Elsevier, Oxford, 2003.

[183] I.-C. Choi, Y.-J. Kim, B. Ahn, M. Kawasaki, T. G. Langdon, J.-i. Jang, Evolution of plasticity, strain-rate sensitivity and the underlying deformation mechanism in Zn–22% Al during high-pressure torsion, Scripta Materialia 75 (2014) 102–105. `doi:10.1016/j.scriptamat.2013.12.003`.

[184] S. Narayanan, D. L. McDowell, T. Zhu, Crystal plasticity model for BCC iron atomistically informed by kinetics of correlated kinkpair nucleation on screw dislocation, Journal of the Mechanics and Physics of Solids 65 (2014) 54–68. `doi:10.1016/j.jmps.2014.01.004`.

[185] R. Schwaiger, B. Moser, M. Dao, N. Chollacoop, S. Suresh, Some critical experiments on the strain-rate sensitivity of nanocrystalline nickel, Acta Materialia 51 (17) (2003) 5159–5172. `doi:10.1016/s1359-6454(03)00365-3`.

[186] H. Conrad, Plastic deformation kinetics in nanocrystalline FCC metals based on the pile-up of dislocations, Nanotechnology 18 (32) (2007) 325701. `doi:10.1088/0957-4484/18/32/325701`.

[187] J. Moon, S. I. Hong, J. W. Bae, M. J. Jang, D. Yim, H. S. Kim, On the strain rate-dependent deformation mechanism of CoCrFeMnNi high-entropy alloy at liquid nitrogen temperature, Materials Research Letters

5 (7) (2017) 472–477. `doi:10.1080/21663831.2017.1323807`.

[188] G. Schoeck, The activation energy of dislocation movement, physica status solidi (b) 8 (2) (1965) 499–507. `doi:10.1002/pssb.19650080209`.

[189] B. Grabowski, N. Zotov, Thermally-activated dislocation mobility in bcc metals: An accelerated molecular dynamics study, Computational Materials Science 200 (2021) 110804. `doi:10.1016/j.commatsci.2021.110804`.

[190] B. Chen, S. Li, H. Zong, X. Ding, J. Sun, E. Ma, Unusual activated processes controlling dislocation motion in body-centered-cubic high-entropy alloys, Proceedings of the National Academy of Sciences 117 (28) (2020) 16199–16206. `doi:10.1073/pnas.1919136117`.

[191] G. Leyson, W. Curtin, Friedel vs. Labusch: the strong/weak pinning transition in solute strengthened metals, Philosophical Magazine 93 (19) (2013) 2428–2444. `doi:10.1080/14786435.2013.776718`.

[192] J. Wang, S. Basu, A. Kauffmann, M. Heilmaier, R. Schwaiger, The effect of grain boundaries and precipitates on the mechanical behavior of the refractory compositionally complex alloy NbMoCrTiAl, Applied Physics Letters 124 (20) (2024). `doi:10.1063/5.0203536`.

[193] A. M. James, M. P. Lord, Macmillan's chemical and physical data, Macmillan London, 1992.

[194] G. W. C. Kaye, T. H. Laby, Tables of physical and chemical constants and some mathematical functions, Longmans, Green and Company Limited, 1928.

Acknowledgements

A long journey of delving into the passion for understanding materials and acquiring knowledge is not complete without acknowledging the help and support from everyone around. Being an engineer from India and travelling all alone to pursue dreams of research in a country abroad, the path is not an easy one. My family, supervisors, friends and colleagues embalmed this thorny road that requires dedication and determination. First and foremost, before I express my gratitude to the project and my supervisors and each and every one supporting me, I would like to thank my parents **Mr. Sudipta Basu** and **Mrs. Sugata Basu**. I would not have had the opportunity to write this thesis and defend my passion without their help, support and sacrifice. They are more than just parents who guide their children to achievements. They are friends who helped me understand life and its complexities. They always encouraged the beauty of humanity and education and its connection to humbleness. I wish I could always keep up to their teachings. This thesis is a culmination of my work at **Institute of Applied Materials (IAM-WBM) at Karlsruhe Institute of Technology** from March 2018 to May 2021 and at **Institute of Energy and Climate Research 2 at Forschungszentrum, Jülich** from June 2021 to April 2022. The project was designed as a part of DFG Schwerpunktprogram Compositionally Complex Alloys-High Entropy Alloys (SPP CCA-HEA) ‘Identification of the intrinsic deformation mechanisms of

single phase body-centred cubic (BCC) high entropy alloy (HEAs). This dissertation would have been impossible to complete without the help and guidance from my advisor and supervisor **Prof. Dr. Ruth Schwaiger**. I have learned not only professionalism from her but dedication to work and science. I deeply express my gratitude to her for supporting me and encouraging me in times of need. The expression of gratitude goes invalid without appreciating the support from my advisor and supervisor **Dr. Christian Brandl**. Delving into the world of simulation and theoretical approach to science would have been extremely difficult without his support, guidance and discussions. I would also like to thank **Dr. Patric Gruber** for his constant support along with his discussions and inputs in the work. I would also like to extend my gratitude to my project partner **Korbinian Deck**, for his input and discussions on our common topic of work. The thesis would have been impossible to complete without their support and encouragement from them. The support of my group mates is equally appreciated. Performing experiments would not have been possible without the supply of materials that have been meticulously processed by Dr.-Ing Alexander Kauffmann's group in IAM–WK especially **Dr. Ing. Stephen Laube** and **Dr. Ing. Aditya Srinivasan**. Besides, I would like to thank **Prof. Dr.-Ing Marc Kamlah** and subsequently **Prof. Dr. mont: Christoph Kirchlechner** for providing a comfortable research environment at IAM-WBM. Life and work at the institute were fun and smooth. **Mrs. Jana Herzog** is a person to fall back on for any difficulties and **Mr. Ewald Ernst** does require a special mention for managing all technical troubles related to the laboratory. I am immensely grateful for the inputs, discussions and encouragements of **Dr. Heinz Riesch-Oppermann**. For a foreign researcher, it is very important that one find colleagues and friends who not only help with mundane problems but also provide a space for liberated and mind-stirring communication. The annus horibilus 2020 would not have been comfortable without friends in this faraway country. My colleagues at

KIT as well as in Forschungszentrum, Jülich have been an immense support to me. Be it the coffee breaks or Friday dine-outs, catching up on superhero movies, or hiking around, every day was better with my colleagues who in eventually became my friends. Such an intense journey is impossible without Alakh Dhruv Chopra and his support. I truly appreciate his effort to support me through all the ups and downs in this journey. Also the submission would not have been possible without the help of Mathias Jetter. The German version of the summary is legible owing to Marcel Siepmann. I am indebted to all my friends from school to bachelor's, from master's to PhD for helping me keep my sanity during this phase. This thank extends to my colleagues and friend at my present workplace OCAS NV (Belgium) for supporting me in the workplace to face new challenges as well as to motivate me to complete the most important phase of my life: my doctoral research. I would also like to take this opportunity to thank every teacher in my life from Kindergarten to high school, from my engineering days at Jadavpur University to my Masters's day at the Indian Institute of Technology, Kharagpur. They had always been the shining light instilling me with the courage and determination that I can achieve my goals.